Ancilla Assisted Quantum Information Processing: General protocols and NMR implementations

A thesis

Submitted in partial fulfillment of the requirements

Of the degree of

DOCTOR OF PHILOSOPHY

By

Abhishek Shukla

20093040

INDIAN INSTITUTE OF SCIENCE EDUCATION AND RESEARCH, PUNE

December, 2015

Dedicated to my parents

Declaration

I declare that this written submission represents my ideas in my own words and where others' ideas have been included, I have adequately cited and referenced the original sources. I also declare that I have adhered to all principles of academic honesty and integrity and have not misrepresented or fabricated or falsified any idea/data/fact/source in my submission. I understand that violation of the above will be cause for disciplinary action by the Institute and can also evoke penal action from the sources which have thus not been properly cited or from whom proper permission has not been taken when needed.

Date:

Abhishek Shukla

Roll No.- 20093040

Certificate

Certified that the work incorporated in the thesis entitled *"Ancilla Assisted quantum Information Processing: General protocols and NMR implementations"*, submitted by *Abhishek Shukla* was carried out by the candidate, under my supervision. The work presented here or any part of it has not been included in any other thesis submitted previously for the award of any degree or diploma from any other University or institution.

Dr. T. S. Mahesh

Date:

(Supervisor)

Acknowledgement

I must admit that this thesis would have not been possible without the help and support of many persons whom I met while pursuing PhD at IISER Pune. I have been very privileged to have so many wonderful friends and collaborators.

First of all, I thank to my research supervisor Dr. T. S. Mahesh for his guidance and encouragement. I am grateful to him for teaching me nuts and bolts of Quantum Information Processing and NMR. His deep understanding about the subject and generous behaviour played the key role behind my research. I consider myself fortunate to have a supervisor like him. I pay my gratitude to him for his support and affection.

I am thankful to Prof. Anil Kumar for various insightful discussions and his concern about my research. His immense knowledge of the field and positive attitude has always been a source of inspiration for me. I thank Prof. A. K. Rajagopal, Prof. Ushadevi, and H. S. Karthik for our collaborative work on moment inversion, which enhanced my curiosity for foundational issues in quantum physics. It was nice to work with Hemant and Manvendra as collaborator. I learned some good things from them. I also thanks to my other collaborators Sharad and Gaurav.

I thank my RAC members- Dr. Arijit Bhattacharyay, Dr. T. G. Ajitkumar, and Dr. K. Gopalakrishnan for their support through their comments and suggestions during annual evaluation of progress in my research. I also thank Dr. R. G. Bhat, Dr. V. G. Anand, and Dr. H. N. Gopi, for their help and affection. I am thankful to our Director Prof. K. N. Ganesh for providing all the necessary experimental facilities in the lab. I would like to thank IISER-Pune for the graduate scholarships that I received during my PhD. I also acknowledge administrative staff, security service people, and housekeeping persons of IISER-Pune. My academic life may have not taken shape in this way without my M.Sc. teacher Dr. Aanand Kumar. I am thankful to him for inciting my interest in Quantum Physics and also for his moral support. The list is incomplete without thanking my all other teachers.

I thank all the members of NMR Research Center -past and present- with whom I have worked. It was a pleasure working with my senior Soumya, his always positive attitude was really amazing. I can't forget relay of arguments between me and Swathi on various topics. I also thank her for giving me company at tea time for number of times in Innovation park canteen. It was really nice to work with Hemant and Koteswar (Sir Ji), Hemant's great attention for his work was always admirable. It was nice to listen Koteswar for basics of NMR. A person is always enjoys benefit if he has such a perfection loving friend. Optimizing the diffusion parameters with Manvendra was really enjoyable. I thank Pooja didi for teaching me how to operate NMR spectrometers. It was wonderful time in NMR lab at Innovation park with all group members. I enjoyed discussions with Ravi Shanker, Bhargava, Nitesh, Sudheer, along with the most young members Deepali, Deepak, Anjusha, and other project students. At last, I would like to pay a special thank to Sachin Kate for his easy availability and help on spectrometer issues.

Outside the lab, the life was enjoyable because of many friends and I thank all of them. First of all I thank all my friends in Physics department, especially friends from 2008 batch for their support and company. Anyone will feel lucky to have friends like them, I will always remember Mayur for his unconditional helps to everyone, Arun for his keen analysis, and Murthy for trying to tease me with his famous 'because of you' sentence. I always enjoyed Arthur's 'wo kya' approach. Resmi's keen observation and Kanika's optimistic behavior was always inspiring. I thank Vimal and Kajari for giving me company while studying in their offices. I thank all my friends in Chemistry department for providing me chemicals. It was awesome to roam, to fight, and to laugh with unforgettable friends Sumit and Abhigyan. I would like to thank to Ramya and Padma to tighten the knot as my sisters. At last I thanks my M.Sc. friends along with my long time friends Praveen, Manu, Rajesh, Neeraj, Anil, Vivek, Sarvesh, and Suchita for their support.

My research career would have not been possible without the great support of my family. I thank my mother, father, and sister for their love, support and encouragement. I also like to thank my cousin sisters and brothers for replacing my unavailability to support my parents in odd times. I found myself lucky to have a friend like Rajeev, I thank him

for always standing with me in any circumstances. I also thank to all my near and dear for their support and encouragement.

List of Publications

1. Soumya Singha Roy, **Abhishek Shukla**, and T. S. Mahesh, *NMR implementation of Quantum Delayed-Choice Experiment,* Phys. Rev. A 85, 022109 (2012).

2. Hemant Katiyar, **Abhishek Shukla**, Rama Koteswara Rao, and T. S. Mahesh, *Violation of Entropic Leggett-Garg Inequality in Nuclear Spin Ensembles,* Phys. Rev. A 87, 052102 (2013).

3. H. S. Karthik, Hemant Katiyar, **Abhishek Shukla**, T. S. Mahesh, A. R. Usha Devi, A. K. Rajagopal, *Inversion of moments to retrieve joint probabilities in quantum sequential measurements,* Phys. Rev. A 87, 052118 (2013).

4. **Abhishek Shukla**, K. Rama Koteswara Rao, and T. S. Mahesh, *Ancilla Assisted Quantum State Tomography in Many-Qubit Registers,* Phys. Rev. A 87, 062317 (2013).

5. **Abhishek Shukla**, Manvendra Sharma, and T. S. Mahesh, *NOON states in star-topology spin-systems: Applications in diffusion studies and RF inhomogeneity mapping* Chem. Phys. Lett. 592, 227 (2014).

6. Sharad Joshi, **Abhishek Shukla**, Hemant Katiyar, Anirban Hazra, and T. S. Mahesh, *Estimating Franck-Condon factors using an NMR quantum processor,* Phys. Rev. A 90, 022303 (2014).

7. **Abhishek Shukla** and T. S. Mahesh, *Single-Scan Quantum Process Tomography,* Phys. Rev. A 90, 052301(2014).

8. **Abhishek Shukla** and T. S. Mahesh, *Dynamical Decoupling of Spin-Clusters using Solid State NMR,* arXiv: quant-ph:1110.1473.

9. Gaurav Bhole, **Abhishek Shukla**, T. S. Mahesh, *Benford distributions in NMR,* arXiv:1406.7077 [physics.data-an].

10. Gaurav Bhole, **Abhishek Shukla**, T. S. Mahesh, *Benford Analysis: A useful paradigm for spectroscopic analysis,* Chem. Phys. Lett. 639, 36 (2015).

11. T. S. Mahesh, **Abhishek Shukla**, Swathi S. Hegde, C. S. Sudheer Kumar, Hemant Katiyar, Sharad Joshi, K. R. Koteswara Rao, *Ancilla assisted measurements on quantum ensembles: General protocols and applications in NMR quantum information processing,* Current Science 109, 1987 (2015).

Contents

Abstract

While a *bit* is the fundamental unit of binary classical information, a *qubit* is a fundamental unit of quantum information. In quantum information processing (QIP), it is customary to call the qubits under study as system qubits, and the additional qubits as ancillary qubits. In this thesis, I describe various schemes to exploit the ancillary qubits to efficiently perform many QIP tasks and their experimental demonstrations in nuclear magnetic resonancee (NMR) systems. Particularly, we have showed that, in the presence of sufficient ancillary qubits, it is possible to completely characterize a general quantum state as well as a general quantum dynamics in a single measurement. In addition, it is also possible to exploit ancillary qubits for realizing noninvasive quantum measurements required for several experiments related to quantum physics. Finally, I will also illustrate some interesting applications of ancillary qubits in spectroscopy. The abstracts of individual chapters are given below.

Chapter 1 is the introduction to this thesis. Here I describe about classical/quantum information, quantum information processing (QIP), nuclear magnetic resonance (NMR), NMR-QIP, and finally ancilla-assisted QIP.

The standard method of Quantum State Tomography (QST) relies on the measurement of a set of noncommuting observables, realized in a series of independent experiments. Ancilla Assisted QST (AAQST) greatly reduces the number of independent measurements by exploiting an ancilla register in a known initial state. In suitable conditions AAQST allows mapping out density matrix of an input register in a single experiment. In **chapter** 2, I describe methods for explicit construction of AAQST experiments in multi-qubit registers. I also report NMR implementations of AAQST on certain qubit-systems and the experimental results confirm the effectiveness of AAQST in such many-qubit registers.

In **chapter** 3, I present a procedure to characterize a general quantum process in a single ensemble measurement. The standard procedure for quantum process tomography (QPT) requires a series of experiments. Each experiment involves initialization of the system to a particular basis state, applying the quantum process ε on the system, and finally

characterizing the output state by quantum state tomography (QST). The output states collected for a complete set of basis states enable us to calculate the χ matrix characterizing the process ε. The standard procedure for QST itself requires independent experiments each involving measurement of a set of commuting observables. Thus QPT procedure demands a number of independent measurements, and moreover, this number increases rapidly with the size of the system. However in ensemble systems, the total number of independent measurements can be greatly reduced with the availability of ancilla qubits. Here we combine AAPT with AAQST to realize a 'single-scan QPT' (SSPT), a procedure to characterize a general quantum process in a single ensemble measurement. We demonstrate experimental SSPT by characterizing several single-qubit processes using a three-qubit NMR quantum register. Furthermore, using the SSPT procedure we experimentally characterize the twirling process and compare the results with theory.

The measurement as described in quantum mechanics is in general invasive. An invasive measurement may affect subsequent dynamics of the quantum system. In **chapter** 4, I report use of ancilla assisted noninvasive measurement to study following two problems. In section 4.1, I describe violation of entropic Leggett-Garg inequality in nuclear spin ensembles. Entropic Leggett-Garg inequality (ELGI) places a bound on the statistical measurement outcomes of dynamical observables describing a macrorealistic system [1]. Such a bound is not necessarily obeyed by quantum systems and therefore provides an important way to distinguish quantumness from classical behaviour. We studied ELGI using a two-qubit NMR system and the experimental results showed a clear violation of ELGI by over four standard deviations. In section 4.2, I describe our experiments on retrieving joint probabilities by inversion of moments. Further, we studied sequential measurements of a single quantum system and investigated their moments and joint probabilities [2] and demonstrated that the moments and the probabilities are inconsistent with each other.

The NOON state is a special multiple-quantum coherence that can be prepared easily using a star-topology spin-system. In **chapter** 5, I describe two important application of such systems: (i) measuring translational diffusion constants in liquids and (ii) quantitative characterization of radio-frequency (RF) inhomogeneity of NMR probes. When compared with the standard single quantum method, the NOON state method requires

shorter diffusion delays or weaker pulsed-field-gradients. Similarly, Torrey oscillations with NOON states decay at a faster rate than that of single quantum coherences and allow accurate characterization of RF inhomogeneity at higher RF powers.

In **chapter** 6, contains an experimental study of the efficiency of various dynamical decoupling sequences for suppressing decoherence of single as well as multiple quantum coherences (MQC) on large spin-clusters. The system involved crystallites of a powdered sample containing a large number of molecular protons interacting via long-range inter molecular dipole-dipole interaction. We invoked single as well as MQC using this interaction followed by an application of various DD sequences namely CPMG, UDD, and RUDD. The experiments reveal superior performance of RUDD sequences in suppressing decoherence.

Chapter 1

Introduction

The term information refers to the amount of knowledge contained either in a message or observation. Depending on the nature of states used for encoding and manipulating the information it can be classified as classical information and quantum information.

1.1 Classical Information

The digital information processing relies on encoding information by a set of discrete values. The smallest unit of information in the binary system is known as a *bit*, which is a mathematical object encoding two states of a computational device. Although information can be quantified in various other units such as byte, nat, trit, decimal etc, the bit being the simplest one, is the most popular unit. Claude Shannon, the founder of information theory, in his seminal paper has proposed a measure for the amount of information contained in a message [3]. Consider a message as a string of random variables, say (X_i). We may calculate the amount of information contained in such a message by calculating the uncertainty in values of random variables before we measure them or in other words the amount of information we gain after we know the value of (X_i) [4]. Entropy of this string of random variables is a function of the probabilities of different possible values the random variable takes. In his classic paper [3] Shannon showed that if $p_1, p_2, \cdots, p_n$ are the probabilities of values of random variables $X_1, X_2, \cdots, X_n$ consecutively, then entropy (and hence information) associated to such probability distribution must be of the form

$$H(X) = -\sum_i p_i \log_2 p_i. \tag{1.1}$$

For example: Information revealed in single flip of an unbiased coin is one bit, i.e., $H(X) = 1$, whereas in two coin flips it is $H(X) = 2$.

1.1.1 Conditional Entropy and Mutual Information

Consider two random variables X and Y. The total uncertainty corresponding to the simultaneous values of both variables, is known as the joint entropy $H(X, Y)$ of variables X and Y [3]. It depends on joint probability distribution $p(x, y)$ of outcomes of variable X and Y and can be calculated by the formula

$$H(X, Y) = -\sum_{x,y} p(x, y) \log p(x, y). \tag{1.2}$$

This definition of entropy can be extended to any set of random variables. The uncertainty associated to the values of one random variable say X, while knowing the value of the other variable say Y, can be calculated by the conditional entropy $H(X|Y)$ [3]. Suppose entropy of the known variable is $H(Y)$, then conditional entropy

$$H(X|Y) = H(X, Y) - H(Y). \tag{1.3}$$

Mutual information stored in variables X and Y can be calculated by subtracting joint entropy $H(X, Y)$ from the sum of individual entropies $H(X)$ and $H(Y)$ [5], i.e.,

$$H(X : Y) = H(X) + H(Y) - H(X, Y). \tag{1.4}$$

Using 1.3 and 1.4, the expression for mutual information can be rewritten as

$$H(X : Y) = H(X) - H(X|Y). \tag{1.5}$$

1.2 Quantum Information and its processing

Quantum Information Processing (QIP) is the branch of information processing in which the resources used are quantum mechanical systems [4]. In 1973, A. Holevo has proposed an inequality which puts an upper bound over the classical mutual information [6]. It infers that the encoding of n bits of classical information requires at least n bits of classical resources [4]. However because of the superposition principle, quantum mechanical sys-

tems are supposed to have a better encoding efficiency than their classical counterparts. This sets the motivation to use quantum resources for information processing.

Here I describe the chronological development of QIP. In 1973, C. H. Bennett showed that computation can be made logically reversible [7]. In 1975, R. P. Poplavaskii in his thermodynamic model of information processing" showed the computational infeasibility of simulating quantum systems" [8]. In 1981, Paul Beinoff proposed a model for a "non dissipative Turing machine" using quantum mechanical resources [9, 10]. In 1976 Polish mathematician Roman Stanislaw Ingarden, in his seminal work proposed a generalised concepts of using quantum systems for information processing [11]. In 1981, Yuri Manin had first proposed the idea of quantum computing [12] but it was R. Feynmann who actually set the platform. He observed that simulating quantum systems using classical computers is inefficient. He presented a model of quantum computers for simulating quantum systems [13]. In 1984 C. Bennett and G. Brassard presented *cryptographic key distribution* model using Weisner's conjugate coding [14]. This work opened a new perspective of QIP namely Quantum Communication. In 1991, A. Eckart invented an entanglement based protocol for secure quantum communication [15]. Year 1994 witnessed a milestone in development of QIP when Peter Shor from Bell labs developed an algorithm for efficient solution of (i) factorization problem (ii) descrete log problems [16]. Empowered with Shor's algorithm, quantum Computation become able to break many of the present days encryption codes. In 1994, P. Shor and A. Steane presented first scheme for error correction code [17, 18]. In 1996 Lov Grover from Bell labs came up with a search algorithm [19]. Unlike Shor's algorithm, quantum simulation, which provides an exponential speed up to computation, Grover's algorithm provides only quadratic speed up over existing classical algorithm. However, the algorithm can be used for a variety of problems, including database search [19, 20]. In 1997, D.Simon had invented an oracle problem for which a quantum computer was found exponentially faster than their classical counterparts [21]. As an important step in development of QIP, P. Divincenzo proposed a list of minimal requirements for any physical architecture to be able to realize QIP tasks [22].

Divincenzo's criteria includes the following:

1. Physical states to realize individually adressible qubits.

2. Ability to initialize system to any quantum state.

3. Universal set of quantum gates.

4. Qubit-specific measurement.

5. Sufficiently long coherence time(Depending on gate time).

   Other than these five points Divincenzo has also proposed two more points which are essential for quantum communication. These criteria are

6. Interconvertibility of stationary and flying qubits

7. Transmit flying qubits between distant locations

Execution of a QIP task can be divided into three parts, namely **initialization**, **evolution**, and **measurement**. These points are described below.

1.2.1 Quantum bit

Analogous to a classical bit, a quantum bit (*qubit*) is a two-dimensional mathematical object encoded by a two-level quantum system. Similar to the two states of a bit, usually represented by 0 and 1, the states of a qubit are represented by $|0\rangle$ or $|1\rangle$. In contrast, however, any quantum superposition of $|0\rangle$ and $|1\rangle$ is also a valid state of the qubit. Here $|0\rangle$ and $|1\rangle$ forms an orthonormal basis for state space of a qubit and can be used as *computational basis* in QIP. In this basis, the state of a qubit is in general represented as

$$|\psi\rangle = \alpha|0\rangle + \beta|1\rangle, \tag{1.6}$$

where $|\alpha|^2 + |\beta|^2 = 1$. Here quantities α and β are the complex numbers and forms a two dimensional complex vector space. In this space state, a qubit can be represented by a vector $\begin{bmatrix} \alpha \\ \beta \end{bmatrix}$. Consider the situation where we are interested in knowing the state of a classical bit. The information about the state of a classical bit is inherited in it, measurement just reveals it thus one can determine state with certainty. On the contrary, when a quantum mechanical system, say qubit, initially in state $|\psi\rangle$, is subjected to the

measurement process, we get an outcome $|0\rangle$ with probability $|\alpha|^2$ and an outcome $|1\rangle$ with probability $|\beta|^2$. This probabilistic outcome reveals the fact that the state of a system can not be measured by using a single copy in one experiment. To compute probabilities, we need either simultaneous measurement of a large number of copies of the qubit or a large number of measurements of a single qubit with repeated state preparation. Above is the description of state of a single quantum mechanical system. Below we describe the state of a multi-qubit quantum register.

Consider a register of n qubits. The most general state of such a register is given by

$$|\psi\rangle = \sum_j \alpha_j |\psi_{1j}\rangle \otimes |\psi_{2j}\rangle \otimes \cdots \otimes |\psi_{nj}\rangle, \tag{1.7}$$

where $|\psi_{ij}\rangle$ refers to ith qubit in jth term of the superposition, and α_j are the complex coefficients which together normalize to unity. We may choose $|\psi_{ij}\rangle \in \{|0\rangle, |1\rangle\}$, so that we can represent the combined state $|\psi\rangle$ by a set (product basis) of 2^n basis elements.

For example in the case of a two qubit system, the product basis contains four elements. These four basis elements are

$$|\phi_1\rangle = \begin{bmatrix} 1 \\ 0 \end{bmatrix} \otimes \begin{bmatrix} 1 \\ 0 \end{bmatrix} = \begin{bmatrix} 1 \\ 0 \\ 0 \\ 0 \end{bmatrix}; \qquad |\phi_2\rangle = \begin{bmatrix} 1 \\ 0 \end{bmatrix} \otimes \begin{bmatrix} 0 \\ 1 \end{bmatrix} = \begin{bmatrix} 0 \\ 1 \\ 0 \\ 0 \end{bmatrix};$$

$$|\phi_3\rangle = \begin{bmatrix} 0 \\ 1 \end{bmatrix} \otimes \begin{bmatrix} 1 \\ 0 \end{bmatrix} = \begin{bmatrix} 0 \\ 0 \\ 1 \\ 0 \end{bmatrix}; \qquad |\phi_4\rangle = \begin{bmatrix} 0 \\ 1 \end{bmatrix} \otimes \begin{bmatrix} 0 \\ 1 \end{bmatrix} = \begin{bmatrix} 0 \\ 0 \\ 0 \\ 1 \end{bmatrix}.$$

States of a qubit can be represented geometrically in terms of polar coordinates. In this representation all pure states lie on the surface of a sphere of unit radius known as

Bloch sphere. The most general state of a single qubit can then be written as

$$|\psi\rangle = \cos\frac{\theta}{2}|0\rangle + e^{i\phi}\sin\frac{\theta}{2}|1\rangle \tag{1.8}$$

where θ and ϕ are spherical polar co-ordinates. Bloch sphere representation is very helpful in visualizing the effects of quantum operations on the qubit.

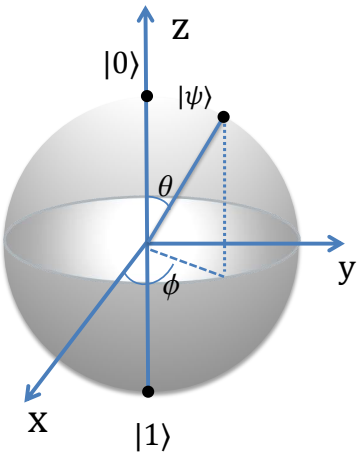

Figure 1.1: Bloch sphere representation of a single qubit states

1.2.2 Density Matrix Formulation

A quantum state can also be represented by an operator known as density operator. The density matrix formulation is very useful in describing the state of an ensemble quantum system such as in nuclear magnetic resonance (NMR). The diagonal terms of the density matrix correspond to the populations of the eigenstates. The off-diagonal terms represent coherences.

For an ensemble of states $|\psi_i\rangle$ each with probability p_i the density operator is $\rho = \sum_i p_i|\psi_i\rangle\langle\psi_i|$ (here $\sum_i p_i = 1$). If all the members of the ensemble are in the same state, we call it a *pure state*. The density operator corresponding to a pure state $|\psi\rangle = \sum_j c_j|j\rangle$ is

$$\rho_{pure} = |\psi\rangle\langle\psi| = \sum_j \sum_k c_j c_k^* |j\rangle\langle k|. \tag{1.9}$$

where c_j's are the probability amplitudes in basis $|j\rangle$. In the case of a *mixed state*, there exists a distribution of sates $|\psi_i\rangle$ with respective probabilities p_i. In this case the density operator can be written as

$$\begin{aligned} \rho_{mixed} &= \sum_i p_i |\psi_i\rangle\langle\psi_i| = \sum_j \sum_k \overline{c_j c_k^*} |j\rangle\langle k| \\ &= \sum_i p_i \rho_i, \end{aligned} \tag{1.10}$$

where ρ_i is the state of an individual quantum system of ensemble with probabilities p_i. A density operator ρ satisfies three important properties

1. ρ is Hermitian, i.e., $\rho^\dagger = \rho$.

2. ρ is a positive operator, i.e., eigenvalues are all non-negative.

3. $\mathrm{Tr}[\rho] = 1$.

   Other than the above properties, density matrix also satisfies the following properties.

4. For a pure state, density operator ρ is idempotent, i.e., $\rho^2 = \rho$ so that $\mathrm{Tr}[\rho^2] = \mathrm{Tr}[\rho] = 1$, while for a mixed state, $\mathrm{Tr}[\rho^2] < 1$.

In terms of Bloch sphere, the most general state of a single qubit can be written as

$$\rho = \frac{\mathbb{I} + \vec{r} \cdot \vec{\sigma}}{2} \tag{1.11}$$

where $\vec{\sigma} = \sum_i \vec{\sigma}_i$ is the Pauli vector operator and $\vec{r}$ is a three dimensional Bloch vector s.t. $||\vec{r}|| \leq 1$.

1.2.3 Entangled state

Like various other non classical features, entanglement is also a completely quantum mechanical phenomenon. An entangled state of a composite quantum system is that which cannot be expressed in terms of states of its components. This criteria is known as separability criteria. Consider an n-component composite system. If $|\psi_1\rangle, |\psi_2\rangle, \cdots, |\psi_n\rangle$ are

the states of the components $A_1, A_2, \cdots, A_n$, then an entangled state $|\psi_{EN}\rangle$ can not be expressed as $|\psi_1\rangle \otimes |\psi_2\rangle \otimes \cdots \otimes |\psi_n\rangle$.

Entanglement plays a very crucial role in various protocols of QIP. Non separability criteria of entanglement lies in the very heart of various quantum communication protocols such as quantum cryptography, superdense coding, and quantum teleportation. An entangled state is called a maximally entangled state if on tracing out one subsystem from the composite system, the rest of the system falls into a maximally mixed state.

Simple examples for maximally entangled states include Bell states of the form

$$|\phi_{\pm}\rangle = \frac{|00\rangle \pm |11\rangle}{\sqrt{2}}. \tag{1.12}$$

Suppose we measure the state of first qubit, and the outcome is 0. This can happen with a probability $\frac{1}{2}$. Then this measurement outcome infers that the state of the second qubit must also be 0. Similarly, if the measurement outcome for the first qubit is 1, then the outcome of the second qubit must also be 1. The other two Bell states are of the form

$$|\psi_{\pm}\rangle = \frac{|01\rangle \pm |10\rangle}{\sqrt{2}}. \tag{1.13}$$

1.2.4 Quantum gates

In a classical computer, classical information can be manipulated using physical tools known as classical logic gates e.g. NOT, OR, NOR, etc. Similarly in quantum computation, quantum information can be manipulated using quantum gates which can be realized by unitary operators U ($UU^{\dagger} = \mathbb{I}$). Thus quantum logic gates are reversible in nature. An efficient implementation of such a quantum operation can be achieved by decomposing it into one qubit gates (local gates) and two qubit gates (non-local gates). Local gates together with C-NOT gates (explained below) form universal gates.

Below we describe some important one qubit and two qubit gates.

1.2.4.1 Single qubit gates

X **gates**: Similar to the classical NOT gate, a quantum NOT gate transforms the state $|0\rangle$ into $|1\rangle$ and vice-versa. Matrix form of this gate is same as that of the Pauli operator σ_x:

$$X = \begin{bmatrix} 0 & 1 \\ 1 & 0 \end{bmatrix}.$$

Operation of NOT gate can be written as

$$\begin{bmatrix} 0 & 1 \\ 1 & 0 \end{bmatrix} \begin{bmatrix} 0 \\ 1 \end{bmatrix} = \begin{bmatrix} 1 \\ 0 \end{bmatrix}.$$

Hadamard gates: The Hadamard gate transforms state $|0\rangle$ into state $|+\rangle = \frac{|0\rangle+|1\rangle}{\sqrt{2}}$ and $|1\rangle$ into state $|-\rangle = \frac{|0\rangle-|1\rangle}{\sqrt{2}}$. The Hadamard gate is represented by H and the matrix form is

$$H = \frac{1}{\sqrt{2}} \begin{bmatrix} 1 & 1 \\ 1 & -1 \end{bmatrix}.$$

Since $H^2 = \mathbf{I}$, two consecutive applications of H operator does not change the initial state.

Z **gates**: The Z gate introduces a relative phase of π to the state $|1\rangle$. Matrix form of Z-gate is

$$Z = \begin{bmatrix} 1 & 0 \\ 0 & -1 \end{bmatrix}.$$

Phase gate: The phase gate introduces a relative phase factor 'i' corresponding to a phase of $\frac{\pi}{2}$ to the state $|1\rangle$. Matrix form of phase gate (denoted by S) is

$$S = \begin{bmatrix} 1 & 0 \\ 0 & i \end{bmatrix}.$$

1.2.4.2 Multi qubit gates

Control-NOT (C-NOT) gates: C-NOT is a two qubit gate, in which one qubit works as control while other qubit works as target. Application of the C-NOT gate leads to selective inversion of target qubit w.r.t. $|1\rangle$ state of control qubit. Quantum circuit and truth table for C-NOT gate are shown in Fig. 1.2.

Matrix form of C-NOT gate is the following:

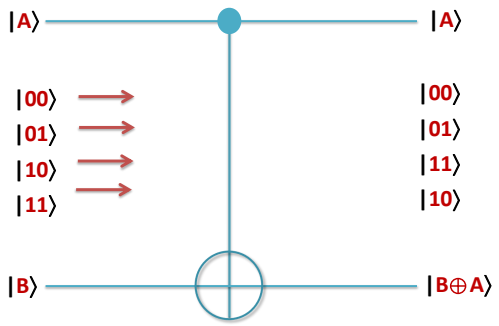

Figure 1.2: Circuit for the C-NOT gate.

$$\text{C-NOT}=\begin{bmatrix}1 & 0 & 0 & 0\\ 0 & 1 & 0 & 0\\ 0 & 0 & 0 & 1\\ 0 & 0 & 1 & 0\end{bmatrix}.$$

1.2.5 Quantum measurement

Some important measurement schemes used in quantum information and quantum computation include (i) projective measurement, (ii) positive operator valued measure (POVM), (iii) weak measurement, and (iv) protective measurement. I shall describe the first two schemes in the following.

Consider a quantum system in the state $|\psi\rangle = \sum_m c_m|m\rangle$ being projectively measured by an observable M having a spectral decomposition s.t. $M = \sum_m mM_m$. Here m are the eigenvalues and M_m are the corresponding projectors which form a complete basis s.t. $\sum_m M_m = \mathbb{I}$. According the measurement postulate of quantum theory [4, 23, 24], the post-measurement state of the system is given by,

$$|\psi_m\rangle = \frac{M_m|\psi\rangle}{p_m}. \tag{1.14}$$

Here $p_m = \langle\psi|M_m^\dagger M_m|\psi\rangle$ is the probability of getting the outcome m.

Often, when knowledge of the post measurement state is of less importance, it is convenient to use the POVM formalism. Here one considers a set of measurement operators

$\{M_m\}$ which are not necessarily orthogonal. If the measurement is performed on a system with state $|\psi\rangle$, the probability of outcome m is $p_m = \langle\psi|M_m^\dagger M_m|\psi\rangle$. We define the POVM elements $E_m = M_m^\dagger M_m$. Then $\sum_m E_m = I$ and the probability $p_m = \langle\psi|E_m|\psi\rangle$. Set $\{E_m\}$ is known as POVM [4]. POVM has been utilized in studying many of the foundational problems of quantum mechanics. Furthermore it has also been applied to quantum state tomography [25] and quantum cryptography [25].

1.2.6 Experimental Architectures

Even after a lot of development in theoretical QIP, so far a physical architecture for a universal quantum computer is still a mirage. As described earlier, any physical device must satisfy Divincenzo criteria in order to qualify as a general quantum processor [22]. Till date there exist no architecture which can full fill all these criteria in one set up. Nevertheless several architecture are being explored for the efficient implementation of various QIP tasks. Some of these techniques are

1. NMR
2. Nitrogen vacancy centers
3. Quantum dots
4. Superconducting quantum interface devices
5. Ion/atom trap
6. Linear optics

A comparison of the merits and the demerits of various QIP architectures is given below [26, 27].

Architecture	NMR	SQUIDS	Linear optics	NV centre	quantum dots	Trapped Ions
System type	Nuclear spins	Flux/charge qubits	Photons	Defect centres	Semiconductor	Atoms
Maximum qubits for QIP	Entangled (12) Correlated in solids (64)	Fabricated (512) Entangled (3)	Entangled (10)	Realized (3)	Realized (1)	Stored(10-10^3) Entangled (14)
Control technique's	RF pulses	MW pulses, Current, Voltage	Optical	RF, optical Electrical	RF, optical Electrical	MW, Optical, RF, Electrical
Coherence time	~ (1-3) sec ~ ms	~ 10 μ s	~ 100 μ s	(1-10) ms	(1-10) μ s	$\geq$ 1s
Gate fidelity	(0.99-0.999)	~ (0.90-0.95)	$\geq$ 0.95	~ 0.9	~ 0.9	(0.99-0.999)
Measurement	Bulk Magnetization	flux Charge	Optical responses	Electrical and Optical	Electrical and Optical	Fluorescence Optical

Table 1.1: Comparison of the merits and the demerits of various architectures

.

1.3 Nuclear Magnetic Resonance

Story of nuclear magnetism begins from 1922, with one of the most famous experiment of quantum mechanics, The Stern-Gerlach experiment. In this experiment Stern and Gerlach demonstrated the existence of energy levels in presence of inhomogeneous magnetic field [28]. Further Fresch, Estermann, and Stern in between 1933-1937 succeeded in measuring proton magnetism. On the basis of these experiments, understanding of nuclear magnetism is as follows. Nuclei of most isotopes posses an intrinsic physical property called *spin*. All spins have spin angular momentum and hence an associated magnetic moment. When a spin having a net magnetic moment is placed in an external magnetic field it aligns in the direction of this magnetic field. This magnetic field lifts degeneracy and splits energy level into multiple levels depending on spin angular momentum number. For example, In case of a spin $\frac{1}{2}$ nucleus, external magnetic field of strength B_0 splits energy level into two sub levels say $|1/2\rangle$ and $|-1/2\rangle$ with energies $-\frac{\gamma B_0 \hbar}{2}$ and $\frac{\gamma B_0 \hbar}{2}$. Such a system is irradiated with an RF radiation. When the frequency of the RF becomes equal to the frequency corresponding to the energy difference between the two levels, resonance occurs. This phenomenon is known as nuclear magnetic resonance (NMR) [29]. The coherent oscillations between two levels were first observed by Rabi in 1937 [30]. These oscillations lead to an absorption spectrum typically known as a NMR spectrum. In 1945 Purcell and his co-workers [31], and Bloch and co-workers [32], independently observed the first NMR signal from bulk matter.

NMR techniques depend on the state of the sample, and broadly classified into liquid

state NMR, liquid crystal NMR, and solid state NMR. In liquid state NMR, the solute containing the system of interest, is dissolved in a sui solvent to prepare an isotropic solution. In such samples, molecular tumbling motions average out anisotropic and dipole-dipole interactions and lead to a simple spectrum but at the cost of certain information on spin interactions. In solid state NMR, because of the closely spaced and spatially oriented spin-systems, strong anisotropic spin interactions arise including the dipolar interactions. Although in this case one obtains a broad spectrum, by suitably modulating the anisotropic interactions, it is possible to extract average spatial information about the spin system. Various techniques for modulating the interactions have been developed over the years [33].

A spin system partially oriented in a liquid crystal has restricted motion and hence possesses reduced anisotropic interactions, while still leading to highly resolved spectral lines. Availability of dipolar coupling and high resolution makes such partially oriented spin-systems an attractive candidate for studying quantum information. Firstly, such systems display only orientational order, but no spatial order, and hence form well-defined qubit-systems with only intramolecular interactions. Secondly, the longer range of the intramolecular dipolar couplings may allow realizing larger number of qubits. Thirdly, the residual dipolar interactions are much stronger than the scalar interactions (which are the only spin-spin interactions surviving in liquids) and allow synthesis of faster quantum gates.

1.3.1 NMR Interactions

The NMR interactions in general can be described by second order tensors. In the following I shall describe different types of interactions.

1.3.1.1 Zeeman interaction

Consider a spin$-I$ (I is the spin-quantum number which can take integral or half-integral values) nucleus with an associated magnetic moment $\boldsymbol{\mu} = \gamma\hbar\mathbf{I}$, where γ is the gyromagnetic ratio, $\hbar$ is the reduced Planck constant ($h/2\pi$), and $\mathbf{I}$ is the spin operator. If the spin is placed in an external magnetic field B_0 applied along the $\hat{z}$ direction, the Zeeman

interaction is described by the Hamiltonian

$$H_Z = -\gamma\hbar B_0 I_z, \tag{1.15}$$

where I_z is the z component of the spin operator $\mathbf{I}$ [34]. The $(2I + 1)$ eigenvalues of the Zeeman Hamiltonian are $E_m = -\gamma\hbar B_0 m$, where $m = -I, -I + 1, \cdots, I - 1, I$. The energy gap between the successive levels is $\Delta E = \hbar\omega_0$, where $\omega_0 = -\gamma B_0$ is known as the Larmor frequency.

Thermal Equilibrium State:

At thermal equilibrium the populations of energy levels are governed by Boltzmann statistics. The state of the system at temperature T and magnetic field B_0 is described by the density operator

$$\rho = \frac{e^{-H_Z/k_B T}}{Z} \tag{1.16}$$

where Z is the partition function, k_B is the Boltzmann constant, and T is the absolute temperature. For an ensemble of spin-1/2 nuclei, the ratio of populations p_0 and p_1 respectively corresponding to states $|0\rangle \equiv |1/2\rangle$ and $|1\rangle \equiv |-1/2\rangle$ is

$$\frac{p_0}{p_1} = 1 + \frac{\hbar\omega_0}{k_B T} \tag{1.17}$$

under high temperature and low field approximation. For a Zeeman-field of 10 T at room temperature quantity $\frac{\hbar\omega_0}{k_B T} \sim 10^{-5}$. Thus population of the ground state is slightly more than the excited state. This slight imbalance in populations leads to a net magnetization in $\hat{z}$ direction. The nuclear magnetization for an ensemble of n spin-1/2 nuclei at thermal equilibrium is given by

$$M_0 = \frac{\mu_0 \gamma^2 \hbar^2 B_0}{4 k_B T} \tag{1.18}$$

where μ_0 is the permeability of free-space [35].

Nucleus	Abundance	Spin	γ (10^6 rad/T/s)	Absolute sensitivity
^1H	$\sim$ 100%	1/2	267.522	1
^{13}C	$\sim$ 1.1%	1/2	67.283	1.76^*10^{-4}
^{15}N	$\sim$ 0.4%	1/2	−27.12	3.85^*10^{-6}
^{19}F	$\sim$ 100%	1/2	251.815	0.83
^{31}P	$\sim$ 100%	1/2	10.394	6.63^*10^{-2}

Table 1.2: Comparison of properties of some spin-1/2 nuclei

1.3.1.2 Chemical shift interaction

For a nucleus in a molecule, the local magnetic field is different from the external magnetic field due to the induced field by the nearby diamagnetic electrons. Since the density of the electron cloud depends on the chemical environment, so is the local field. This local field is given by

$$B_{\text{loc}} = B_0(1 - \sigma_0), \tag{1.19}$$

[34], where σ_0 is known as the *chemical shift tensor*. The induced field is generally small compared to B_0, but is sufficient to create a measurable shift in Larmor frequency. This shift, called *Chemical Shift*, is an important tool in structural analysis.

1.3.1.3 Dipole-dipole interaction

A pair of nearby nuclei can exhibit dipole-dipole (DD) interaction by inducing local fields at the site of each other. Such a through-space interaction leads to what is known as the *direct dipolar coupling*. The Hamiltonian for the DD interaction between two nuclei j and k is given by [33]

$$H_{\text{DD}}^{jk} = \mathbf{I}^j \cdot \mathbf{D}^{jk} \cdot \mathbf{I}^k. \tag{1.20}$$

Here $\mathbf{D}^{jk}$ is a 2nd rank tensor and $\mathbf{I}^j$, $\mathbf{I}^k$ are 1st rank spin tensors. On expressing $\mathbf{I}^j$ and $\mathbf{I}^k$ in terms of their z components (I_z^j, I_z^k), raising spin operators (I_+^j, I_+^k), and lowering spin

operators (I_-^j, I_-^k), the dipolar Hamiltonian can be written as [36].

$$H_{\mathrm{DD}}^{jk} = b^{jk}(A + B + C + D + E + F), \tag{1.21}$$

where,

$$\begin{aligned} A &= I_z^j I_z^k (1 - 3\cos^2\theta) \\ B &= -\frac{1}{4}(I_+^j I_-^k + I_-^j I_+^k)(1 - 3\cos^2\theta) \\ C &= -\frac{3}{2}(I_+^j I_z^k + I_z^j I_+^k)\sin\theta\cos\theta e^{-i\phi} \\ D &= -\frac{3}{2}(I_-^j I_z^k + I_z^j I_-^k)\sin\theta\cos\theta e^{i\phi} \\ E &= -\frac{3}{4}(I_+^j I_+^k)\sin^2\theta e^{-2i\phi} \\ F &= -\frac{3}{4}(I_-^j I_-^k)\sin^2\theta e^{2i\phi}, \end{aligned} \tag{1.22}$$

with θ being the angle between $\vec{r}^{jk}$ (radius vector from spin j to k) and $\hat{z}$, and $b^{jk} = -\frac{\mu_0 \gamma^j \gamma^k \hbar}{4\pi (r^{jk})^3}$. Under the secular approximation, the terms C, D, E, and F can be discarded and the truncated Hamiltonian becomes

$$H_{\mathrm{DD}}^{jk} = d^{jk}(3I_z^j I_z^k - \mathbf{I}^j \cdot \mathbf{I}^k), \tag{1.23}$$

where $d^{jk} = \frac{b^{jk}}{2}(3\cos^2\theta - 1)$. In weakly-dipolar-coupled systems (wherein the dipolar coupling is much smaller than the corresponding chemical shift difference) or in heteronuclear spin systems, the dipolar coupling Hamiltonian can be further approximated to

$$H_{\mathrm{DD}}^{jk} = 2d^{jk} I_z^j I_z^k \tag{1.24}$$

[36].

In an *isotropic liquid*, molecules execute fast tumbling motion thus averaging the in-

tramolecular dipolar coupling to zero [35], i.e.,

$$\int_0^{\pi} (3\cos^2\theta - 1)\sin\theta d\theta = 0. \tag{1.25}$$

In an *anisotropic liquid*, partial alignment of molecules leads to an incomplete averaging of dipolar coupling. Thus in this case the residual dipolar coupling constant amounts to $d_{jk} = b_{jk}S$, where the average quantity $S = \overline{(3\cos^2\theta - 1)/2}$ is the order parameter of the oriented spin-systems.

1.3.1.4 Quadrupolar interaction

Nuclei with spin $s > 1/2$ posses an asymmetric charge distribution due to nucleons. Such nuclei posses quadrupolar charge distribution and hence an associated electric quadrupolar moment. The electric quadrupolar moment interacts strongly with surrounding electric field gradients. If θ is the orientation of atomic framework w.r.t. external magnetic field direction $\hat{z}$, the quadrupolar Hamiltonian for corresponding nucleus is [35]

$$H_Q(\theta) = \frac{eQ}{2I(2I-1)}\mathbf{I}\cdot\mathbf{V}(\theta)\cdot\mathbf{I}. \tag{1.26}$$

Here Q is the quadrupolar moment, I is the spin quantum number, $\mathbf{I}$ is the nuclear spin tensor, and $\mathbf{V}(\theta)$ is the electric field gradient tensor at the cite of nucleus. Usually strength of the quadrupolar interaction varies from a few kHz to hundreds of MHz. If the interaction is weak compared to the Zeeman interaction, we may discard higher order terms, but more often quadrupolar interaction is strong enough. So we need to keep higher order terms, mostly till second order. The full Hamiltonian is

$$H_{\mathrm{Q}} = H_{\mathrm{Q}}^{(1)} + H_{\mathrm{Q}}^{(2)}. \tag{1.27}$$

Here first order coupling constant $H_{\mathrm{Q}}^{(1)}$ is

$$H_{\mathrm{Q}}^{(1)} = \omega_{\mathrm{Q}}^{(1)}\frac{1}{6}\left\{3I_z^2 - I(I+1)\mathbb{I}\right\}, \tag{1.28}$$

where $\omega_{\mathrm{Q}}^{(1)} = \frac{3eQ\overline{V}_{zz}}{2I(2I-1)\hbar}$.

The second order term $H_{\mathrm{Q}}^{(2)}$ is more complex, however, the second order coupling is such that $\omega_{\mathrm{Q}}^{(2)} \sim \left|\frac{\omega_Q^{(1)}}{\omega_0}\right|$, where the denominator is the Larmor frequency.

1.3.1.5 Radio Frequency (RF) interaction

In NMR, the spin manipulations are realized with the help of RF pulses. Consider the magnetic component of an RF field, $2B_1\cos(\omega_{\mathrm{RF}}t + \phi)\hat{x}$. The corresponding Hamiltonian is

$$H_{\mathrm{RF}} = -\boldsymbol{\mu} \cdot 2B_1(t)\hat{x} = 2\omega_1\hbar I_x \cos(\omega_{\mathrm{RF}}t + \phi). \tag{1.29}$$

Here $\omega_1 = -\gamma B_1$ is the effective RF amplitude, ω_{RF} is the RF frequency, and ϕ is the RF phase. When $\omega_{\mathrm{RF}} = \omega_0$ we achieve resonance condition. Difference between the two frequencies is known as offset.

Rotating frame: The linearly polarized RF field $2B_1\cos(\omega_{\mathrm{RF}}t+\phi)\hat{x}$ can be decomposed into right ($\mathbf{B_r}$) and left ($\mathbf{B_l}$) circularly polarized RF fields

$$\begin{aligned} \mathbf{B_r} &= B_1\left\{\cos(\omega_{\mathrm{RF}}t + \phi)\hat{x} + \sin(\omega_{\mathrm{RF}}t + \phi)\hat{y}\right\}, \text{ and} \\ \mathbf{B_l} &= B_1\left\{\cos(\omega_{\mathrm{RF}}t + \phi)\hat{x} - \sin(\omega_{\mathrm{RF}}t + \phi)\hat{y}\right\}. \end{aligned} \tag{1.30}$$

If we choose $\omega_{\mathrm{RF}} = \omega_0$, the first component ($\mathbf{B_r}$) precesses about the $\hat{z}$ axis in the same sense as the nuclear spin, realizing resonance condition. The other RF component precesses in opposite direction (equivalent to frequency $-\omega_{\mathrm{RF}}$) and hence will be out of resonance. The latter component is ignored under high-field conditions, but causes Bloch-Siegert shift as RF strength becomes comparable to the Larmor frequency [37]. Now we choose a frame, also rotating about $\hat{z}$ axis with frequency ω_{RF}. In this frame the RF component $\mathbf{B_r}$ appears static,

$$\mathbf{B_r}' = B_1\left\{\cos\phi\hat{x} + \sin\phi\hat{y}\right\}. \tag{1.31}$$

In the off-resonant case, with offset $\Omega = \omega_0 - \omega_{\mathrm{RF}}$, the effective field in the rotating frame

is the vector sum of the RF in the transverse direction and the offset in the longitudinal direction,

$$\mathbf{B}_{\text{eff}} = -\frac{\Omega}{\gamma}\hat{z} - \frac{\omega_1}{\gamma}\left\{\cos\phi\hat{x} + \sin\phi\hat{y}\right\}. \tag{1.32}$$

The RF Hamiltonian in the rotating frame thus becomes,

$$\begin{aligned} H_{\text{eff}} &= -\boldsymbol{\mu}\cdot\mathbf{B}_{\text{eff}} \\ &= \Omega\hbar I_z + \omega_1\hbar\left\{I_x\cos\phi + I_y\sin\phi\right\}. \end{aligned} \tag{1.33}$$

The evolution of the quantum ensemble under the effective field in the rotating frame is described by the time-dependent density operator,

$$\rho_{\text{r}}(t) = e^{-iH_{\text{eff}}t}\rho_{\text{r}}(0)e^{iH_{\text{eff}}t}, \tag{1.34}$$

where $\rho_{\text{r}}(0)$ describes the initial condition.

If $\Omega = 0$ (on-resonance) and $\phi = 0$, the effective field is along $\hat{x}$ direction. Then, in the rotating frame, the magnetization nutates about $\hat{x}$. Choosing the duration of RF τ such that $\omega_1\tau = \theta$, it is possible to obtain a θ_x pulse. In general, the effective nutation frequency about the effective field is $\omega_{\text{eff}} = \sqrt{\Omega^2 + \omega_1^2}$.

1.3.2 Relaxation of nuclear spins

Relaxation is the process which brings nuclear spins back to thermal equilibrium. Nuclear spin relaxation is a consequence of interaction of the spin system to the surrounding environment or lattice. The lattice can introduce a random time dependent magnetic field fluctuations at the site of a spin. Frequency components of this fluctuating local field can be decomposed in two parts, parallel and perpendicular to the static field. Depending On the direction of frequency components of fluctuating local field at the site of spin system, NMR relaxation can be classified in following two ways [34].

1.3.2.1 Longitudinal relaxation

The transverse frequency components of the local fluctuating fields are responsible for non-adiabatic contributions to relaxation. Random magnetic fields with a magnitude equal to the Larmor frequency induce a transition of spin system population from higher energy state to lower energy state and corresponding lattice population from lower energy state to higher energy state via an energy conserving process. This loss of energy of spin system to the lattice brings spin system in thermal equilibrium. Furthermore being a non-adiabatic transition, it also introduces some uncertainty in the energies of eigenstates. This uncertainty leads to fluctuations in Larmor frequency of spin system, resulting in the decay of phase coherence in time. Consequently non-adiabatic transitions lead to both longitudinal as well as transverse relaxation.

1.3.2.2 Transverse relaxation

On the other hand the longitudinal frequency components which are responsible for adiabatic transition cause a fluctuation in Larmor frequency leading to the loss of phase coherence. As a result the off diagonal terms in the density matrix undergo decay. Since adiabatic transitions do not contribute to any exchange of energy between the spin system and lattice, the populations of the spin states remain unaltered. So adiabatic transitions are responsible only for transverse relaxation.

1.4 NMR quantum information processing

NMR has already provided a number of applications in spectroscopy, imaging, and many other fields of science and technology. The experimental realization of QIP is another recent application of NMR. In 1997, Cory et al and Chuang et al have independently proposed that NMR can be used as an experimental architecture for QIP [38, 39]. They proposed that the difficulty of achieving pure states in NMR can be overcome by preparing a special mixed state, called pseudopure state. This approach provided a realistic way for NMR-QIP in ensemble systems. After that, till date a number of QIP tasks have been implemented using NMR. Availability of numerous well developed techniques in

conventional NMR and favourable properties of spin systems helped in establishing NMR as a good candidate for QIP. Some of the details about NMR architecture are mentioned below.

The developments in control of spin dynamics via specially designed RF pulses have facilitated realization of quantum gates with high fidelities. One utilizes internal Hamiltonian (Zeeman, Spin-Spin interactions) along with an external control Hamiltonian (RF), to realize universal quantum gates. Also, the NMR spin systems, being weakly coupled to the environment, exhibit long coherence times compared to many other architectures. Even with all these merits, liquid state NMR-QIP is limited by the scalability criterion. Thus in the present scenario, implementation of a large scale quantum computation using NMR is difficult. Till now, the largest register used for computation involves a dozen-qubit [40]. Hope is still alive with solid-state NMR spin systems where one may achieve larger registers and with shorter gate times. A comparative study of various architectures has already been given by 1.1. NMR-QIP protocols can be broadly divided into three parts: (a) initialization (b) realization of a quantum circuit via robust quantum gates, and (c) measurements or characterization of the output states. Below we will explain these in detail along with a brief description of NMR systems.

1.4.1 NMR qubits

The natural choice to mimic a qubit is a spin-1/2 nucleus. A multispin system with spin-spin interactions can be used to realize a multiqubit register.

1.4.2 Initialization

A quantum algorithm usually begins with a definitely known initial state or a pure state. Achieving a pure state in conventional NMR is not practical. One way to overcome this problem is by preparing a pseudopure state which is isomorphic to a pure state.

Pseudopure state: An ensemble is said to be in a pure state $|\psi\rangle$, when all its members are in the state $|\psi\rangle$. The density operator for the pure state is given by $\rho_{\text{pure}} = |\psi\rangle\langle\psi|$. An ensemble is said to be in a pseudopure state if it is described by the density operator of

the type $\rho_{\text{pps}} = (1-\epsilon)\mathbb{I}/N + \epsilon\rho_{\text{pure}}$. An example is illustrated in Figure 1.3.

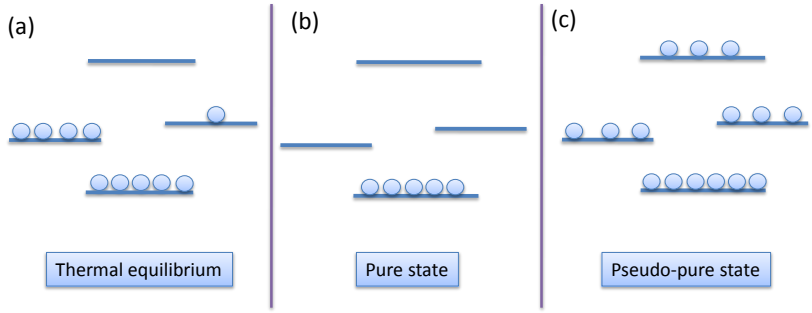

Figure 1.3: Distribution of population for a heteronuclear two-spin system (a) for thermal equilibrium state, (b) pure state, and (c) pseudopure state

1.4.2.1 Spatial averaging

This method of preparing pseudopure states involves RF pulses and pulsed-field-gradients (PFGs) [38]. In the following, we describe this method by considering a homonuclear spin-pair using product operator formalism:

Below we show preparation of ρ_{00} pseudopure state in a two spin system using product operator formalism.

$$
\begin{aligned}
I_z^1 + I_z^2 &\xrightarrow{(\frac{\pi}{3})_x^2} I_z^1 + \frac{1}{2}I_z^2 + \frac{\sqrt{3}}{2}I_y^2 \\
&\xrightarrow{G_z} I_z^1 + \frac{1}{2}I_z^2 \\
&\xrightarrow{(\frac{\pi}{4})_x^1} \frac{1}{\sqrt{2}}I_z^1 - \frac{1}{\sqrt{2}}I_y^1 + \frac{1}{2}I_z^2 \\
&\xrightarrow{\frac{1}{2J_{12}}} \frac{1}{\sqrt{2}}I_z^1 + \frac{1}{\sqrt{2}}2I_x^1I_z^2 + \frac{1}{2}I_z^2 \\
&\xrightarrow{(\frac{\pi}{4})_{-y}^1} \frac{1}{2}I_z^1 - \frac{1}{2}I_x^1 + \frac{1}{2}2I_x^1I_z^2 + \frac{1}{2}2I_z^1I_z^2 + \frac{1}{2}I_z^2 \\
&\xrightarrow{G_z} \frac{1}{2}(I_z^1 + I_z^2 + 2I_z^1I_z^2) \\
&\equiv \frac{1-\epsilon}{4}\mathbb{I}_{\text{n}} + \epsilon|00\rangle\langle 00|. \qquad (1.35)
\end{aligned}
$$

In the above set of expressions, $\frac{1}{2J_{12}}$ represents an evolution under spin-spin interaction (J-coupling) for the duration $\frac{1}{2J_{12}}$, and G_z represents PFG applied to destroy transverse magnetization.

1.4.2.2 Logical labelling

In 1997 Gershenfield and chuang proposed a method to prepare subsystem in pseudopure state [39]. For example: in the case of a homonuclear system of three spin-1/2 nuclei at thermal equilibrium, the deviation-populations (proportional to diagonal terms of deviation density matrix) are $\Delta\rho = I_z^1 + I_z^2 + I_z^3$ are $\{3, 1, 1, 1, -1, -1, -1, -3\}$. To prepare pseudopure state for 2^{nd} and 3^{rd} qubit subsystem, the populations between states $|001\rangle$ and $|101\rangle$, $|010\rangle$ and $|110\rangle$ are inverted by application of transition selective pulses as shown in Fig. 1.4. The new populations corresponding to subsystems $\{|000\rangle, |001\rangle, |010\rangle, |011\rangle\}$ and $\{|100\rangle, |101\rangle, |110\rangle, |111\rangle\}$ are respectively, $\{3, -1, -1, -1\}$, and $\{1, 1, 1, -3\}$ respectively. The deviation part of pseudopure state density matrix, corresponding to 0 and 1 subspace of 1^{st} qubit are $\Delta\rho^0 = 4|00\rangle\langle 00| - \mathbb{I}$ and $\Delta\rho^1 = \mathbb{I} - 4|11\rangle\langle 11|$.

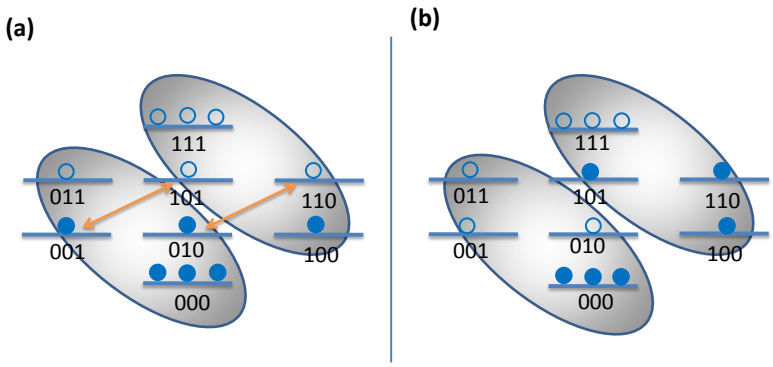

Figure 1.4: Populations (a) of density matrix for a homonuclear 3 spin system at thermal equilibrium and (b) of deviation density matrices $\Delta\rho^0$ and $\Delta\rho^1$

1.4.3 NMR quantum gates

In the following we give examples of some important single qubit gates and their NMR realization. We will describe single and multiple qubit gates.

1.4.3.1 Single qubit gates

The most important single qubit quantum gates are the NOT gate, Hadamard gate and the phase gate. In principle, one can always achieve any desired local rotation using at most three Euler angle rotations.

1.4.3.2 NOT-gate

It flips spin state $|0\rangle$ to $|1\rangle$ and vice-versa. In NMR, it can be realized by a π_x pulse [41] since

$$\pi_x = e^{-i\pi I_x} = -i\begin{bmatrix} 0 & 1 \\ 1 & 0 \end{bmatrix}. \tag{1.36}$$

Here the undetectable global phase can be ignored.

1.4.3.3 Hadamard gate

It prepares a qubit in state $|0\rangle$ into equal superposition of $|0\rangle$ and $|1\rangle$. In NMR it can be realized using the pulses $\left(\frac{\pi}{2}\right)_y \pi_x$, since

$$\left(\frac{\pi}{2}\right)_y \pi_x \equiv e^{-i\pi I_x} e^{-i\frac{\pi}{2} I_y} = \frac{1}{\sqrt{2}}\begin{bmatrix} 1 & 1 \\ 1 & -1 \end{bmatrix}, \tag{1.37}$$

up to a global phase.

1.4.3.4 Phase gate

A phase gate implements a rotation around $\hat{z}$-axis. For example the application of a phase gate ϕ on a qubit state prepared in equal superposition of two of its states introduces a

phase factor $e^{i\phi}$ to $|1\rangle$. In NMR, RF pulses can be applied only in the transverse direction, nevertheless a $\hat{z}$- rotation can be realized by a composite pulse using pulses of phases x and y (or by using chemical shift)

$$\phi_z = \pi_x \phi_y \pi_{-x} \equiv e^{-i\frac{\pi}{2}I_x} e^{-i\phi I_y} e^{i\frac{\pi}{2}I_x} = e^{-i\phi I_z} = e^{-i\frac{\phi}{2}} \begin{bmatrix} 0 & 0 \\ 0 & e^{i\phi} \end{bmatrix}. \tag{1.38}$$

1.4.3.5 Multiqubit gates

A general multiqubit gate can be realized with an appropriate combination of qubit selective RF pulses (local gates) and coupling interactions (nonlocal gates). An NMR pulse sequence to realize C- NOT gate is given below [41].

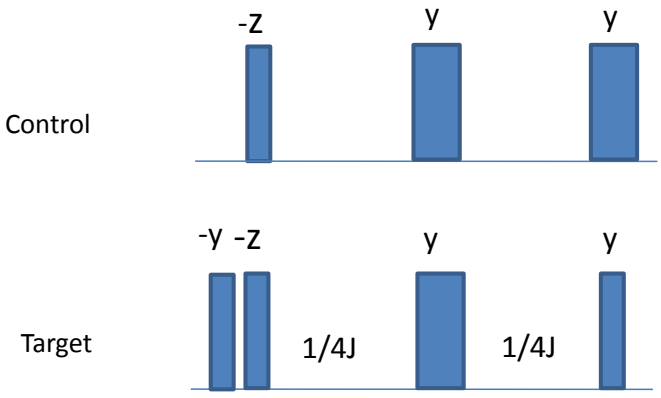

Figure 1.5: NMR pulse sequence for the C-NOT gate. Thin pulses are $\frac{\pi}{2}$ pulses and broad pulses are π pulses. Delay $\frac{1}{4J}$ represent free evolution under secular part of indirect spin-spin interaction.

1.4.4 Numerically optimized pulses

NMR quantum gates can be realized either by a combination of RF pulses and delays where evolution under internal Hamiltonian can take place. In a heteronuclear spin system, due to the large dispersion of Larmor frequencies and due to the availability of multichannel RF coils, it is easy to introduce spin-selective rotations. On the other hand, in the case of homonuclear systems, realizing spin-selective rotations is nontrivial, and often requires specially designed RF modulations [42]. Recently many numerical methods are available for this purpose. These methods not only take into account of complete Hamiltonian of the spin-system, but also attempt to realize gates that are robust against the experimental errors such as RF inhomogeneity (RFI) [42, 43].

Fig.1.6 shows a GRAPE modulation for a π_x pulse on a FFF spin system realized in NMR sample of iodotrifluoroethylene (C_2F_3I) and it's performance against RFI. The fidelity of the numerically generated pulse profile with respect to ideal pulse has been calculated using the expression 1.39

$$F = \frac{|\mathrm{Tr}[U_{targ}^{\dagger} U_{sim}]|}{N}. \tag{1.39}$$

Here $N = 2^n$ is the dimension of unitary operators.

1.5 Ancilla assisted quantum information processing (AAQIP)

1.5.1 System qubits and Ancilla qubits

In a QIP task those qubits which are under study are known as system qubits. The additional qubits which assist in this study but may or may not be measured at the end of the computation are often referred as ancilla qubits. Such ancilla qubits may be very useful in efficient implementation of certain QIP protocol.

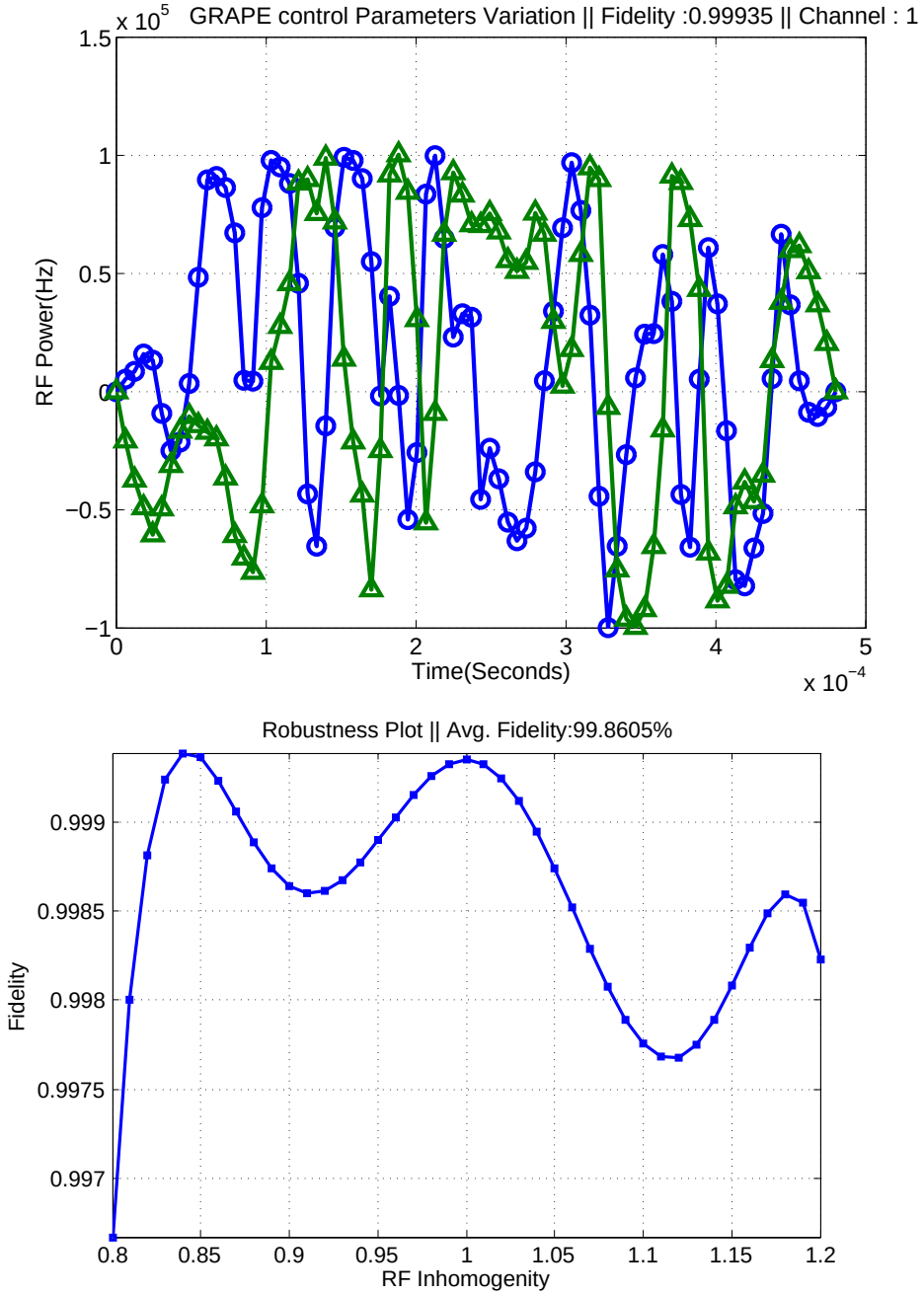

Figure 1.6: GRAPE generated RF profiles of π_x pulse on ^{19}F spins of iodotrifluoroethylene: X- component is shown in blue, Y- component is shown in green (top), and robustness profile against RFI (bottom).

1.5.2 Applications of ancilla qubits

Availability of ancilla qubits can be exploited in various ways. In the following I discuss three of them.

(i) **Extended work space:**

Consider a qubit system of size n in the state ρ, along with additional ancillary qubits n_a all prepared in the state ρ_a. Thus total number of the qubits in combined system and ancillary register are $\tilde{n} = n + n_a$. Now the state of the combined system can be written as $\tilde{\rho} = \rho \otimes \rho_a$. This extended space, can be exploited for efficient implementation of various QIP tasks. Below are the two cases where extended space is useful.

Characterization of quantum state: The extended Hilbert space allows a larger set of observables which can be simultaneously measured, and hence allow more efficient quantum state tomography of system qubits. This aspect is discussed in chapter 2.

Characterization of quantum process: The extended Hilbert space can also simultaneously encode different input states of the system qubits and hence allows more efficient quantum process tomography. This aspect is discussed in chapter 3.

(ii) **Non-invasive measurements:**

While a truly noninvasive quantum measurement is an idealized process, it is often possible to extract certain information about the quantum state via indirect measurement. One method involves letting the system qubits interact with ancilla qubits, and the measurement of ancilla qubits at a later stage, thus indirectly extracting the information about the system qubits. This aspect is discussed in chapter 4.

(iii) **Spectroscopy:**

We show in chapter 5 that the availability of ancilla qubits can be utilized for sensitive encoding of relative phase leading to certain interesting applications in spectroscopy. For example efficient measurement of translational diffusion constant and RF inhomogeneity.

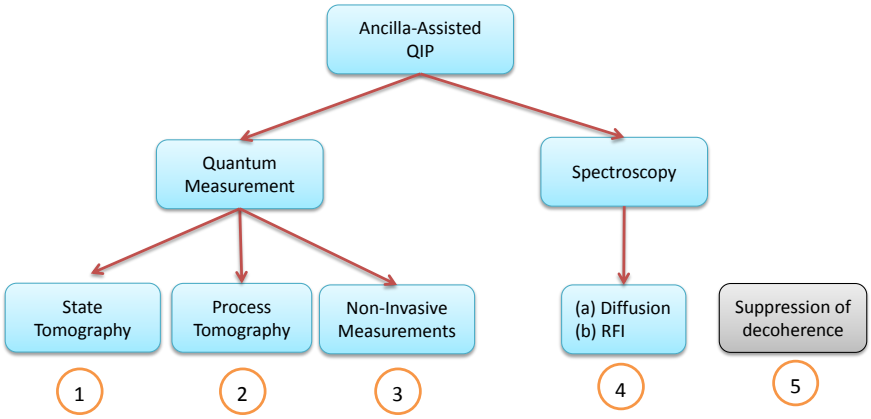

Figure 1.7: Topics studied in this thesis summarized as different chapters.

Figure 1.7 summarizes various QIP and spectroscopy related topics studied in this thesis.

Chapter 2

Ancilla assisted quantum state tomography

2.1 Introduction

Quantum computers have the potential to carry-out certain computational tasks with an efficiency that is beyond the reach of their classical counterparts [4]. In practice however, harnessing the computational power of a quantum system has been an enormously challenging task [44]. The difficulties include imperfect control on the quantum dynamics and omnipresent interactions between the quantum system and its environment leading to an irreversible loss of quantum coherence. In order to optimize the control fields and to understand the effects of environmental noise, it is often necessary to completely characterize the quantum state. In experimental quantum information studies, Quantum State Tomography (QST) is an important tool that is routinely used to characterize an instantaneous quantum state [4].

QST on an initial state is usually carried out to confirm the efficiency of initialization process. Though QST of the final state is usually not part of a quantum algorithm, it allows one to measure the fidelity of the output state. QSTs in intermediate stages often help experimentalists to tune-up the control fields better.

QST can be performed by a series of measurements of noncommuting observables which together enables one to reconstruct the complete complex density matrix. In the standard method, the required number of independent experiments grows exponentially with the number of input qubits [45,46]. Anil Kumar and co-workers have illustrated QST using a single two-dimensional NMR spectrum [47]. They showed that a two-dimensional NMR experiment consisting of a series of identical measurements with systematic increments in evolution time, can be used to quantitatively estimate all the elements of the density matrix. Later Nieuwenhuizen and co-workers have shown that it is possible to reduce the number of independent experiments in the presence of an ancilla register initialized to a known state [48]. They pointed out that in suitable situations, it is possible to carry-out QST with a single measurement of a set of factorized observables. We refer to this method

as Ancilla Assisted QST (AAQST). This method was experimentally illustrated by Suter and co-workers using a single input qubit and a single ancilla qubit [49]. Recently Peng and coworkers have studied the effectiveness of the method for qutrit-like systems using numerical simulations [50]. Single shot mapping of density matrix by AAQST method not only reduces the experimental time, but also alleviates the need to prepare the target state several times. Often slow variations in system Hamiltonian may result in systematic errors in repeating the state preparation. Further, environmental noises lead to random errors in multiple preparations. These errors play important roles in the quality of the reconstruction of the target state. Therefore AAQST has the potential to provide a more reliable way of tomography.

In this chapter, I first report our revisit of the theory of QST and AAQST and also provide methods for explicit construction of the constraint matrices, which will allow extending the tomography procedure for large registers. An important feature of the method described here is that it requires only global rotations and short evolutions under the collective internal Hamiltonian. I also describe our NMR demonstrations of AAQST on two different types of systems: (i) a two-qubit input register using a one-qubit ancilla in an isotropic liquid-state system and (ii) a three-qubit input register using a two-qubit ancilla register in a partially oriented system.

In the following §I briefly describe the theory of QST and AAQST. In §2.3 I describe experimental demonstrations and finally I conclude in §2.5.

2.2 Theory

2.2.1 Quantum State Tomography

We consider an n-qubit register formed by a system of n mutually interacting spin-1/2 nuclei with distinct resonance frequencies ω_i and mutual interaction frequencies $2\pi J_{ij}$. The Hamiltonian under weak-interaction limit ($2\pi J_{ij} \ll |\omega_i - \omega_j|$) consists of the Zeeman part and spin-spin interaction part, i.e.,

$$\mathcal{H} = -\sum_{i=1}^{n} \omega_i \sigma_z^i/2 + \sum_{i=1}^{n} \sum_{j=i+1}^{n} 2\pi J_{ij} \sigma_z^i \sigma_z^j/4 \tag{2.1}$$

respectively, where σ_z^i and σ_z^j are the z-components of Pauli operators of ith and jth qubits [34]. The set of $N = 2^n$ eigenvectors $\{|m_1 m_2 \cdots m_n\rangle\}$ of the Zeeman Hamiltonian form a complete orthonormal computational basis. We can order the eigenvectors based on the decimal value m of the binary string $(m_1 \cdots m_n)$, i.e., $m = m_1 2^{n-1} + \cdots + m_n 2^0$.

The general density matrix can be decomposed as $\mathbb{I}/N + \epsilon\rho$ where the identity part is known as the background, the trace-less part ρ is known as the *deviation density matrix*, and the dimensionless constant ϵ is the purity factor [38]. In this context, QST refers to complete characterization of the deviation density matrix, which can be expanded in terms of $N^2 - 1$ real unknowns:

$$\begin{aligned}\rho &= \sum_{m=0}^{N-2} \rho_{mm}(|m\rangle\langle m| - |N-1\rangle\langle N-1|) \\ &\quad + \sum_{m=0}^{N-2} \sum_{m'=m+1}^{N-1} \{R_{mm'}(|m\rangle\langle m'| + |m'\rangle\langle m|) + iS_{mm'}(|m\rangle\langle m'| - |m'\rangle\langle m|)\}. \end{aligned} \tag{2.2}$$

Here first part consists of $N - 1$ diagonal unknowns ρ_{mm} with the last diagonal element $\rho_{N-1,N-1}$ being constrained by the trace-less condition. R and S each consisting of $(N^2 - N)/2$ unknowns correspond to real and imaginary parts of the off-diagonal elements respectively. Thus a total of $N^2 - 1$ real unknowns needs to be determined.

Usually an experimental technique allows a particular set of observables to be measured directly. To explain the NMR case, we introduce n-bit binary strings, $j_\nu = \nu_1\nu_2\cdots\nu_{j-1}0\nu_j\cdots\nu_{n-1}$ and $j'_\nu = \nu_1\nu_2\cdots\nu_{j-1}1\nu_j\cdots\nu_{n-1}$ differed only by the flip of the jth bit. Here $\nu = \nu_1 2^{n-2} + \nu_2 2^{n-3} + \cdots + \nu_{n-1}2^0$ is the value of the $n-1$ bit binary string $(\nu_1, \nu_2, \cdots, \nu_{n-1})$ and ν can take a value between 0 and $\gamma = N/2 - 1$. The real and imaginary parts of an NMR signal recorded in a quadrature mode corresponds to the expectation values of transverse magnetization observables $\sum_{j=1}^{n} \sigma_{jx}$ and $\sum_{j=1}^{n} \sigma_{jy}$ respectively [34]. The background part of the density matrix neither evolves under unitaries nor gives raise to any signal, and therefore we ignore it. Under suitable conditions (when all the transitions are resolved), a single spectrum directly yields nN matrix elements $\{R_{j_\nu,j'_\nu}, S_{j_\nu,j'_\nu}\}$ as complex intensities of spectral lines. These matrix elements are often referred to as single quantum elements since they connect eigenvectors related by the flip of a single qubit.

We refer the single-quantum terms R_{j_ν,j'_ν} and S_{j_ν,j'_ν} respectively as the real and imaginary parts of νth spectral line of jth qubit. Thus a single spectrum of an n-qubit system in an arbitrary density matrix can yield nN real unknowns. In order to quantify the remaining elements, one relies on multiple experiments all starting from the same initial state ρ. The kth experiment consists of applying a unitary U_k to the state ρ, leading to $\rho^{(k)} = U_k \rho U_k^\dagger$, and measuring the single-quantum spectrum $\{R^{(k)}_{j_\nu,j'_\nu}, S^{(k)}_{j_\nu,j'_\nu}\}$. From eqn. (2.2) we obtain

$$\begin{aligned} R^{(k)}_{j_\nu,j'_\nu} &= \sum_m a^{(k)}_{j\nu}(m)\rho_{mm} + \sum_{m,m'>m} c^{(k)}_{j\nu}(m,m')R_{mm'} + e^{(k)}_{j\nu}(m,m')S_{mm'}, \\ S^{(k)}_{j_\nu,j'_\nu} &= \sum_m b^{(k)}_{j\nu}(m)\rho_{mm} + \sum_{m,m'>m} d^{(k)}_{j\nu}(m,m')R_{mm'} + f^{(k)}_{j\nu}(m,m')S_{mm'}, \end{aligned} \tag{2.3}$$

in terms of the unknowns $\rho_{mm'}$ and the known real constants $\{a, \cdots, f\}$:

$$\begin{aligned} a^{(k)}_{j\nu}(m,m) + ib^{(k)}_{j\nu}(m,m) &= \langle j_\nu|U_k|m\rangle\langle m|U_k^\dagger|j'_\nu\rangle - \langle j_\nu|U_k|N-1\rangle\langle N-1|U_k^\dagger|j'_\nu\rangle, \\ c^{(k)}_{j\nu}(m,m') + id^{(k)}_{j\nu}(m,m') &= \langle j_\nu|U_k|m\rangle\langle m'|U_k^\dagger|j'_\nu\rangle + \langle j_\nu|U_k|m'\rangle\langle m|U_k^\dagger|j'_\nu\rangle, \\ e^{(k)}_{j\nu}(m,m') + if^{(k)}_{j\nu}(m,m') &= i\langle j_\nu|U_k|m\rangle\langle m'|U_k^\dagger|j'_\nu\rangle - i\langle j_\nu|U_k|m'\rangle\langle m|U_k^\dagger|j'_\nu\rangle \end{aligned} \tag{2.4}$$

[51]. After K experiments, we can setup the matrix equation

$$
M \begin{bmatrix}
\rho_{0,0} \\
\cdots \\
\rho_{N-2,N-2} \\
---------- \\
R_{0,1} \\
\cdots \\
R_{0,N-1} \\
\cdots \\
R_{m,m'>m} \\
\cdots \\
R_{N-2,N-1} \\
---------- \\
S_{0,1} \\
\cdots \\
S_{0,N-1} \\
\cdots \\
S_{m,m'>m} \\
\cdots \\
S_{N-2,N-1}
\end{bmatrix}
=
\begin{bmatrix}
R^{(1)}_{1_0,1'_0} \\
\cdots \\
R^{(1)}_{1_\gamma,1'_\gamma} \\
R^{(1)}_{2_0,2'_0} \\
\cdots \\
\cdots \\
R^{(K)}_{n_\gamma,n'_\gamma} \\
-------- \\
S^{(1)}_{1_0,1'_0} \\
\cdots \\
S^{(1)}_{1_\gamma,1'_\gamma} \\
S^{(1)}_{2_0,2'_0} \\
\cdots \\
\cdots \\
S^{(K)}_{n_\gamma,n'_\gamma}
\end{bmatrix}. \tag{2.5}
$$

Here the left column vector is formed by the N^2-1 unknowns of ρ: diagonal elements in the top, real off-diagonals in the middle, and imaginary off-diagonals in the bottom. The right column vector is formed by KnN numbers - the real and imaginary parts of the experimentally obtained spectral intensities ordered according to the value of the binary string ν, the qubit number j, and the experiment number k. The $KnN\times(N^2-1)$ dimensional

constraint matrix is of the form

$$M = \left[\begin{array}{cccccc|cccccc|cccccc}
a^{(1)}_{1,0}(0,0) & \cdots & c^{(1)}_{1,0}(m,m') & \cdots & e^{(1)}_{1,0}(m,m') & \cdots \\
\cdots & \cdots & \cdots & \cdots & \cdots & \cdots \\
a^{(1)}_{1,\gamma}(0,0) & \cdots & c^{(1)}_{1,\gamma}(m,m') & \cdots & e^{(1)}_{1,\gamma}(m,m') & \cdots \\
\cdots & \cdots & \cdots & \cdots & \cdots & \cdots \\
a^{(1)}_{n,0}(0,0) & \cdots & c^{(1)}_{n,0}(m,m') & \cdots & e^{(1)}_{n,0}(m,m') & \cdots \\
\cdots & \cdots & \cdots & \cdots & \cdots & \cdots \\
\cdots & \cdots & \cdots & \cdots & \cdots & \cdots \\
a^{(K)}_{n\gamma}(0,0) & \cdots & c^{(K)}_{n\gamma}(m,m') & \cdots & e^{(K)}_{n\gamma}(m,m') & \cdots \\
\hline
b^{(1)}_{1,0}(0,0) & \cdots & d^{(1)}_{1,0}(m,m') & \cdots & f^{(1)}_{1,0}(m,m') & \cdots \\
\cdots & \cdots & \cdots & \cdots & \cdots & \cdots \\
b^{(1)}_{1,\gamma}(0,0) & \cdots & d^{(1)}_{1,\gamma}(m,m') & \cdots & f^{(1)}_{1,\gamma}(m,m') & \cdots \\
\cdots & \cdots & \cdots & \cdots & \cdots & \cdots \\
b^{(1)}_{n,0}(0,0) & \cdots & d^{(1)}_{n,0}(m,m') & \cdots & f^{(1)}_{n,0}(m,m') & \cdots \\
\cdots & \cdots & \cdots & \cdots & \cdots & \cdots \\
\cdots & \cdots & \cdots & \cdots & \cdots & \cdots \\
b^{(K)}_{n\gamma}(0,0) & \cdots & d^{(K)}_{n\gamma}(m,m') & \cdots & f^{(K)}_{n\gamma}(m,m') & \cdots
\end{array}\right]. \tag{2.6}$$

Note that each column of the constraint matrix corresponds to contribution of a particular unknown element of ρ to the various spectral intensities. By choosing the unitaries $\{U_k\}$ such that $\text{rank}(M) \geq N^2 - 1$ (the number of unknowns), eqn. (2.5) can be solved either by singular value decomposition or by Gaussian elimination method [51]. Fig. 2.1 illustrates the minimum number (K) of experiments required for QST. As anticipated, K increases rapidly as $O(N/n)$ with the number of input qubits. In the following we describe how it is possible to speed-up QST, in the presence of an ancilla register, with fewer experiments.

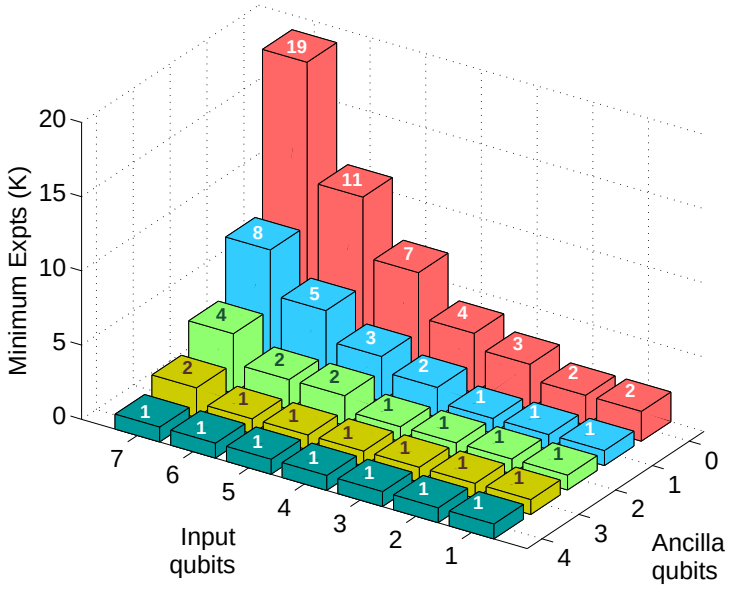

Figure 2.1: Minimum number of independent experiments required in QST (without ancilla) and AAQST (with different number of ancilla register).

2.2.2 Ancilla Assisted QST (AAQST)

Suppose the input register of n-qubits is associated with an ancilla register consisting of $\hat{n}$ qubits. The dimension of the combined system of $\tilde{n} = n + \hat{n}$ qubits is $\tilde{N} = N\hat{N}$, where $\hat{N} = 2^{\hat{n}}$. For simplicity we assume that each qubit interacts sufficiently with all other qubits so as to obtain a completely resolved spectrum yielding $\tilde{n}\tilde{N}$ real parameters. Following method is applicable even if there are spectral overlaps, albeit with lower efficiency (i.e., with higher number (K) of minimum experiments). Further for simplicity, we assume that the ancilla register begins with the maximally mixed initial state, with no contribution to the spectral lines from it. Otherwise, we need to add the contribution of the ancilla to the final spectrum and the eqn. (2.5) will become inhomogeneous. As explained later in the experimental section, initialization of maximally mixed state can be achieved with high precision. Thus the deviation density matrix of the combined system is $\tilde{\rho} = \rho \otimes \mathbb{I}/\hat{N}$. Now applying only local unitaries neither leads to ancilla coherences nor transfers any of the input coherences to ancilla. Therefore we consider applying a non-local unitary exploiting

the input-ancilla interaction,

$$\tilde{U}_k = V \sum_{a=0}^{\hat{N}-1} U_{ka} \otimes |a\rangle\langle a|, \tag{2.7}$$

where U_{ka} is the kth unitary on the input register dependent on the ancilla state $|a\rangle$ and V is the local unitary on the ancilla. The combined state evolves to

$$\begin{aligned} \tilde{\rho}^{(k)} &= \tilde{U}_k \tilde{\rho} \tilde{U}_k^\dagger \\ &= \frac{1}{\hat{N}} \sum_{m,m',a} \rho_{mm'} U_{ka} |m\rangle\langle m'| U_{ka}^\dagger \otimes V|a\rangle\langle a|V^\dagger. \end{aligned} \tag{2.8}$$

We now record the spectrum of the combined system corresponding to the observable $\sum_{j=1}^{\tilde{n}} \sigma_{jx} + i\sigma_{jy}$. Each spectral line can again be expressed in terms of the unknown elements of the ancilla matrix in the form given in eqn. (2.3). The spectrum of the combined system yields $\tilde{n}\tilde{N}$ linear equations. The minimum number of independent experiments needed is now $O(N^2/(\tilde{n}\tilde{N}))$. Since we can choose $\tilde{N} \gg N$, AAQST needs fewer than O(N/n) experiments required in the standard QST. In particular, when $\tilde{n}\tilde{N} \geq N^2$, a single optimized unitary suffices for QST. Fig. 2.1 illustrates the minimum number (K) of experiments required for various sizes of input and ancilla registers. As illustrated, QST can be achieved with only one experiment, if an ancilla of sufficient size is provided along with.

2.2.3 Building the constraint matrix

The major numerical procedure in AAQST is obtaining the constraint matrix M. For calculating the constraint coefficients $c_{rj}^{(k)}$, one may utilize an elaborate decomposition of U_k using numerical or analytical methods. Alternatively, as described below, we can use a simple algorithmic approach to construct the constraint matrix.

First imagine a diagonal state ρ for the ancilla register (eqn. (2.2)) with $\rho_{00} = 1$ and $\rho_{mm} = 0$ for all other $1 \leq m \leq N-2$, $R_{mm'} = S_{mm'} = 0$. Applying the unitary U_k on the composite deviation density matrix $\tilde{\rho} = \rho \otimes \mathbb{I}/\hat{N}$, we obtain all the spectral intensities

(using eqn. (2.3))

$$a^k_{j\nu}(0,0) = R^{(k)}_{j\nu,j\nu'},\ b^k_{j\nu}(0,0) = S^{(k)}_{j\nu,j\nu'}. \tag{2.9}$$

Thus the spectral lines indicate the contributions only from ρ_{00} (and $\rho_{N-1,N-1}$). Repeating the process with all the unitaries $\{U_k\}$ yields the first column in M matrix (eqn. (2.6)) corresponding to the unknown ρ_{00}. Same procedure can be used for all the diagonal elements ρ_{mm} with $0 \leq m \leq N-2$. To determine M matrix column corresponding to a real off-diagonal unknown $R_{mm'}$, we start with an input-register density matrix $R_{mm'} = 1$ and all other elements set to zero. Again by applying the unitary U_k on the composite density matrix, and using eqn. (2.3) we obtain

$$c^k_{j\nu}(m,m') = R^{(k)}_{j\nu,j\nu'},\ d^k_{j\nu}(m,m') = S^{(k)}_{j\nu,j\nu'}. \tag{2.10}$$

Repeating the process with all unitaries $\{U_k\}$ determines the column of M corresponding to the unknown $R_{mm'}$.

To determine M matrix column corresponding to an imaginary off-diagonal unknown $S_{mm'}$, we set $S_{mm'} = 1$ and all other elements to zero, and apply U_k on the composite state to obtain

$$e^k_{j\nu}(m,m') = R^{(k)}_{j\nu,j\nu'},\ f^k_{j\nu}(m,m') = S^{(k)}_{j\nu,j\nu'}. \tag{2.11}$$

Proceeding this way, by selectively setting the unknowns one by one, the complete constraint matrix can be built easily.

2.2.4 Optimization of Unitaries

Solving the matrix equation (2.5) requires that $\text{rank}(M) \geq N^2-1$, the number of unknowns. But having the correct rank is not sufficient. The matrix M must be well conditioned in order to ensure that small errors in the observed intensities $\{R^{(k)}_{j\nu,j\nu'}, S^{(k)}_{j\nu,j\nu'}\}$ do not contribute to large errors in the values of the elements $\rho_{mm'}$. The quality of the constraint matrix can be measured by a scalar quantity called condition number $C(M)$ defined as the ratio of

the largest singular value of M to the smallest [52]. Smaller the value of $C(M)$, better conditioned is the constraint matrix M for solving the unknowns. Thus the condition number provides a convenient scalar quantity to optimize the set $\{U_k\}$ of unitaries to be selected for QST. As explained in the experimental section, we used a simple unitary model $U_1(\tau_1, \tau_2)$ as an initial guess and used genetic algorithm to minimize the condition number and optimize the parameters (τ_1, τ_2). The necessary number (K) of independent experiments is decided by the rank of the constraint matrix and the desired precision. The rank condition requires that $KnN \geq N^2 - 1$. Introducing additional experiments renders the problem over-determined, thus reducing the condition number and increasing the precision. In the following section we describe the experimental results of AAQST for registers with (i) $n = 2, \hat{n} = 1, \tilde{n} = 3$ and (ii) $n = 3, \hat{n} = 2, \tilde{n} = 5$ respectively.

2.3 Experiments

We report experimental demonstrations of AAQST on two spin-systems of different sizes and environments. In each case, we have chosen two density matrices for tomography. All the experiments described below are carried out on a Bruker 500 MHz spectrometer at an ambient temperature of 300 K using high-resolution nuclear magnetic resonance techniques. In the following, we describe experimental implementation of AAQST on two different spin systems.

2.3.1 Two-qubit input, One-qubit ancilla

Here we use three spin-1/2 ^{19}F nuclei of iodotrifluoroethylene (C_2F_3I) dissolved in acetone-D_6 as a 3-qubit system. The molecular structure and the Hamiltonian parameters are given in upper trace of Fig. 2.2. Single quantum transitions of each spin, labelled by other spin states are also shown in Fig. 2.2(a, b, c). As can be seen in Fig.2.4, all the 12 transitions of this system are clearly resolved.

The pulse sequence for the AAQST experiment is shown in Fig. 2.3. We have chosen F_1 as the ancilla qubit and F_2 and F_3 as the input qubits. QST was performed for two different density matrices (i) thermal equilibrium state, i.e., $\rho_1 = \frac{1}{2}\left(\sigma_z^2 + \sigma_z^3\right)$,

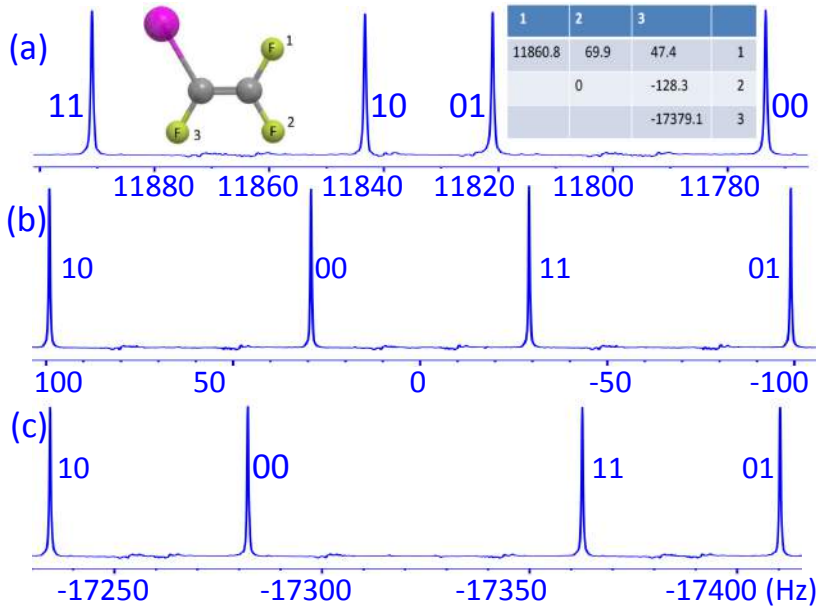

Figure 2.2: Molecular structure of iodotrifluoroethylene and the table of Hamiltonian parameters in Hz: chemical shifts (diagonal elements) and J-coupling constants (off-diagonal elements) are given in upper trace. Single quantum transitions of (a) F_1, (b) F_2, and (c) F_3 spins, labelled by states of other spins are also shown.

and (ii) state after a $(\pi/4)_{\pi/4}$ pulse applied to the thermal equilibrium state, i.e., $\rho_2 = \frac{1}{2}\left(\sigma_x^2 + \sigma_x^3\right) - \frac{1}{2}\left(\sigma_y^2 + \sigma_y^3\right) + \frac{1}{\sqrt{2}}\left(\sigma_z^2 + \sigma_z^3\right)$. In both the cases, the first qubit was initialized into a maximally mixed state by applying a selective $(\pi/2)_y$ pulse on F_1 and followed by a strong pulsed-field-gradient (PFG) in the z-direction. The selective pulse was realized by GRAPE technique [43].

AAQST of each of the above density matrices required just one unitary evolution followed by the measurement of complex NMR signal. We modelled the AAQST unitary as follows: $U_1 = \left(\frac{\pi}{2}\right)_y U_{\text{int}}(\tau_2)\left(\frac{\pi}{2}\right)_x U_{\text{int}}(\tau_1)$, where $U_{\text{int}}(\tau) = \exp(-i\mathcal{H}\tau)$ is the unitary operator for evolution under the internal Hamiltonian $\mathcal{H}$ (see eqn. (3.7)) for a time τ, and $\left(\frac{\pi}{2}\right)$ rotations are realized by non selective radio frequency pulses applied to all the spins along the directions indicated by the subscripts. The constraint matrix M had 15 columns corresponding to the unknowns and 24 rows corresponding to the real and imaginary parts of the 12 spectral lines. Only the durations $\{\tau_1, \tau_2\}$ needed to be optimized to minimize the condition number $C(M)$. We used a genetic algorithm for the optimization and obtained $C(M) = 17.3$ for $\tau_1 = 6.7783$ ms and $\tau_2 = 8.0182$ ms. The real and imaginary parts

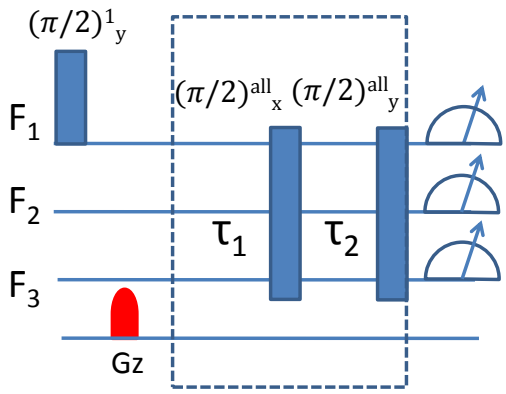

Figure 2.3: The pulse sequence for two qubit AAQST. A $\frac{\pi}{2}$ pulse followed by a gradient prepares first spin into maximally mixed state. The pulse sequence corresponding to unitary U_1 is shown inside the dotted block. Unitaries $U_{int}(\tau_1)$ and $U_{int}(\tau_2)$ are realized by delays τ_1 and τ_2. The $\frac{\pi}{2}^{all}$ are shown by solid boxes.

of the single shot experimental AAQST spectrum, along with the reference spectrum, are shown in the top part of Fig. 2.4. The intensities $\{R^{(1)}_{jv,jv'}, S^{(1)}_{jv,jv'}\}$ were obtained by simple curve-fit routines, and the matrix eqn. (2.5) was solved to obtain all the unknowns. The reconstructed density matrices along with the theoretically expected ones are shown below the spectra in Fig. 2.4. The fidelities of experimental states with the theoretically expected states (ρ_1 and ρ_2) are respectively 0.998 and 0.990. The high fidelities indicated successful AAQST of the prepared states.

2.3.2 Three-qubit input, Two-qubit ancilla

We use three ^{19}F nuclei and two ^{1}H nuclei of 1-bromo-2,4,5-trifluorobenzene partially oriented in a liquid crystal namely, N-(4-methoxybenzaldehyde)-4- butylaniline (MBBA). Due to the partial orientational order, the direct spin-spin interaction (dipolar interaction) does not get fully averaged out, but gets scaled down by the order parameter [53]. The molecular structure, the chemical shifts, the strengths of the effective couplings, and ^{1}H and ^{19}F spectra of the above sample are shown in Fig. 2.5 and 2.6. Single quantum transitions corresponding to each spins as shown in Fig. 2.5(c, d, e) and Fig. 2.6a, b, c are labelled by states of other spins.are shown in Fig. 2.5a and Fig. 2.5b. As is evident, the

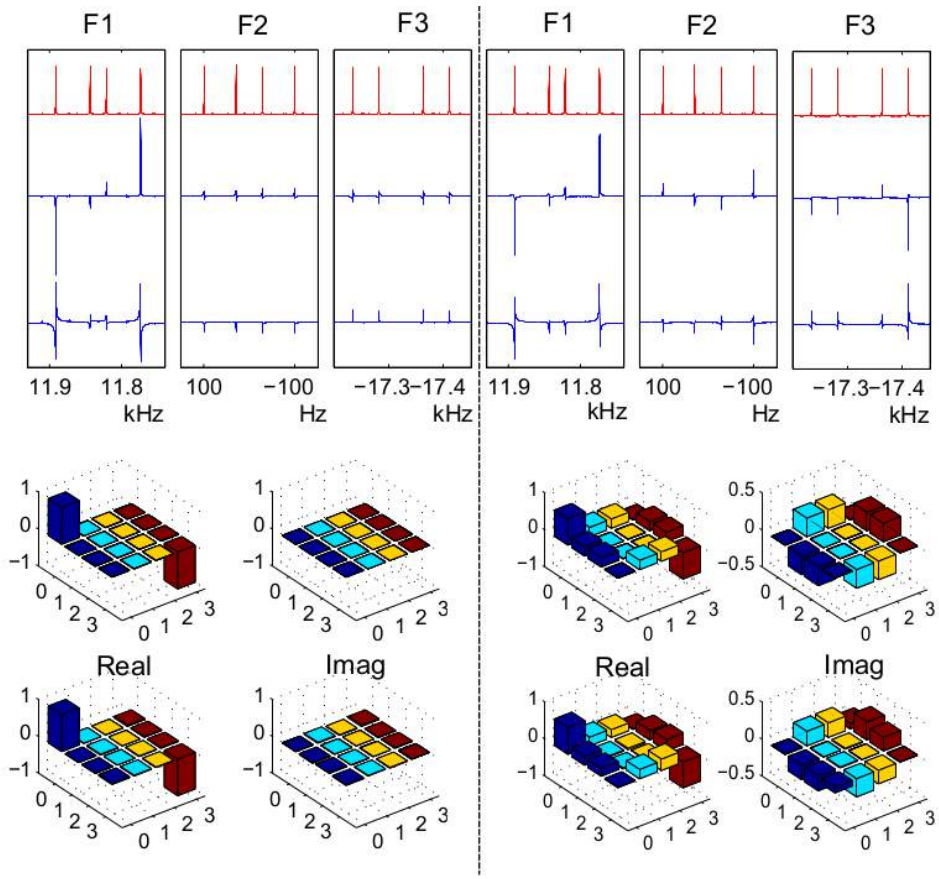

Figure 2.4: AAQST results for thermal equilibrium state ρ_1 (left column), and that of state ρ_2 (right column), described in the text. The reference spectra is in the top trace. The spectra corresponding to the real part ($R^{(1)}_{jv,jv'}$, middle trace) and the imaginary part ($S^{(1)}_{jv,jv'}$, bottom trace) of the ^{19}F signal are obtained in a single shot AAQST experiment. The bar plots correspond to theoretically expected states (top row) and those obtained from AAQST experiments (bottom row). Fidelities of the states are 0.997 and 0.99 respectively for the two density matrices.

partially oriented system can display stronger and longer-range coupling network leading to a larger register. Here we choose the three ^{19}F nuclei forming the input register and two ^{1}H nuclei forming the ancilla register. The Hamiltonian for the heteronuclear dipolar interaction (between ^{1}H and ^{19}F) has an identical form as that of J-interaction [53]. The homonuclear dipolar couplings (among ^{19}F, as well as among ^{1}H nuclei) were small compared to their chemical shift differences enabling us to approximate the Hamiltonian in the form of eqn. (3.7).

The partially oriented spin-system yields all the 80 transitions sufficiently resolved.

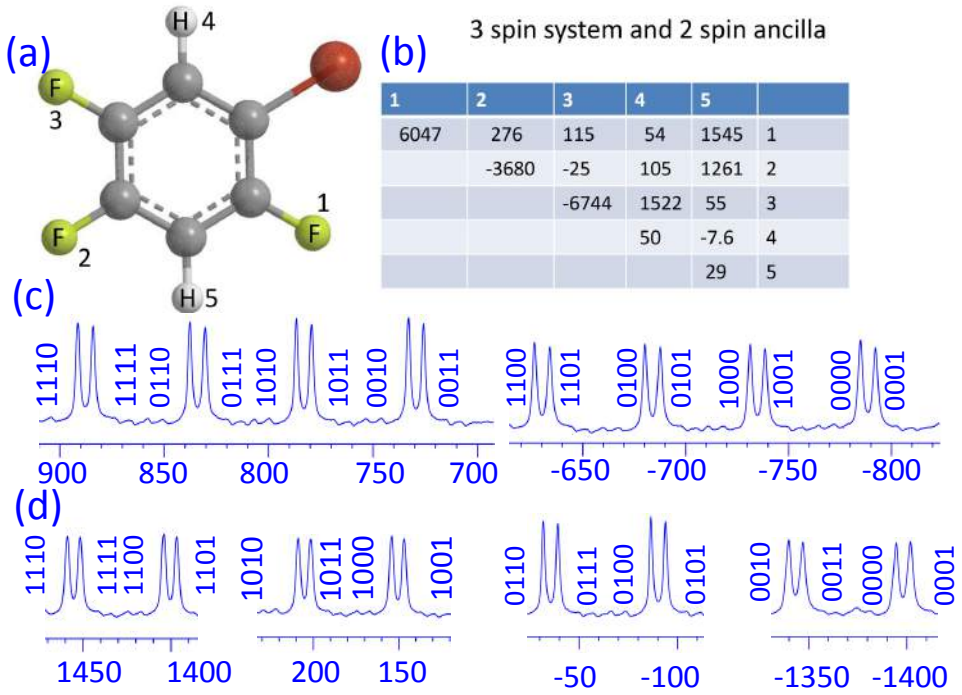

Figure 2.5: (a) Molecular structure and (b) the table of Hamiltonian parameters of 1-bromo 2,4,5- trifluorobenzene in Hz: chemical shifts (diagonal elements) and J-coupling constants (off-diagonal elements). Single quantum transitions for (c) H_4, (d) H_5 spins, labelled by states of other spins are also shown.

Again we use just one experiment for the complete AAQST of the 3-qubit input register. We modelled the AAQST unitary in a similar way as before: $U_1 = \left(\frac{\pi}{2}\right)_x U_{\text{int}}(\tau_2) \left(\frac{\pi}{2}\right)_x U_{\text{int}}(\tau_1)$ where $U_{\text{int}}(\tau) = \exp(-i\mathcal{H}\tau)$ is the unitary operator for evolution under the internal Hamiltonian $\mathcal{H}$ (see eqn. (3.7)) for a time τ, and $\left(\frac{\pi}{2}\right)_x$ are global x-rotations. The constraint matrix M had 63 columns corresponding to the unknowns and 160 rows corresponding to the real and imaginary parts of 80 spectral lines. After optimizing the durations by minimizing the condition number using a genetic algorithm, we obtained $C(M) = 14.6$ for $\tau_1 = 431.2\mu$s and $\tau_2 = 511.5\mu$s. Again we study AAQST on two states: (i) Thermal equilibrium of the ^{19}F spins: $\rho_1 = (\sigma_z^1 + \sigma_z^2 + \sigma_z^3)/2$, and (ii) a random density matrix ρ_2 obtained by applying unitary $U_0 = \left(\frac{\pi}{2}\right)_x^F \tau_0(\pi)_x^H \tau_0 \left(\frac{\pi}{2}\right)_y^{F_1}$, with $\tau_0 = 2.5$ ms, on thermal equilibrium state, i.e., $\rho_2 = U_0 \rho_1 U_0^\dagger$. In both the cases, we initialize the ancilla i.e., the ^{1}H qubits on to a maximally mixed state by first applying a $(\pi/2)^H$ pulse followed by a strong PFG in the z-direction. The real and imaginary parts of the single shot AAQST spectra,

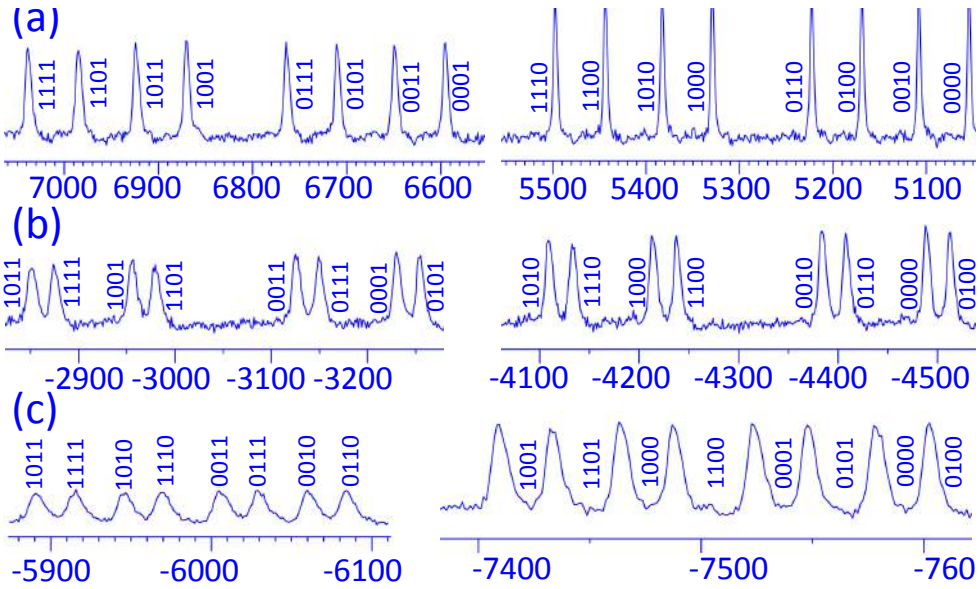

Figure 2.6: Single quantum transitions of (a) F_1, (b) F_2, and (c) F_3 spins in 1-bromo-2,4,5-trifluorobenzene are shown. Transitions are labelled by states of other spins.

along with the reference spectra, are shown in Figs. 2.7 and 2.8 respectively. Again the line intensities $\{R^{(1)}_{j\nu,j\nu'}, S^{(1)}_{j\nu,j\nu'}\}$ are obtained by curve-fitting, and all the 63 unknowns of the 3-qubit deviation density matrix are obtained by solving the matrix eqn. (2.5). The reconstructed density matrices along with the theoretically expected states (ρ_1 and ρ_2) are shown below the spectra in Figs. 2.7 and 2.8. The fidelities of experimental states with the theoretically expected states (ρ_1 and ρ_2) are respectively 0.98 and 0.95. The lower fidelity in the latter case is mainly due the imperfections in the preparation of the target state ρ_2. The overall poorer performance in the liquid crystal system is due to the lower fidelities of the QST pulses, spatial and temporal variations of solute order-parameter, and stronger decoherence rates compared to the isotropic case. In spite of these difficulties, the three-qubit density matrix with 63 unknowns could be estimated quantitatively through a single NMR experiment.

2.4 Robustness

We have also simulated the robustness of the AAQST protocal against simulated noise and the results are shown in Fig. 2.9. To realize a noisy experimental output we have

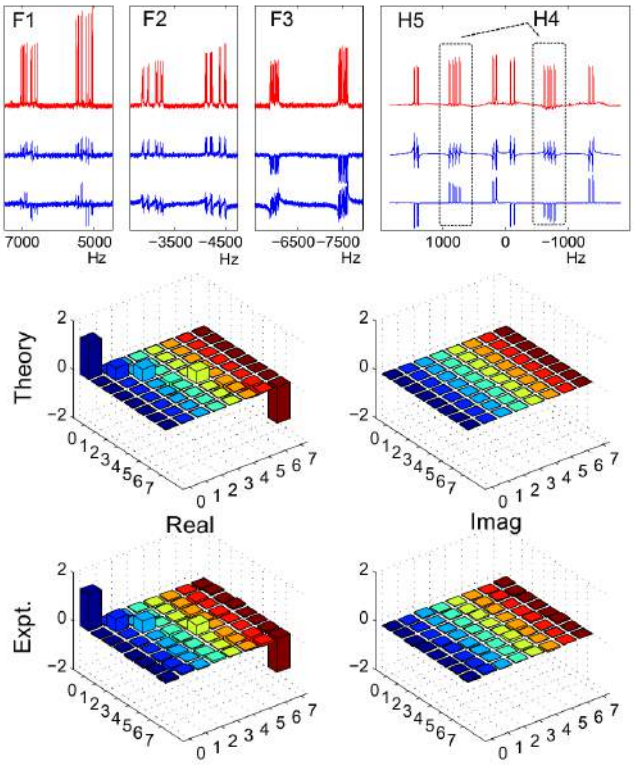

Figure 2.7: AAQST results for thermal equilibrium state, i.e., $(\sigma_z^1 + \sigma_z^2 + \sigma_z^3)/2$. The reference spectrum is in the top trace. The spectra corresponding to the real part ($R^{(1)}_{j\nu,j\nu'}$, middle trace) and the imaginary part ($R^{(1)}_{j\nu,j\nu'}$, bottom trace) of the ^{19}F signal are obtained in a single shot AAQST experiment. The bar plots correspond to theoretically expected states (top row) and those obtained from AAQST experiments (bottom row). Fidelity of the AAQST state is 0.98.

we have externally added the noise (a random-number array) into the measured output signals before reconstructing the density matrix. This procedure has been repeated for the various noise levels η. The average fidelity drop against the corresponding noise level for all four cases namely two-qubit input, single-qubit ancilla (ρ_1 and ρ_2) and three-qubit input, two-qubit ancilla (ρ_1 and ρ_2) are shown.

2.5 Conclusions

Quantum state tomography is an important part of experimental studies in quantum information processing. The standard method involves a large number of independent measurements to reconstruct a density matrix. The ancilla-assisted quantum state tomography

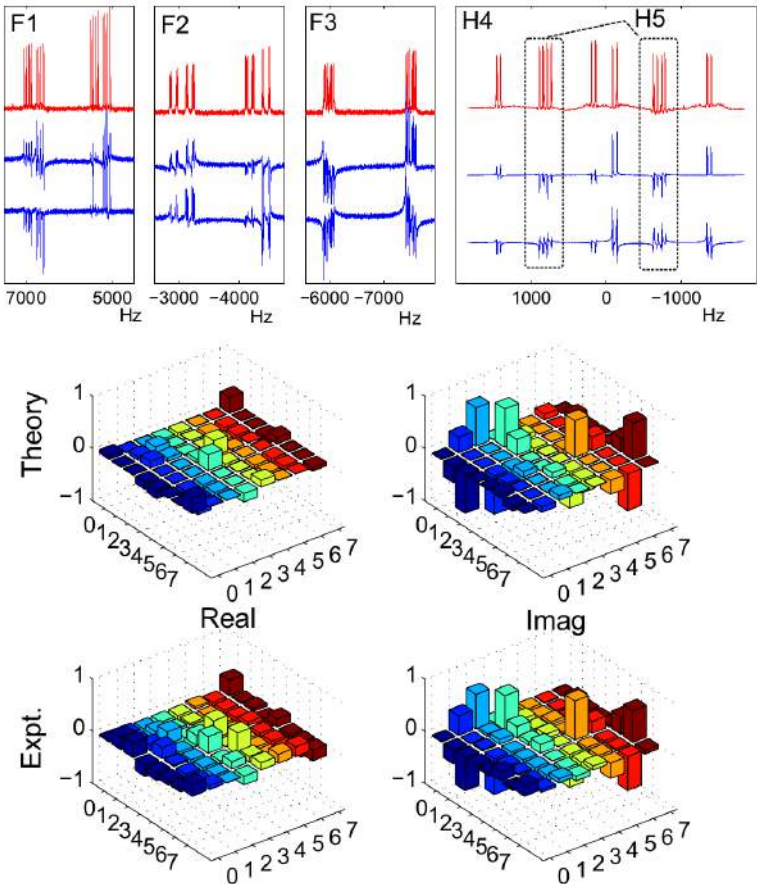

Figure 2.8: AAQST results for the state ρ_2 described in the text. The reference spectrum is in the top trace. The real (middle trace) and the imaginary spectra (bottom trace) are obtained in a single shot AAQST experiment. The bar plots correspond to theoretically expected states (top row) and those obtained from AAQST experiments (bottom row). Fidelity of the AAQST state is 0.95.

introduced by Nieuwenhuizen and co-workers allows complete reconstruction of complex density matrix with fewer experiments by letting the unknown state of the input register to interact with an ancilla register initialized in a known state. Ancilla registers are essential in many of the quantum algorithms. Usually, at the end of the quantum algorithms, ancilla is brought to a state which is separable with the input register. The same ancilla register which is used for computation can be utilized for tomography after the computation. The ancilla register can be prepared into a maximally mixed state by dephasing all the coherences and equalizing the populations. We provided methods for explicit construction of tomography matrices in large registers. We also discussed the optimization of tomogra-

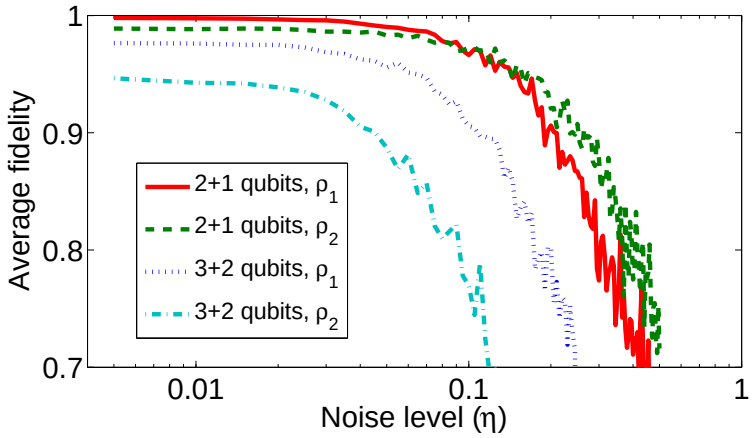

Figure 2.9: Average fidelity of the characterised state for simulated noise level. The simulation procedure is described in the text. We have carried out this study for all four experimentally characterised density matrices as shown in the legend. The expressions for density matrices ρ_1 and ρ_2 are mentioned in §2.3.1 and §2.3.2. Results show robustness of the protocal

.

phy experiments based on minimization of the condition number of the constraint matrix. Finally, we demonstrated the experimental ancilla-assisted quantum state tomography in two systems: (i) a system with two input qubits and one ancilla qubit in an isotropic medium and (ii) a system with three input qubits and two ancilla qubits in a partially oriented medium. In both the cases, we successfully reconstructed the target density matrices with a single quadrature detection of transverse magnetization. The methods introduced in this work should be useful for extending the range of quantum state tomography to larger registers.

Chapter 3

Single-scan quantum process tomography

3.1 Introduction

An open quantum system may undergo an evolution due to intentional control fields as well as due to unintentional interactions with stray fields caused by environmental fluctuations. In practice, even a carefully designed control field may be imperfect to the extent that one might need to characterize the overall process acting on the quantum system. Such a characterization, achieved by a procedure called quantum process tomography (QPT), is crucial in the physical realization of a fault-tolerant quantum processor [54, 55]. QPT is realized by considering the quantum process as a map from a complete set of initial states to final states, and experimentally characterizing each of the final states using quantum state tomography (QST) [45]. Since the spectral decomposition of a density matrix may involve noncommuting observables, Heisenberg's uncertainty principle demands multiple experiments to characterize the quantum state. Thus QST by itself involves the measurement of a series of observables after identical preparations of the system in the quantum state. Hence, QPT in general requires a number of independent experiments, each involving initialization of the quantum system, applying the process to be characterized, and finally QST. Furthermore, the total number of independent measurements required for QPT increases exponentially with the size of the system undergoing the process.

The physical realization of QPT has been demonstrated on various experimental setups such as NMR [56, 57], linear optics [58–61], ion traps [62, 63], superconducting qubits [64–69], and NV center qubit [70]. Several developments in the methodology of QPT have also been reported [71, 72]. In particular, it has been shown that ancilla assisted process tomography (AAPT) can characterize a process with a single QST [58, 59, 73, 74]. However, it still requires multiple measurements each taken over a set of commuting observables. On the other hand, if sufficient ancilla qubits are available, QST can be carried out with a single ensemble measurement (i.e., a single scan) over the entire system-ancilla

space. This procedure, known as ancilla assisted quantum state tomography (AAQST), has been studied both theoretically and experimentally [48–50, 64, 75]. Here we combine AAPT with AAQST and realize a 'single-scan quantum process tomography' (SSPT), which can characterize a general process in a single ensemble measurement of the system-ancilla state.

In the next section, after briefly revising QPT and AAPT, I describe SSPT procedure. In §3.3, I illustrate our SSPT procedure using a three-qubit NMR quantum register. I also present our characterization of certain unitary processes corresponding to standard quantum gates and a nonunitary process, namely twirling operation. Finally I conclude in §3.4.

3.2 Theory

3.2.1 Quantum Process Tomography (QPT)

A process ε maps a quantum state ρ to another state $\varepsilon(\rho)$. Here we consider an n-qubit system with $N^2(= 2^{2n})$-dimensional Liouville space S. In order to characterize ε, we let the process act on each linearly independent element of a complete basis set $\{\rho_1, \rho_2, \cdots, \rho_{N^2}\}$. Expressing each output state in the complete basis we obtain

$$\varepsilon(\rho_j) = \sum_k \lambda_{jk}\rho_k, \tag{3.1}$$

where the complex coefficients λ_{jk} can be extracted after QST.

The outcome of a trace-preserving quantum process ε also has an operator-sum representation

$$\varepsilon(\rho) = \sum_i E_i \rho E_i^\dagger, \tag{3.2}$$

where the *Kraus operators* E_i satisfy the completeness relation $\sum_i E_i^\dagger E_i = \mathbb{I}$. To assist experimental characterization of the process, we utilize a fixed set of basis operators $\{\tilde{E}_m\}$,

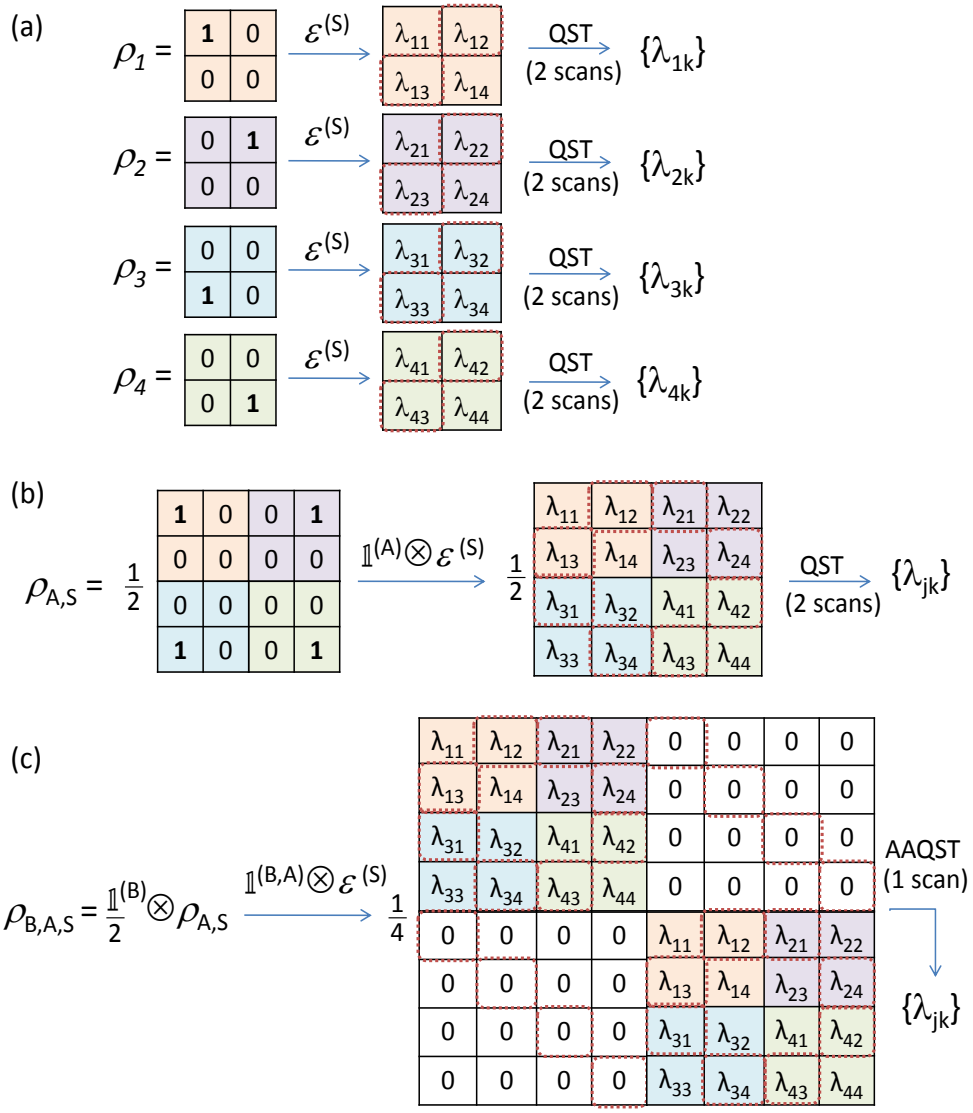

Figure 3.1: Illustrating (a) single-qubit QPT requiring a total of 8 NMR measurements, (b) AAPT requiring 2 NMR measurements, and (c) SSPT requiring a single NMR measurement.

and express $E_i = \sum_m e_{im}\tilde{E}_m$. The process is now described by

$$\varepsilon(\rho) = \sum_{mn} \tilde{E}_m \rho \tilde{E}_n^\dagger \chi_{mn}, \tag{3.3}$$

where $\chi_{mn} = \sum_i e_{im} e_{in}^*$ form a complex matrix which completely characterizes the process ε. Since the set $\{\rho_k\}$ forms a complete basis, it is also possible to express

$$\tilde{E}_m \rho_j \tilde{E}_n^\dagger = \sum_k \beta_{jk}^{mn} \rho_k, \tag{3.4}$$

where β_{jk}^{mn} can be calculated theoretically. Eqns. 3.1, 3.3, and 3.4 lead to

$$\varepsilon(\rho_j) = \sum_k \lambda_{jk}\rho_k = \sum_k \sum_{mn} \beta_{jk}^{mn} \chi_{mn} \rho_k. \tag{3.5}$$

Exploiting the linear independence of $\{\rho_k\}$, one obtains the matrix equation

$$\beta\chi = \lambda, \tag{3.6}$$

from which χ-matrix can be extracted by standard methods in linear algebra.

For example, in the case of a single qubit, one can choose the linearly independent basis $\{|0\rangle\langle 0|, |0\rangle\langle 1|, |1\rangle\langle 0|, |1\rangle\langle 1|\}$ (see Fig. 3.1a). While the middle-two elements are non-Hermitian, they can be realized as a linear combination of Hermitian density operators [4]. A fixed set of operators $\{I, X, -iY, Z\}$ can be used to express the χ matrix. Thus the standard single-qubit QPT procedure requires four QST experiments.

QPT on an N-dimensional system requires N^2-QST experiments, where a single QST involves several quantum measurements each taken jointly over a set of commuting observables. The exact number of measurements required for QST may depend on the properties of available detectors.

In NMR, a single-scan experiment allows us to detect all the single-quantum elements of the density matrix (see Fig. 3.1). For example, real and imaginary part of NMR signal of a two qubit system together consists of eight transitions. Transitions in real spectrum corresponding to the four observables are Observables, corresponding to the transitions in

n	M_{QPT}	M_{AAPT}	(n_{A1})	M_{SSPT}	(n_{A1}, n_{A2})
1	8	2	(1)	1	(1, 1)
2	32	4	(2)	1	(2, 2)
3	192	11	(3)	1	(3, 3)
4	1024	32	(4)	1	(4, 5)
5	7168	103	(5)	1	(5, 6)

Table 3.1: Comparison of number of independent measurements and number of ancilla qubits (in parenthesis) required for n-qubit QPT, AAPT, and SSPT.

real part are $\{\sigma_x \otimes |0\rangle\langle 0|, \sigma_x \otimes |1\rangle\langle 1|, |0\rangle\langle 0| \otimes \sigma_x, |1\rangle\langle 1| \otimes \sigma_x\}$ and imaginary part are $\{\sigma_y \otimes |0\rangle\langle 0|, \sigma_y \otimes |1\rangle\langle 1|, |0\rangle\langle 0| \otimes \sigma_y, |1\rangle\langle 1| \otimes \sigma_y\}$. Thus a quadrature detected NMR signal directly provides information on four density matrix elements [34]. To measure other elements, one needs to transform the density matrix by a known unitary, and again record the four transitions. The intensities of these transitions are proportional to linear combinations of various elements of the density matrix. In principle, two experiments suffice for a 2-qubit QST [75]. In the case of an n-qubit NMR system with a well resolved spectrum, QST requires $\simeq \left\lceil \frac{N}{n} \right\rfloor$ measurements, where $\lceil\rfloor$ rounds the argument to next integer [75]. Therefore an n-qubit QPT needs a total of $M_{\mathrm{QPT}} \simeq N^2 \left\lceil \frac{N}{n} \right\rfloor$ measurements. Estimates of M for a small number of qubits shown in the first column of Table 1 illustrate the exponential increase of M_{QPT} with n.

3.2.2 Ancilla-Assisted Process Tomography (AAPT)

If sufficient number of ancillary qubits are available, ancilla assisted process tomography (AAPT) can be carried out by simultaneously encoding all the basis elements onto a higher dimensional system-ancilla Liouville space $A \otimes S$ [58, 59, 73, 74]. AAPT requires a single final QST, thus greatly reducing the number of independent measurements. For example, a single-qubit process tomography can be carried out with the help of an ancillary qubit by preparing the 2−qubit Bell state $|\phi_{AS}\rangle = (|0_A\rangle|0_S\rangle + |1_A\rangle|1_S\rangle)/\sqrt{2}$, applying the process on the system-qubit, and finally carrying out QST of the two-qubit state (see Fig. 3.1b). While the choice of the initial state for AAPT is not unique, the above choice provides a simple way to represent all the four 2×2 dimensional basis states directly onto different

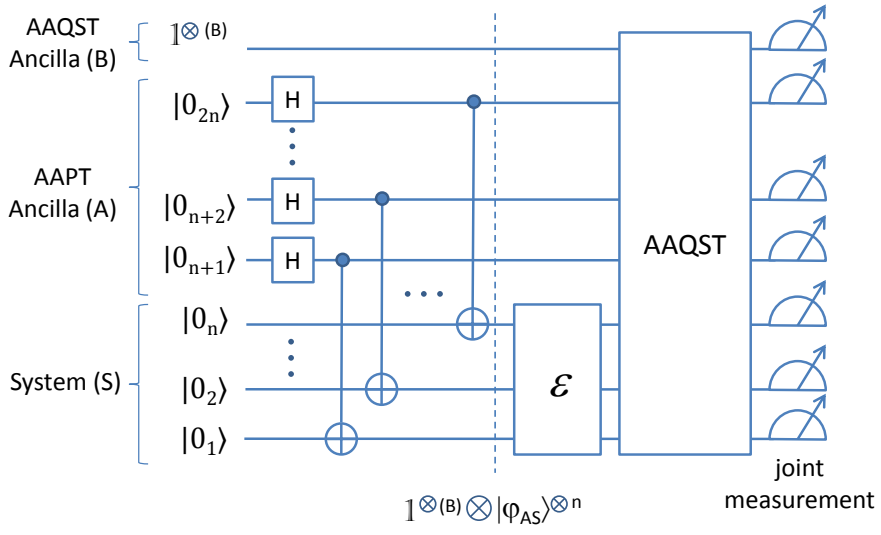

Figure 3.2: Quantum circuit for SSPT. Building blocks of the circuit involves initialization of the system and ancilla registers, encoding of the input states into subspaces of system-ancilla register, application of process ε, and finally AAQST.

subspaces of the 4×4 dimensional density operator (see Figs. 3.1a and 3.1b). For an n-qubit system, all the N^2 basis elements can be encoded simultaneously in independent subspaces of a single $N^2 \times N^2$ Liouville operator belonging to $2n$-qubit space $A \otimes S$. A simple choice for the initial state is of the form $|\phi_{AS}\rangle^{\otimes n}$. The quantum circuit for the preparation of this state is shown in the first part of Fig. 3.2. Thus exactly n-ancilla qubits are needed to carry out AAPT on an n-qubit system.

Although only two independent measurements are needed for a two-qubit QST, this number grows exponentially with the total number of qubits. An n-qubit AAPT involves a $2n$-qubit QST, and accordingly requires $M_{\text{AAPT}} \simeq \left\lceil \frac{N^2}{2n} \right\rceil$ scans [75]. The minimum number of scans for a few system-qubits are shown in the second column of Table 3.1. While AAPT requires significantly lesser number of measurements compared to QPT, it still scales exponentially with the number of system-qubits.

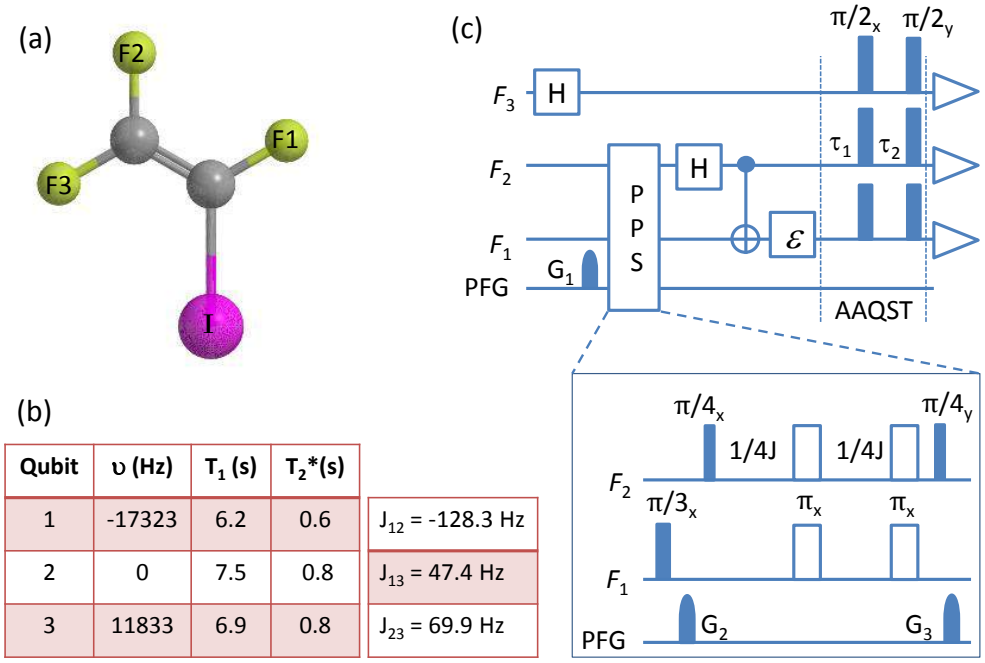

(b)

Qubit	υ (Hz)	T_1 (s)	T_2*(s)
1	-17323	6.2	0.6
2	0	7.5	0.8
3	11833	6.9	0.8

J_{12} = -128.3 Hz
J_{13} = 47.4 Hz
J_{23} = 69.9 Hz

Figure 3.3: Molecular structure of iodotrifluoroethylene (a), and the table of Hamiltonian and relaxation parameters (b), NMR pulse-sequence to demonstrate SSPT (c). Pulse sequence for preparing $|00\rangle$ pseudopure state is shown in the inset of (c).

3.2.3 Single-Scan Process Tomography (SSPT)

It had been shown earlier that, if sufficient number of ancillary qubits are available, QST of a general density matrix of arbitrary dimension can be performed with a single-scan [49, 50, 75]. This method, known as ancilla assisted quantum state tomography (AAQST) is based on the redistribution of all elements of the system density matrix on to a joint density matrix in the combined system-ancilla Liouville space. Initially ancilla register for AAQST is prepared in a maximally mixed state thus erasing all information in it and redistribution of matrix elements is achieved by an optimized joint unitary operator [75]. By combining AAPT with AAQST, process tomography can be achieved with a single-scan measurement of all the qubits (see Fig. 3.1c and 3rd column of Table 3.1).

If AAQST is carried out with an ancilla space (B) of n_B-qubits, the combined space $B \otimes A \otimes S$ corresponds to $\tilde{n} = 2n + n_B$ qubits. A single-scan measurement suffices if the total number of observables is equal to or exceeds the number of real unknowns (i.e.,

N^4-1) in the $2n$-qubit density matrix, i.e., if $\tilde{n}\tilde{N} \geq (N^4-1)$, where $\tilde{N} = 2^{\tilde{n}}$ [75]. However, if only pairwise interactions are used between the system and ancilla of same dimension, then also, a single experiments suffices for AAQST [**?**]. The number of ancillary qubits n_A and n_B required for SSPT are shown in the third column of Table 3.1.

The complete circuit for SSPT is shown in Fig. 3.2. It involves two ancilla registers, one for AAPT and the other for AAQST. Initially AAQST register is prepared in a maximally mixed state and the other two registers are set to $|0\rangle^{\otimes n}$ states. Hadamard gates on the AAPT ancilla followed by C-NOT gates (on system qubits controlled by ancilla) prepare state $|\phi_{AS}\rangle^{\otimes n}$, which simultaneously encodes all the basis elements required for QPT. A single application of the process ε, on the system qubits, acts simultaneously and independently on all the basis elements $\{\rho_j\}$. The final AAQST operation allows estimation of all the elements of the $2n$-qubit density matrix $\sum_j A^{(j)} \otimes \varepsilon(\rho_j)$, where $A^{(j)}$ identifies the jth subspace. The output of each subspace $\varepsilon(\rho_j)$ can now be extracted using a single scan experiment, and the coefficients $\lambda_{jk} = \mathrm{Tr}[\varepsilon(\rho_j)\rho_k^\dagger]$ can be calculated.

3.3 Experiments

We used iodotrifluoroethylene (C_2F_3I) dissolved in acetone-D_6 as a 3-qubit system. The molecular structure and labelling scheme are shown in Fig. 3.3a. All the experiments described below are carried out on a Bruker 500 MHz NMR spectrometer at an ambient temperature of 300 K using high-resolution NMR techniques. The NMR Hamiltonian in this case can be expressed as

$$\mathcal{H} = -\pi \sum_{i=1}^{3} \nu_i \sigma_z^i + \pi \sum_{i=1,j>i}^{3,3} J_{ij}\sigma_z^i\sigma_z^j/2 \tag{3.7}$$

where σ_z^i and σ_z^j are Pauli z-operators of ith and jth qubits [34]. The chemical shifts ν_i, coupling constants J_{ij}, and relaxation parameters (T_1 and T_2^*) are shown in Fig. 3.3b. All the pulses are realized using gradient ascent pulse engineering (GRAPE) technique [43] and had average fidelities above 0.99 over 20% inhomogeneous RF fields.

We utilize spins F_1, F_2, and F_3 respectively as the system qubit (S), AAPT ancilla (A),

and AAQST ancilla (B). The NMR pulse-sequence for SSPT experiments are shown in Fig. 3.3c. It begins with preparing B qubit in the maximally mixed state by bringing its magnetization into transverse direction using a Hadamard gate, and subsequently dephasing it using a PFG. The remaining qubits are initialized into a pseudopure $|00\rangle$ state by applying the standard pulse-sequence shown in the inset of Fig. 3.3c [38]. The Bell state $|\phi_{AS}\rangle$ prepared using a Hadamard-CNOT combination had a fidelity of over 0.99. After preparing this state, we applied the process ε on the system qubit. The final AAQST consists of $(\pi/2)_x$ and $(\pi/2)_y$ pulses on all the qubits separated by delays $\tau_1 = 6.7783$ ms and $\tau_2 = 8.0182$ ms [75]. A single-scan measurement of all the qubits now leads to a complex signal of 12 transitions, from which all the 15 real unknowns of the 2-qubit density matrix $\rho_{AS} = \sum_j A^{(j)} \otimes \varepsilon(\rho_j)$ of F_1 and F_2 can be estimated [75] (see Fig. 3.1). In our choice of fixed set of operators and basis elements

$$\rho_{AS} = \left[\begin{array}{cc|cc} \lambda_{11} & \lambda_{12} & \lambda_{21} & \lambda_{22} \\ \lambda_{13} & \lambda_{14} & \lambda_{23} & \lambda_{24} \\ \hline \lambda_{31} & \lambda_{32} & \lambda_{41} & \lambda_{42} \\ \lambda_{33} & \lambda_{34} & \lambda_{43} & \lambda_{44} \end{array}\right]. \tag{3.8}$$

The χ matrix characterizing the complete process can now be obtained by solving the eqn. 6.10.

3.3.1 SSPT of quantum gates

We now describe experimental characterization of several single-qubit unitary processes. The quantum gates to be characterized are introduced as process ε on F_1 qubit in Fig. 3.3c. The experimental χ-matrices for NOP (identity process), NOT-X ($e^{-i\pi X/2}$), NOT-Y ($e^{-i\pi Y/2}$), Hadamard, Phase$-\pi$ ($e^{i\pi Z/2}$), and Phase$-\pi/4$ ($e^{i\pi Z/8}$) are shown in Fig. 3.4. Starting from thermal equilibrium, each SSPT experiment characterizing an entire one-qubit process took less than four seconds. A measure of overlap of the experimental

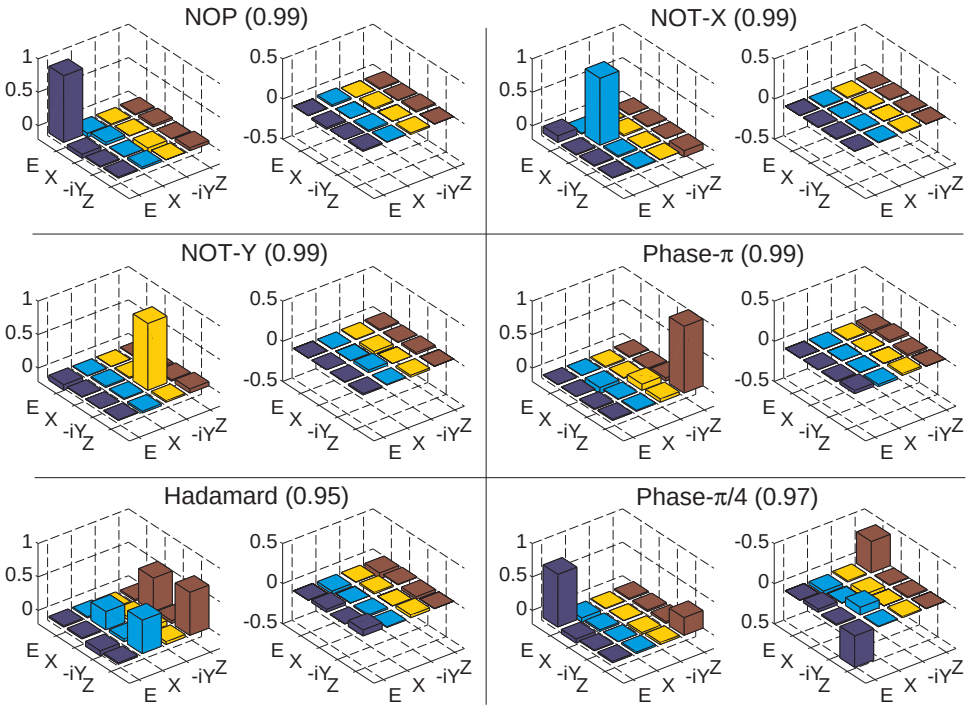

Figure 3.4: The barplots showing experimental χ-matrices for various quantum processes obtained using SSPT. In each case, the left and right barplots correspond to the real and imaginary parts respectively, and the fidelities are indicated in parenthesis.

process $\chi_{\rm exp}$ with the theoretically expected process $\chi_{\rm th}$ is given by the gate fidelity [70]

$$F(\chi_{\rm exp},\chi_{\rm th}) = \frac{|Tr[\chi_{\rm exp}\chi_{\rm th}^{\dagger}]|}{\sqrt{Tr[\chi_{\rm exp}^{\dagger}\chi_{\rm exp}]\;Tr[\chi_{\rm th}^{\dagger}\chi_{\rm th}]}}. \tag{3.9}$$

The gate fidelities for all the six processes are indicated in Fig. 3.4. Except in the cases of Hadamard and Phase-$\pi/4$, the gate fidelities were about 0.99. The lower fidelities in Hadamard (0.95) and Phase-$\pi/4$ (0.97) are presumed to be due to RF inhomogeneity and nonlinearities in the pulse implementations.

In order to study the robustness of SSPT procedure we first considered an ideal process, simulated the corresponding spectral intensities, and reconstructed the final density matrix ρ_{AS}. Using eqn. 3.8 we obtained λ_{jk} values and calculated the matrix χ_0 simulating the noise-free SSPT procedure. We then introduced noise by adding random numbers in the range $[-\eta,\eta]$ to the spectral intensities and used the resulting data for calculating χ_η. The variations of average gate fidelities $F(\chi_0,\chi_\eta)$ for various processes versus noise am-

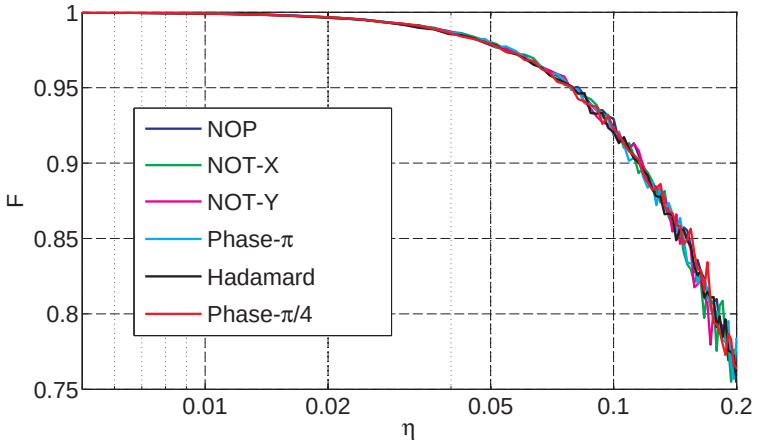

Figure 3.5: Simulated fidelity of various processes as a function of noise strength η.

plitude η are shown in Fig. 3.5. Interestingly, the noise has similar effects on fidelities of all the simulated processes. We also observe that fidelities remained above 0.9 for $\eta < 0.1$, indicating that SSPT is fairly robust against the noise in this range.

3.3.2 SSPT of twirling process

Twirling is essentially a nonunitary process usually realized by an ensemble average of a set of unitary operations. It was first introduced by Bennett et al [76] for extracting singlet states from a mixture of Bell states. Twirling has been studied in detail [77–81] and various modified twirling protocols have also been suggested [82, 83].

In NMR, twirling can be achieved with the help of a pulsed field gradient (PFG), which produces a continuous space-dependent spin-rotation, such that the ensemble average effectively emulates a nonunitary process [84]. A $\hat{z}$ PFG produces a z-dependent unitary $U_\phi(z) = \exp\left(-i\frac{\phi}{2}\sum_{j=1}^{n}\sigma_{jz}\right)$, where j is the summation index over all the qubits. Assuming a linear gradient introducing a maximum phase $\pm\Phi$ on either ends of a sample of length z_0, we have $\phi(z) = 2\Phi(z/z_0)$. When the $\hat{z}$ PFG acts on an initial n-qubit density matrix $\rho_{\text{in}} = \sum_{lm}\rho_{lm}|l\rangle\langle m|$, the resultant output density matrix is,

$$\begin{aligned}\rho_{\text{out}} &= \frac{1}{2\Phi}\int_{-\Phi}^{\Phi} d\phi\ U_\phi \rho_{\text{in}} U_\phi^\dagger \\ &= \sum_{lm} \rho_{lm}|l\rangle\langle m|\ \text{sinc}(q_{lm}\Phi). \end{aligned} \tag{3.10}$$

Here $\text{sinc(x)} = \frac{\sin x}{x}$ and $q_{lm} = \frac{1}{2}\sum_j [(-1)^{m_j} - (-1)^{n_j}]$ is the quantum number of the element $|l_1 l_2 \cdots l_n\rangle\langle m_1 m_2 \cdots m_n|$, i.e., the difference in the spin-quantum numbers of the corresponding basis states. While the diagonal elements $|l\rangle\langle l|$ and other zero-quantum elements are unaffected by twirling, the off-diagonal elements with $q_{lm} \neq 0$ undergo decaying oscillations with increasing Φ values.

SSPT of twirling process is carried out using the procedure described in Fig. 3.3c after introducing δ-PFG-δ in place of the process ε, where δ is a short delay for switching the gradient. Applying PFG selectively on the system qubit is not simple, and is also unnecessary. Since the F_3 qubit (AAQST ancilla) is already in a maximally mixed state, twirling has no effect on it. For the Bell state $|\phi_{AS}\rangle$, applying a strong twirling on either or both spins (F_1, F_2) has the same effect, i.e., a strong measurement reducing the joint-state to a maximally mixed state. However, since $|\phi_{AS}\rangle$ corresponds to a two-quantum coherence (i.e., $q_{00,11} = 2$), its dephasing is double that of a single-quantum coherence. Assuming the initial state $\rho_{\text{in}} = |\phi_{AS}\rangle\langle\phi_{AS}|$, and using expressions 3.1 and 3.10, we find that the non-zero elements of λ are

$$\lambda_{11} = \lambda_{44} = 1, \text{ and, } \lambda_{22} = \lambda_{33} = \text{sinc}(2\Phi). \tag{3.11}$$

Solving expression 6.10, we obtain a real χ matrix with only nonzero elements

$$\chi_{\text{EE}} = \frac{1 + \text{sinc}(2\Phi)}{2} \text{ and } \chi_{\text{ZZ}} = \frac{1 - \text{sinc}(2\Phi)}{2}. \tag{3.12}$$

In our experiments, the duration of PFG and δ are set to 300 µs and 52.05 µs respectively, such that the chemical shift evolutions and J-evolutions are negligible. The strength of twirling is slowly varied by increasing the PFG strength from 0 to 2.4 G/cm in steps of 0.05 G/cm. The results of the experiments are shown in Fig. 3.6. The filled squares

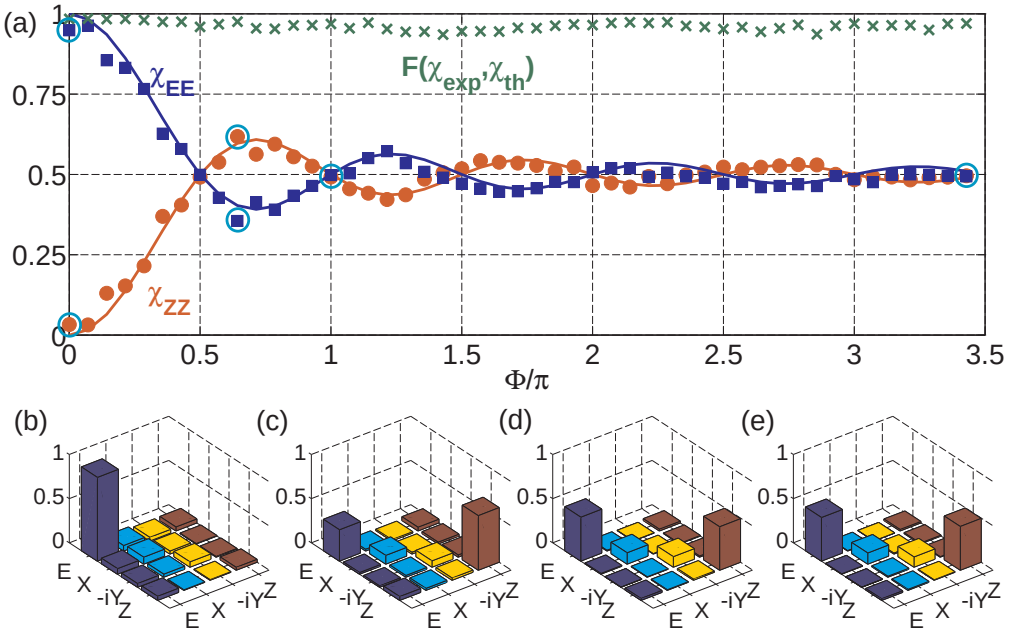

Figure 3.6: (a) The experimental values of $|\chi_{EE}|$ ($|\chi_{ZZ}|$) are shown by filled squares (filled circles). The solid line (χ_{EE}) in blue and (χ_{ZZ}) in red illustrate theory. The barplots correspond to experimental $|\chi|$ matrices at (b) $\Phi = 0$, (c) $\Phi = 0.64\pi$, (d) $\Phi = \pi$, and (e) $\Phi = 3.43\pi$.

(circles) in Fig. 3.6a correspond to experimentally obtained values for $|\chi_{EE}|$ ($|\chi_{ZZ}|$). Small imaginary parts observed in experimental χ matrices are due to minor experimental imperfections. The smooth lines indicate corresponding theoretical values obtained from eqns. 3.12. The crosses indicate the gate fidelities $F(\chi_{\rm exp},\chi_{\rm th})$ calculated using eqn. 3.9. The barplots show experimental $|\chi|$ matrices for (b) $\Phi = 0$, (c) $\Phi = 0.64\pi$, (d) $\Phi = \pi$, and (e) $\Phi = 3.43\pi$, and χ_{EE} and χ_{ZZ} values in Fig. 3.6a corresponding to these Φ values are circled out.

At zero twirling, the process is essentially a NOP process as is clear from the bar plot in Fig. 3.6b, wherein $|\chi_{EE}| \approx 1$ and $|\chi_{ZZ}| \approx 0$. When $\Phi = k\pi/2$ with an integer k, the ensemble initially prepared in state $|\psi_{AS}\rangle$ undergoes an overall phase distribution over $[-k\pi, k\pi]$, and at this stage $\chi_{EE} = \chi_{ZZ} = 0.5$ (eg. Fig. 3.6d). Further increase in Φ leads to oscillations of χ_{EE} and χ_{ZZ} about 0.5, and for large Φ values, both of these elements damp towards 0.5 and all other elements vanish (eg. Fig. 3.6e). The errors in experimental χ_{EE} and χ_{ZZ} values were less than 8 %. The good agreement of the experimental values with theory indicates the overall success of SSPT procedure. The average of the gate

fidelities was over 0.96. Small deviations of the experimental values from theory are due to nonlinearities in PFG profile as well as due to imperfections in RF pulses implementing the SSPT procedure.

3.4 Conclusions

Information processing requires two important physical resources, namely, the size of the register and the number of operations. Often there exists an equivalence between these two resources which allows trading one resource with another. Likewise, in the present work we show that, if some extra qubits are available, it is possible to carry out quantum process tomography of the system qubits with a single-scan ensemble measurement. We have illustrated this method on a single system qubit and two ancillary qubits using NMR quantum computing methods. In particular, we extracted the χ matrices characterizing certain quantum gates and obtained their gate fidelities with the help of a single ensemble measurement of a three qubit system in each case. We studied the robustness of SSPT procedure using numerical simulations. We also characterized twirling operation which is essentially a nonunitary process.

The ensemble nature of NMR systems allows us to determine all the single-quantum observables in a single scan experiment. However, a larger ancilla may be required if measurement of only a commuting set of observables is allowed in a single experiment, as in the case of single-apparatus QST [48], or if the system-ancilla interactions are constrained, as in pair-wise interaction case [85]. Nevertheless, the overall procedure of SSPT can be generalized to apply in other fields such as optical qubits, trapped ions, or superconducting qubits.

A potential application of single-scan process tomography could be in high throughput characterization of dynamic processes. The standard methods require repeated applications of the same process either to collect independent outputs from all the basis states or to allow quantum state tomography. However, the present method requires only one application of the process for the entire characterization.

Chapter 4

Ancilla assisted non-invasive measurements

The measurement of a classical object need not affect its subsequent dynamics. Thus classical measurements are said to be *non-invasive*. On the other hand, a strong measurement of a quantum object does affect its subsequent dynamics, and is said to be *invasive*. The effects of measurements on dynamics of the classical and the quantum objects are illustrated below in Fig. 4.1.

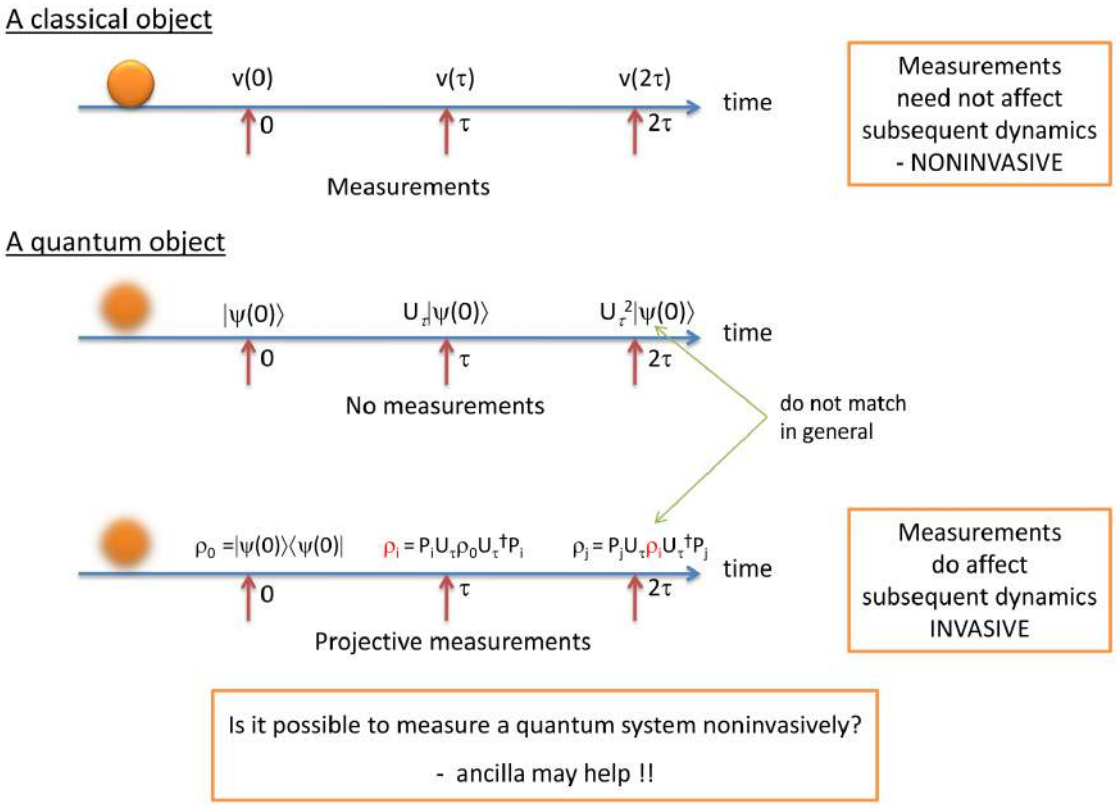

Figure 4.1: Illustrating classical *noninvasive* measurements and quantum *invasive* measurements.

Certain quantum mechanical studies, like Leggett-Garg inequality, are based on the assumption of non-invasive measurability [27, 86–89]. Recently Knee et al [90] have

proposed a scheme known as *ideal negative result measurement* (INRM), which is more effectively non-invasive than some previous schemes. Here we describe two interesting quantum physics problems studied using NMR systems, wherein ancilla qubits are utilized for noninvasive measurements. The problems of interest are:

1. Entropic Leggett-Garg Inequality (ELGI) in nuclear spin ensembles and,

2. Retrieving joint probabilities by inversion of moments in quantum sequential measurements.

Some definitions:

Joint and Conditional probabilities: In probability theory, given at least two random variables X and Y with outcomes $\{x_i\}$ and $\{y_j\}$, the joint probability distribution $p(X, Y)$ gives the probability of combined outcomes x_i and y_j for variable X and Y. Although here I have described it for a two variable case, the concept is general and can be extended to any number of random variables and also for continuous variables.

The Conditional probability distribution $p(Y/X)$ for random variables X and Y gives the probability of getting outcome y_j for given outcome x_i. Given a joint probability distribution $p(X, Y)$ the conditional probability distribution can be calculated as $p(Y/X) = p(X, Y)/p(x)$. This relation is also known as Bayes theorem.

Marginal and grand probabilities: Consider a set of random variable $\{X_i\}$ for $i = 1 \cdots n$ and outcome $\{x_i = \pm 1\}$. According to the classical probability theory, if the n variable joint probability is $p(x_1, x_2, \cdots x_n)$, then the family of $n - 1$ variate probability $p(x_1, x_2, \cdots x_{k-1}, x_{k+1} \cdots x_{n-1})$ can be obtained by summing up (marginalizing out) probabilities corresponding to all outcomes variable x_k. These probabilities are known as marginals of $p(x_1, x_2, \cdots x_n)$. By marginalizing different combinations of variables, a complete family of marginal probabilities can be obtained.

4.1 Entropic Leggett-Garg Inequality in Nuclear Spin Ensembles

4.1.1 Introduction

The behavior of quantum systems is often incomprehensible by classical notions, the best examples being nonlocality [91,92] and contextuality [93]. Quantum systems are *nonlocal* since they violate Bell's inequality, which assumes that local operations on one of the two space-like separated objects can not disturb the measurement outcomes of the other [94]. The quantum systems are also *contextual* in the sense that a measurement outcome depends not only on the system and the property being measured, but also on the context of the measurement, i.e., on the set of other compatible properties which are being measured along with.

Another notion imposed on classical objects is macrorealism, which is based on two criteria: (i) the object remains in one or the other of many possible states at all times, and (ii) the measurements are noninvasive, i.e., they reveal the state of the object without disturbing the object or its future dynamics. Quantum systems are incompatible with these criteria and therefore violate bounds on correlations derived from them. For instance, Leggett-Garg inequality (LGI) sets up macrorealistic bounds on linear combinations of two-time correlations of a dichotomic observable belonging to a single dynamical system [95]. In this sense, LGI is considered as a temporal analogue of Bell's inequality. Quantum systems do not comply with LGI, and therefore provide an important way to distinguish the quantum behavior from macrorealism. Violations of LGI by quantum systems have been investigated and demonstrated experimentally in various systems [86–90, 96–101].

For understanding the quantum behavior it is important to investigate it through different approaches, particularly from an information theoretical point of view. For example, an entropic formulation for Bell's inequality has been given by Braunstein and Caves [102], and more recently that for contextuality has been given independently by Rafael and Fritz [103] and Kurzynski *et.al.* [104]. Recently, an entropic formulation of LGI has also been introduced by Usha Devi *et al.* [1], in terms of classical Shannon entropies associated with classical correlations.

Here we report an experimental demonstration of violation of entropic LGI (ELGI) in an ensemble of spin 1/2 nuclei using nuclear magnetic resonance (NMR) techniques. Although NMR experiments are carried out at a high temperature limit, the nuclear spins have long coherence times, and their unitary evolutions can be controlled in a precise way. The large parallel computations carried out in an NMR spin ensemble assists in efficiently extracting the single-event probability (SEP) and joint probabilities (JP). The simplest ELGI study involves three sets of two-time joint measurements of a dynamic observable belonging to a 'system' qubit at time instants (t_1, t_2), (t_2, t_3), and (t_1, t_3). The first measurement in each case must be 'noninvasive' in the sense, it should not influence the outcome of the second measurement. These noninvasive measurements (NIM) can be performed with the help of an ancilla qubit.

Further, it has been argued in [1] that the violation of ELGI arises essentially due to the fact that certain JP are not legitimate in a quantum scenario. Here we describe extracting three-time JP using a three-qubit system, and demonstrate experimentally that it can not reproduce all the marginal probabilities (MP) and hence is illegitimate.

This section is organized as follows. In subec. 4.1.2 I briefly revisit the theory of the ELGI [1], and then I describe the scheme we designed for the measurement of probabilities in subec. 4.1.3. Later I detail our experimental study in subsec. 4.1.4 and describe the study of the three-time joint probability in subec. 4.1.5. I conclude in subec. 4.1.6.

4.1.2 Theory

Consider a dynamical observable $Q(t_k) = Q_k$ measured at different time instances t_k. Let the measurement outcomes be q_k with probabilities $P(q_k)$. In classical information theory, the amount of information stored in the random variable Q_k is given by the Shannon entropy [4],

$$H(Q_k) = -\sum_{q_k} P(q_k) \log_2 P(q_k). \tag{4.1}$$

The conditional information stored in Q_{k+l} at time t_{k+l}, assuming that the observable Q_k has an outcome q_k, is

$$H(Q_{k+l}|Q_k = q_k) = -\sum_{q_{k+l}} P(q_{k+l}|q_k) \log_2 P(q_{k+l}|q_k),$$

where $P(q_{k+l}|q_k)$ is the conditional probability. Then the mean conditional entropy is given by,

$$H(Q_{k+l}|Q_k) = -\sum_{q_k} P(q_k) H(Q_{k+l}|Q_k = q_k). \tag{4.2}$$

Using Bayes' theorem, $P(q_{k+l}|q_k)P(q_k) = P(q_{k+l}, q_k)$, Here $P(q_k) = P(q_{k+l}, q_k)$ the mean conditional entropy becomes

$$H(Q_{k+l}|Q_k) = H(Q_k, Q_{k+l}) - H(Q_k), \tag{4.3}$$

where the joint Shannon entropy is given by

$$H(Q_k, Q_{k+l}) = -\sum_{q_k, q_{k+l}} P(q_{k+l}, q_k) \log_2 P(q_{k+l}, q_k). \tag{4.4}$$

These Shannon entropies always follow the inequality [102]

$$H(Q_{k+l}|Q_k) \leq H(Q_{k+l}) \leq H(Q_k, Q_{k+l}). \tag{4.5}$$

The left side of the equation implies that removing a constraint never decreases the entropy, and the right side implies information stored in two variables is always greater than or equal to that in one [1]. Suppose that three measurements Q_k, Q_{k+l}, and Q_{k+m}, are performed at time instants $t_k < t_{k+l} < t_{k+m}$. Then, from equations (4.3) and (4.5), the following inequality can be obtained:

$$H(Q_{k+m}|Q_k) \leq H(Q_{k+m}|Q_{k+l}) + H(Q_{k+l}|Q_k). \tag{4.6}$$

For n measurements $Q_1, Q_2, \ldots, Q_n$, at time instants $t_1 < t_2 < \cdots < t_n$, the above inequality can be generalized to [1]

$$\sum_{k=2}^{n} H(Q_k|Q_{k-1}) - H(Q_n|Q_1) \geq 0. \tag{4.7}$$

This inequality must be followed by all macro-realistic objects, since its satisfaction means the existence of legitimate JP distribution, which can yield all MP [105].

Usha Devi *et al.* [1] have shown theoretically that the above inequality is violated by a quantum spin-s system, prepared in a completely mixed initial state, $\rho_{in} = \mathbb{I}/(2s+1)$. Consider the z-component of the spin evolving under the Hamiltonian $H = -\omega S_x$ as our dynamical observable, *i.e.* $Q_t = U_t S_z U_t^\dagger$, where $U_t = e^{-iHt}$, and S_x and S_z are the components of spin-angular momentum. Let n-measurements occur at regular time instants $\Delta t,\ 2\Delta t, \cdots, n\Delta t$. Ideally in this case, the conditional entropies $H(Q_k|Q_{k-1})$ between successive measurements are all equal, and can be denoted as $H[\theta/(n-1)]$, where $\theta/(n-1) = \omega\Delta t$ is the rotation caused by the Hamiltonian in the interval Δt. Similarly we can denote $H(Q_n|Q_1)$ as $H[\theta]$. The left hand side of inequality (4.7) scaled in units of $\log_2(2s+1)$ is termed as the information deficit D. For n-equidistant measurements, it can be written as [1]

$$D_n(\theta) = \frac{(n-1)H[\theta/(n-1)] - H[\theta]}{\log_2(2s+1)} \geq 0. \tag{4.8}$$

4.1.3 Measurement of Probabilities

Consider a spin-1/2 particle as the system qubit. Using the eigenvectors $\{|0\rangle, |1\rangle\}$ of S_z, as the computational basis, the projection operators at time $t = 0$ are $\{\Pi_\alpha = |\alpha\rangle\langle\alpha|\}_{\alpha=0,1}$. For the dynamical observable, the measurement basis is rotating under the unitary $U_t = e^{i\omega S_x t}$, such that $\Pi_\alpha^t = U_t \Pi_\alpha U_t^\dagger$. However, it is convenient to perform the actual measurements in the time-independent computational basis. Since for an instantaneous state $\rho(t)$, $\Pi_\alpha^t \rho(t) \Pi_\alpha^t = U_t \Pi_\alpha \left(U_t^\dagger \rho(t) U_t\right) \Pi_\alpha U_t^\dagger$, measuring in $\{\Pi_\alpha^t\}$ basis is equivalent to back-evolving the state by $U_t^\dagger$, measuring in computational basis, and lastly forward evolving by U_t. This latter evolution can be omitted if one is interested only in the probabilities and not in the post measurement state of the system. For example, in case of multiple-time

measurements, the forward evolution can be omitted after the final measurement. The method for extracting SEP and JP involves the quantum circuits shown in Fig. 4.2. To measure SEP $P(q_i)$ of system qubit in a general state ρ_S, it is evolved by $U_i^\dagger = e^{iHt_i}$, and the probabilities $P(q_i)$ are obtained using diagonal tomography. Here a further forward evolution by U_i is not necessary as described earlier.

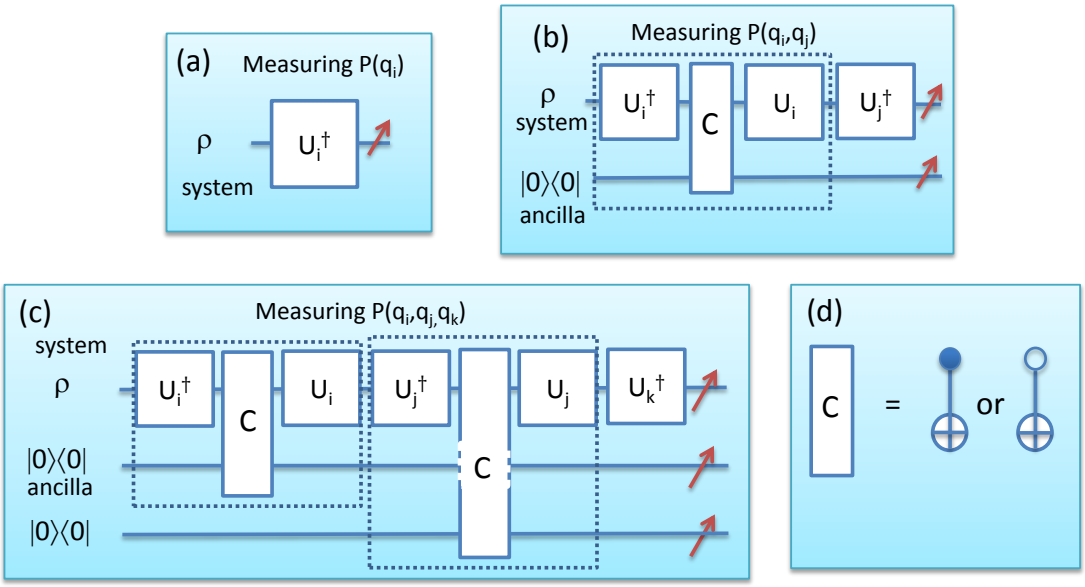

Figure 4.2: Circuits for measuring SEP (a), and two-time JP (b), and three-time JP (c). The grouped gates represent measurement in $\{\Pi_0^t, \Pi_1^t\}$ basis. The operation C can be either CNOT gate or anti-CNOT gate, as described in the text. In (c) the second CNOT gate is applied between first and third spin. The pointer at the end in each circuit represents the measurement of diagonal elements of the density matrix. (d) Block C represents either CNOT or anti-CNOT gate.

To measure JP $P(q_i, q_j)$, we utilize an ancilla qubit initialized in the state $|0\rangle\langle 0|$ (Fig. 4.2 b). After back evolution to computational basis, the CNOT gate encodes the probabilities of the system-qubit $P(q_i)$ on to the ancilla-qubit. After a further evolution by $U_i U_j^\dagger = e^{-i\omega S_x(t_j - t_i)}$, a diagonal tomography of the two qubit system yields $P(q_i, q_j)$. A similar scheme, shown in Fig. 4.2 c, is employed for extracting three-time JP. These circuits can be generalized for higher order JP or for spin-$s > 1/2$ systems, using appropriate ancilla register.

In the earlier LGI experiments, NIM have been performed by either (i) a weak measurement which has minimum effect on the post measurement quantum state [86–88] or (ii) initializing the system qubit in the maximally mixed state so that the system density matrix remains unchanged by the measurements [89, 97]. Recently however, it was noted by Knee *et al.* that a sceptical macrorealist is not convinced by either of the above methods [90]. Instead, they had proposed convincingly, a more non-invasive procedure, known as ideal negative result' measurements (INRM) [90]. The idea for INRM is as follows. The CNOT gate is able to flip the ancilla qubit only if the system qubit is in state $|1\rangle$, and does nothing if the system qubit is in state $|0\rangle$. Therefore after the CNOT gate, if we measure the probability of unflipped ancilla, this corresponds to an 'interaction-free' or NIM of $P(q = 0)$. Similarly, we can implement an anti-CNOT gate, which flips the ancilla only if the system qubit is in state $|0\rangle$, and does nothing otherwise, such that the probability of unflipped qubit now gives $P(q = 1)$. Note that in both the cases, the probabilities wherein the system interacted with the ancilla, resulting in its flip, are discarded Fig. 4.3. To see this property consider a one qubit general state (for system) and an ancilla in the state $|0\rangle\langle 0|$, then the encoding of probability using C-NOT is as follows

$$\begin{gathered}\left(p_0|0\rangle\langle 0| + p_1|1\rangle\langle 1| + a|1\rangle\langle 0| + a^\dagger|0\rangle\langle 1|\right)_S \otimes |0\rangle\langle 0|_A \\ \downarrow \text{CNOT} \\ |0\rangle\langle 0|_S \otimes p_0|0\rangle\langle 0|_A + |1\rangle\langle 1|_S \otimes p_1|1\rangle\langle 1|_A \\ +|1\rangle\langle 0|_S \otimes a|1\rangle\langle 0|_A + |0\rangle\langle 1|_S \otimes a^\dagger|0\rangle\langle 1|_A.\end{gathered}$$

Now measuring the diagonal terms of the ancilla qubit, we can retrieve p_0 and p_1.

Since we are not concerned about any further evolution, the last measurement need not be NIM. In our experiments we combine the two methods, i.e., (i) first we prepare the system in a maximally mixed state i.e., $\rho_S = \mathbb{I}/2$, and (ii) we perform INRM. In this case, $P(0_i) = P(1_i) = 1/2$, and JP are

$$\begin{aligned}P(0_i, 0_j) &= |\cos(\theta_{ij}/2)|^2/2 = P(1_i, 1_j), \quad \text{and,} \\ P(0_i, 1_j) &= |\sin(\theta_{ij}/2)|^2/2 = P(1_i, 0_j),\end{aligned} \tag{4.9}$$

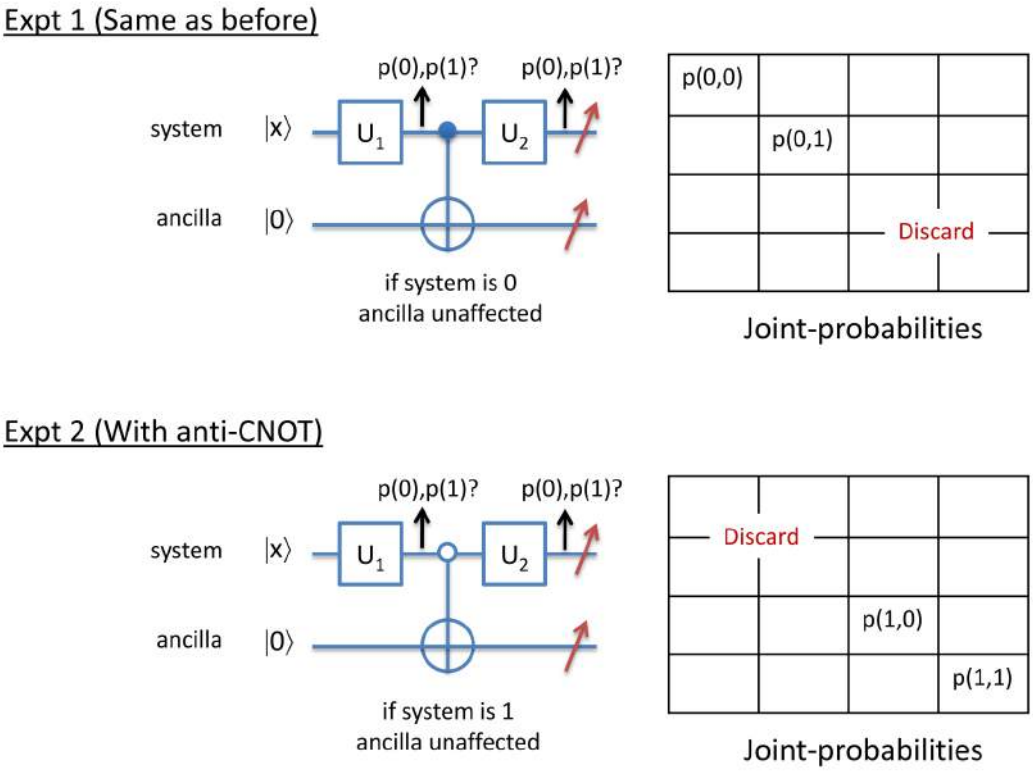

Figure 4.3: INRM procedure for extracting probabilities P_0 (a) and P_1 (b) of a single qubit system.

where $\theta_{ij} = \omega(t_j - t_i)$ [1]. The only SEP needed for the ELGI test is $H(Q_1)$, since $H(Q_t)$ is constant for the maximally mixed system state. Further, since $H(Q_1, Q_2) = H(Q_2, Q_3)$ in the case of uniform time intervals, only two joint entropies $H(Q_1, Q_2)$ and $H(Q_1, Q_3)$ are needed to be measured for evaluating D_3. In the following we describe the experimental implementation of these circuits for the three-measurement LGI test.

4.1.4 Experiment

We have used $^{13}CHCl_3$ (dissolved in $CDCl_3$) as the two qubit system and treat its ^{13}C and ^{1}H nuclear spins as the system and the ancilla qubits respectively as shown in Fig. 4.4 a. The resonance offset of ^{13}C was set to 100 Hz and that of ^{1}H to 0 Hz (on resonant) Fig. 4.4 b. The two spins have an indirect spin-spin coupling constant $J = 209.2$ Hz. All the

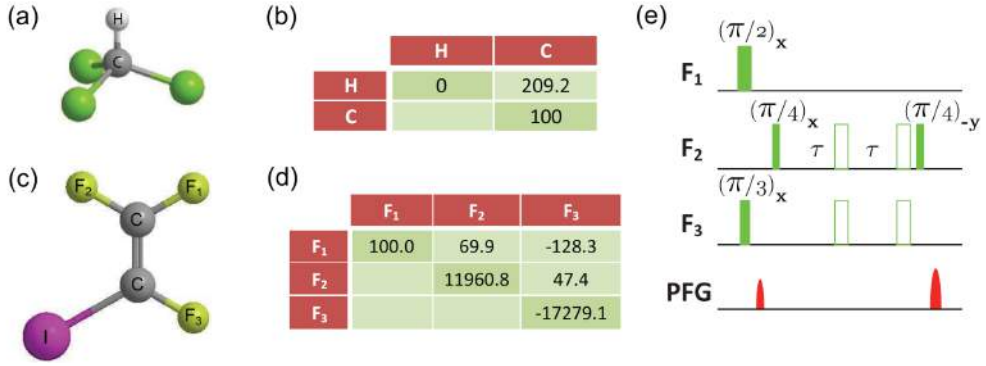

Figure 4.4: The molecular structures of chloroform (a) and trifluoroiodoethylene (c) and the corresponding tables (b and d) of relative resonance frequencies (diagonal elements) and the J-coupling constants. The pulse sequence for initializing trifluoroiodoethylene is shown in (e). In (e) the open pulses are π pulses and the delay $\tau = 1/(4J_{23})$.

experiments were carried out at an ambient temperature of 300 K on a 500 MHz Bruker UltraShield NMR spectrometer.

The initialization involved preparing the maximally mixed state $\rho_S = \mathbb{I}/2$ on the system qubit ^{13}C. This is achieved by a $\pi/2$ pulse on ^{13}C followed by a strong pulsed field gradient (PFG). The evolution propagator $U_j^\dagger U_i = e^{-iS_x\omega(t_j-t_i)}$ is realized by the cascade HU_dH, where H is the Hadamard gate, and the delay propagator $U_d = e^{-iS_z\omega(t_j-t_i)}$ corresponds to the $\hat{z}$-precession of the system qubit at $\omega = 200\pi$ rad/s resonance off-set. The J-evolution during this delay is refocused by a π pulse on the ancilla qubit. The CNOT, H, as well as the π pulses are realized by numerically optimized amplitude and phase modulated RF pulses, and are robust against the RF inhomogeneity with a average Hilbert-Schmidt fidelity better than 0.998 [42, 43, 106]. The final measurement of probabilities are carried out by diagonal tomography. It involved dephasing all the coherences using a strong pulsed field gradient followed by a $\pi/30$ detection pulse. The intensities of the resulting spectral lines yielded a traceless diagonal density matrix d_{ii}, which was normalized by theoretical deviation density matrix and a trace is introduced by adding the identity matrix to the normalized deviation matrix such that they both have the same root mean square value $\sqrt{\sum_i d_{ii}^2}$. As described in Fig. 4.2b, two sets of experiments were performed, one with CNOT and the other with anti-CNOT. We extracted $P(0,q)$ ($q = \{0,1\}$) from the

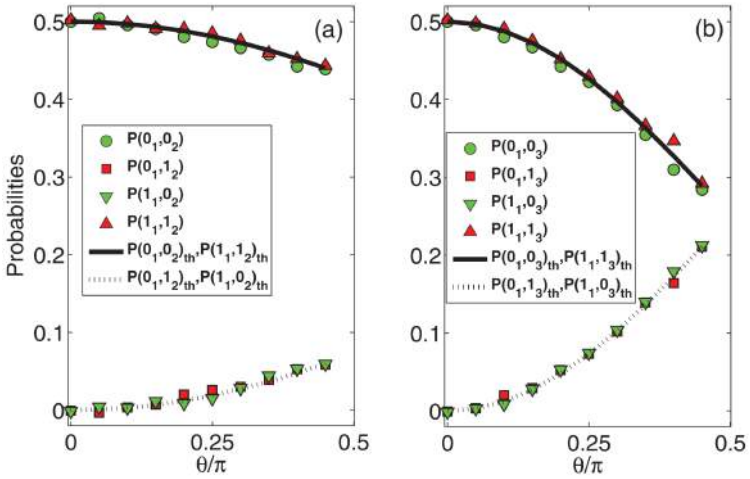

Figure 4.5: The lines indicate the theoretical joint probabilities (a) $P(q_1, q_2)_{th}$ and (b) $P(q_1, q_3)_{th}$, and the symbols indicate the mean experimental probabilities (a) $P(q_1, q_2)$ and (b) $P(q_1, q_3)$ obtained by the INRM procedure.

CNOT set, and $P(1, q)$ from the anti-CNOT set. The probabilities thus obtained by INRM procedure are plotted in Fig. 4.5. These sets of experiments also allow us to compare the results from (i) only CNOT, (ii) only anti-CNOT, and (iii) INRM procedures. The joint entropies were calculated in each case using the experimental probabilities and the information deficit (in bits) was calculated using the expression $D_3 = 2H(Q_2|Q_1) - H(Q_3|Q_1)$. The theoretical and experimental values of D_3 for various rotation angles θ are shown in Fig. 4.6. We find a general agreement between the mean experimental D_3 values with that of the quantum theory. The error bars indicate the standard deviations obtained by a series of independent measurements. According to quantum theory, a maximum violation of $D_3 = -0.134$ should occur at $\theta = \pi/4$. The experimental values of $D_3(\pi/4)$ are -0.141 ± 0.005, -0.136 ± 0.002, and -0.114 ± 0.027 for the CNOT, anti-CNOT, and INRM cases respectively. Thus in all the cases, we found a clear violation of ELGI.

4.1.5 Three-time Joint Probabilities

In the above, we have described extracting the two-time JP $P(q_i, q_j)$ directly. However, it should also be possible to generate them as marginals $P'(q_i, q_j)$ of three-time joint proba-

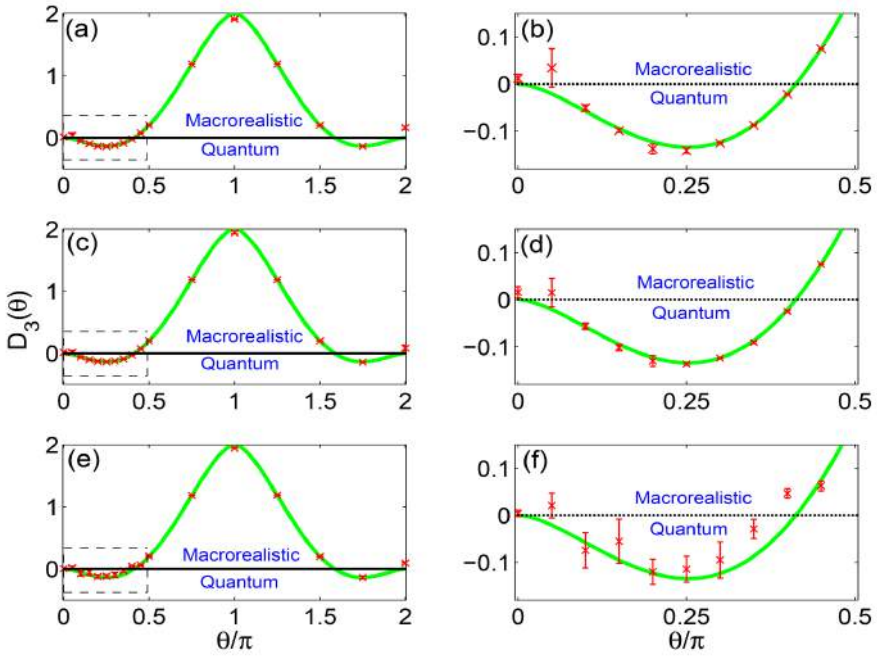

Figure 4.6: Information deficit D_3 versus θ obtained using (a), (b) CNOT; (c), (d) anti-CNOT; and (e), (f) INRM procedure. The boxed areas in the left plots [(a), (c), (e)] are magnified in the right plots [(b), (d), (f)], respectively. The mean experimental D3 (in bits) values are shown as symbols. The curves indicate theoretical D3 (in bits). The horizontal lines at D3 = 0 indicate the lower bounds of the macrorealism territories.

bilities:

$$\begin{aligned} P'(q_1,q_2) &= \sum_{q_3} P(q_1,q_2,q_3), \\ P'(q_2,q_3) &= \sum_{q_1} P(q_1,q_2,q_3), \text{ and} \\ P'(q_1,q_3) &= \sum_{q_2} P(q_1,q_2,q_3). \end{aligned} \tag{4.10}$$

Now $P(q_1,q_2,q_3)$ can reproduce $P(q_1,q_2)$ and $P(q_2,q_3)$, i.e., $P'(q_1,q_2) = P(q_1,q_2)$ and $P'(q_2,q_3) = P(q_2,q_3)$. However, $P(q_1,q_2,q_3)$ can not reproduce $P(q_1,q_3)$, i.e., $P'(q_1,q_3) \neq P(q_1,q_3)$, in general. While for a macrorealistic world $P'(q_i,q_j) = P(q_i,q_j)$ The above concept can be investigated experimentally by measuring the three-time JP, as described in Fig. 4.2c. Since this experiment requires measurements at three time instants, we need two ancilla qubits along with the system qubit. Here the first spin (F_1) is used as the

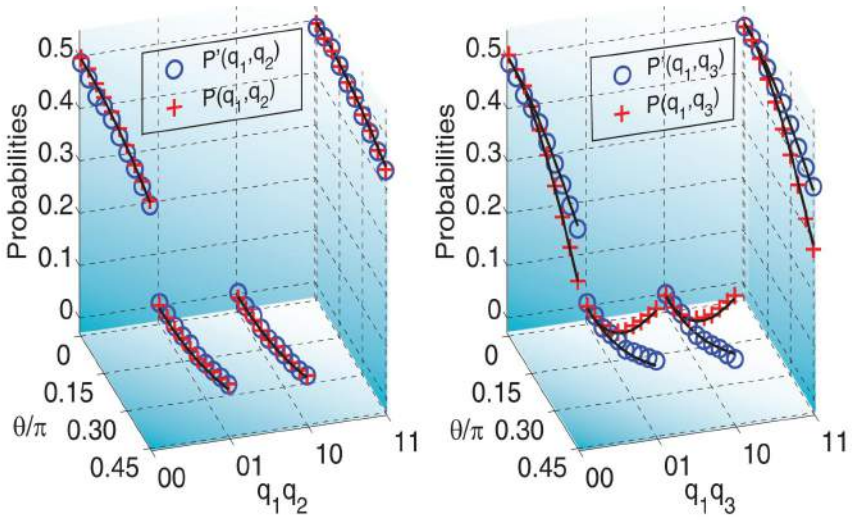

Figure 4.7: (a) Joint probabilities $P(q_1, q_2)$ and marginal probabilities $P'(q_1, q_2)$, and (b) joint probabilities $P(q_1, q_3)$ and marginal probabilities $P'(q_1, q_3)$. The lines correspond to theoretical values and the symbols are mean experimental values.

system qubit and the others (F_2 and F_3) are chosen as the ancilla qubits shown in Fig. 4.4d. The effective ^{19}F transverse relaxation time constants T_2^* were about 0.8 s and their longitudinal relaxation time constants were all longer than 6.3 s. The experiments were carried out at an ambient temperature of 300 K. The initialization involved evolution of an equilibrium deviation density matrix under the following sequence to prepare the state $\rho_{in} = \frac{1-\epsilon}{8}\mathbb{I} + \epsilon\left\{\frac{1}{2}\mathbb{I}_S \otimes |00\rangle\langle 00|_A\right\}$ as shown in Fig. 4.4e. Where $\epsilon \sim 10^{-5}$ is the purity

factor [38].

$$
\begin{aligned}
& S_{1z} + S_{2z} + S_{3z} \\
& \qquad \downarrow \qquad (\pi/2)_{1x}(\pi/3)_{3x}, \text{PFG} \\
& S_z^2 + \tfrac{1}{2} S_{3z} \\
& \qquad \downarrow \qquad (\pi/4)_{2x} \\
& \tfrac{1}{\sqrt{2}} S_{2z} - \tfrac{1}{\sqrt{2}} S_{2y} + \tfrac{1}{2} S_{3z} \\
& \qquad \downarrow \qquad 1/(2J_{23}) \\
& \tfrac{1}{\sqrt{2}} S_{2z} + \sqrt{2} S_{2x} S_{3z} + \tfrac{1}{2} S_{3z} \\
& \qquad \downarrow \qquad (\pi/4)_{-2y}, \text{PFG} \\
& \tfrac{1}{2}(S_{2z} + 2 S_{2z} S_{3z} + S_{3z}).
\end{aligned}
$$

First the experimental three-time JP $P(q_1, q_2, q_3)$ were obtained using the circuit Fig. 4.2c. Two-time MP $P'(q_i, q_j)$ were obtained using Eqs. (7). Note that the circuits measuring higher order JP can also be used to retrieve lower order JP by selectively tracing out qubits. Therefore, two-time JP $P(q_i, q_j)$ were measured directly with the same circuit Fig. 4.2c; here the JP are completely stored in the ancilla qubits, and were obtained by tracing out the system qubit. The experimental results of $P(q_1, q_2)$ and $P'(q_2, q_3)$ are shown in Fig. 4.7a. It is evident that the marginals agree quite well with the corresponding JP. Similarly experimental results of $P(q_1, q_3)$ and $P'(q_1, q_3)$ are shown in Fig. 4.7b . These results show, in contrary to the macrorealistic theory, that the grand probability $P(q_1, q_2, q_3)$ can not reproduce all the two-time joint probabilities as the marginals. Therefore the grand probability is not legitimate in the quantum case, which is the fundamental reason for the violation of the ELGI by quantum systems [1]. It is interesting to note that even for those values of θ for which D_3 is positive, the three-time joint probability is illegitimate. Therefore, while the violation of the ELGI indicates the quantumness of the system, its satisfaction does not rule out the quantumness.

4.1.6 Conclusions

The entropic Leggett-Garg inequalities, imposes bounds on the statistical outcomes of temporal correlations of observables. I described an experimental study of the entropic Leggett-Garg inequality in nuclear spins using NMR techniques. We employed the recently described 'ideal negative result' procedure to noninvasively extract JP. Our results indicate the macrorealistic bound being violated by over four standard deviations, confirming the non-macrorealistic nature of the spin-1/2 particles. Quantum systems do not have legitimate joint probability distribution, which results in the violation of bounds set-up for macrorealistic systems. We have experimentally measured the three-time JP and confirmed that it can not reproduce all the two-time JP.

One distinct feature of the entropic LGI is that, the dichotomic nature of observables assumed in the original formulation of LGI can be relaxed, thus allowing one to study the quantum behavior of higher dimensional systems such as spin $> 1/2$ systems. This could be an interesting topic for future experimental investigations.

4.2 Retrieving joint probabilities by inversion of moments

4.2.1 Introduction

The issue of determining a probability distribution uniquely in terms of its moment sequence – known as *classical moment problem* – has been developed for more than 100 years [107, 108]. In the case of discrete distributions with the associated random variables taking finite values, moments faithfully capture the essence of the probabilities i.e., the probability distribution is moment determinate [109]. In the special case of classical random variables X_i assuming dichotomic values $x_i = \pm 1$, it is easy to see that the sequence of moments.

$$\mu_{n_1,n_2,\cdots,n_k} = \langle X_1^{n_1} X_2^{n_2} \cdots X_k^{n_k} \rangle = \sum_{x_1,x_2,\cdots,x_k=\pm 1} \{x_1^{n_1}, x_2^{n_2}, \cdots, x_k^{n_k}\} P(x_1, x_2, \cdots, x_k) \qquad (4.11)$$

where $n_1, n_2, \cdots, n_k = 0, 1$, can be readily inverted to obtain the joint probabilities $P(x_1, x_2, \cdots, x_k)$ uniquely. More explicitly, the joint probabilities $P(x_1, x_2, \cdots, x_k)$ are given in terms of the 2^k moments $\mu_{n_1,n_2,\cdots,n_k}, n_1, n_2, \cdots n_k = 0, 1$ as,

$$\begin{aligned} P(x_1, x_2, \cdots, x_k) &= \frac{1}{2^k} \sum_{n_1,\cdots,n_k=0,1} x_1^{n_1} x_2^{n_2} \cdots x_k^{n_k} \mu_{n_1,\cdots,n_k} \\ &= \frac{1}{2^k} \sum_{n_1,\cdots,n_k=0,1} x_1^{n_1} x_2^{n_2} \cdots x_k^{n_k} \langle X_1^{n_1} X_2^{n_2} \cdots X_k^{n_k} \rangle. \end{aligned} \tag{4.12}$$

Does this feature prevail in the quantum scenario? This results in a negative answer as it is wellknown that the moments associated with measurement outcomes on spatially separated parties are not compatible with the joint probability distribution. This feature reflects itself in the violation of Bell inequalities. In this paper we investigate whether moment-indeterminacy persists when we focus on sequential measurements on a single quantum system. We show that the discrete joint probabilities originating in the sequential measurement of a single qubit dichotomic observable $\hat{X}(t_i) = \hat{X}_i$ at different time intervals are not consistent with the ones reconstructed from the moments. More explicitly, considering sequential measurements of $\hat{X}_1$, $\hat{X}_2$, $\hat{X}_3$, we reconstruct the trivariate joint probabilties $P_\mu(x_1, x_2, x_3)$ based on the set of eight moments $\{\langle \hat{X}_1 \rangle, \langle \hat{X}_2 \rangle, \langle \hat{X}_3 \rangle, \langle \hat{X}_1, \hat{X}_2 \rangle, \langle \hat{X}_2, \hat{X}_3 \rangle, \langle \hat{X}_1, \hat{X}_3 \rangle, \langle \hat{X}_1, \hat{X}_2, \hat{X}_3 \rangle\}$ and prove that they do not agree with the three-time joint probabilities (TTJP) $P_d(x_1, x_2, x_3)$ evaluated directly based on the correlation outcomes in the sequential measurement of all the three observables. Interestingly, the moments and TTJP can be independently extracted experimentally in NMR system – demonstrating the difference between moment inverted three time probabilities with the ones directly drawn from experiment, in agreement with theory. For obtaining TTJP directly we use the procedure of Ref. [110] and for extracting moments we extend the Moussa protocol [111] to a set of non-commutating observables. The specifics are given in the experimental section. Disagreement between moment inverted joint probabilities with the ones based on measurement outcomes in turn reflects the inherent inconsistency that the family of all marginal probabilities do not arise from the grand joint probabilities. The non-existence

of a legitimate grand joint probability distribution, consistent with the set of all pairwise marginals is attributed to be the common origin of a wide range of no-go theorems on non-contextuality, locality and macrorealism in the foundations of quantum theory [1, 89, 94, 112–116]. Absence of a valid grand joint probability distribution in the sequential measurement on a single quantum system is brought out here in terms of its mismatch with moment sequence. I organize the chapter as follows. In subsec. 4.2.2, I begin with a discussion on moment inversion to obtain joint probabilities of three classical random variables assuming dichotomic values ±1. In subsec. 4.2.3, I report our study for the quantum scenario with the help of a specific example of sequential measurements of dichotomic observable at three different times on a spin-1/2 system. We have shown that the TTJP constructed from eight moments do not agree with those originated from the measurement outcomes. Subsec. 4.2.4 is devoted to report experimental results with NMR implementation on an ensemble of spin-1/2 nuclei, demonstrating that moment constructed TTJP do not agree with those directly extracted. Subsec. 4.2.5 has concluding remarks.

4.2.2 Reconstruction of joint probability of classical dichotomic random variables from moments

Let X denote a dichotomic random variable with outcomes $x = \pm 1$. The moments associated with statistical outcomes involving the variable X are given by $\mu_n = \langle X^n \rangle = \sum_{x=\pm 1} x^n P(x), n = 0, 1, 2, 3, \cdots$, where $0 \leq P(x = \pm 1) \leq 1; \sum_{x=\pm 1} P(x) = 1$ are the corresponding probabilities. Given the moments μ_0 and μ_1 from a statistical trial, one can readily obtain the probability mass function:

$$P(1) = \frac{1}{2}(\mu_0 + \mu_1) = \frac{1}{2}(1 + \mu_1), \tag{4.13}$$

$$P(-1) = \frac{1}{2}(\mu_0 - \mu_1) = \frac{1}{2}(1 - \mu_1); \tag{4.14}$$

i.e., moments determine the probabilities uniquely. In the case of two dichotomic random variables X_1, X_2, the moments $\mu_{n_1,n_2} = \langle X_1^{n_1} X_2^{n_2} \rangle = \sum_{x_1=\pm 1, x_2=\pm 1} x_1^{n_1} x_2^{n_2} P(x_1, x_2)$ where

$n_1, n_2 = 0, 1 \cdots$ encode the bivariate probabilities $P(x_1, x_2)$. Explicitly,

$$\begin{aligned}
\mu_{00} &= \sum_{x_1,x_2=\pm 1} P(x_1, x_2) = P(1,1) + P(1,-1) + P(-1,1) + P(-1,-1) = 1, \\
\mu_{10} &= \sum_{x_1,x_2=\pm 1} x_1 P(x_1, x_2) = \sum_{x_1=\pm 1} x_1 P(x_1) \\
&= P(1,1) + P(1,-1) - P(-1,1) - P(-1,-1), \\
\mu_{01} &= \sum_{x_1,x_2=\pm 1} x_2 P(x_1, x_2) = \sum_{x_2} x_2 P(x_2) \\
&= P(1,1) - P(1,-1) + P(-1,1) - P(-1,-1), \\
\mu_{11} &= \sum_{x_1,x_2=\pm 1} x_1 x_2 P(x_1, x_2) = P(1,1) - P(1,-1) - P(-1,1) + P(-1,-1). \quad (4.15)
\end{aligned}$$

Note that the moments μ_{10}, μ_{01} involve the MP $P(x_1) = \sum_{x_2=\pm 1} P(x_1, x_2)$, $P(x_2) = \sum_{x_1=\pm 1} P(x_1, x_2)$ respectively and they could be evaluated based on statistical trials drawn independently from the two random variables X_1 and X_2. Given the moments $\mu_{00}, \mu_{10}, \mu_{01}, \mu_{11}$ the reconstruction of the probabilities $P(x_1, x_2)$ is straightforward:

$$\begin{aligned}
P(x_1, x_2) &= \frac{1}{4} \sum_{n_1,n_2=0,1} x_1^{n_1} x_2^{n_2} \mu_{n_1,n_2} \\
&= \frac{1}{4} \sum_{n_1,n_2=0,1} \langle X_1^{n_1} X_2^{n_2} \rangle. \quad (4.16)
\end{aligned}$$

Further, a reconstruction of trivariate JP $P(x_1, x_2, x_3)$ requires the following set of eight moments: $\{\mu_{000} = 1, \mu_{100} = \langle X_1 \rangle, \mu_{010} = \langle X_2 \rangle, \mu_{001} = \langle X_3 \rangle, \mu_{110} = \langle X_1, X_2 \rangle, \mu_{011} = \langle X_2, X_3 \rangle, \mu_{101} = \langle X_1, X_3 \rangle, \ \mu_{111} = \langle X_1, X_2, X_3 \rangle\}$. The probabilities are retrieved faithfully in terms of the eight moments as,

$$\begin{aligned}
P(x_1, x_2, x_3) &= \frac{1}{8} \sum_{n_1,n_2,n_3=0,1} x_1^{n_1} x_2^{n_2} x_3^{n_3} \mu_{n_1,n_2,n_3} \\
&= \frac{1}{8} \sum_{n_1,n_2,n_3=0,1} x_1^{n_1} x_2^{n_2} x_3^{n_3} \langle X_1^{n_1} X_2^{n_2} X_3^{n_3} \rangle.
\end{aligned} \quad (4.17)$$

It is implicit that the moments $\mu_{100}, \mu_{010}, \mu_{001}$ are determined through independent statistical trials involving the random variables X_1, X_2, X_3 separately; $\mu_{110}, \mu_{011}, \mu_{101}$ are obtained

based on the correlation outcomes of (X_1, X_2), (X_2, X_3), and (X_1, X_3) respectively. More specifically, in the classical probability setting there is a tacit underlying assumption that the set of all MP $P(x_1), P(x_2), P(x_3), P(x_1, x_2), P(x_2, x_3), and P(x_1, x_3)$ are consistent with the trivariate JP $P(x_1, x_2, x_3)$. This underpinning does not get imprinted automatically in the quantum scenario. Suppose the observables $\hat{X}_1, \hat{X}_2, \hat{X}_3$ are non-commuting and we consider their sequential measurement. The moments $\mu_{100} = \langle \hat{X}_1 \rangle, \mu_{010} = \langle \hat{X}_2 \rangle$, $\mu_{001} = \langle \hat{X}_3 \rangle$ may be evaluated from the measurement outcomes of dichotomic observables $\hat{X}_1, \hat{X}_2, \hat{X}_3$ independently; the correlated statistical outcomes in the sequential measurements of $(\hat{X}_1, \hat{X}_2)$, $(\hat{X}_2, \hat{X}_3)$ and $(\hat{X}_1, \hat{X}_3)$ allow one to extract the set of moments $\mu_{110} = \langle \hat{X}_1 \hat{X}_2 \rangle, \mu_{011} = \langle \hat{X}_2 \hat{X}_3 \rangle, \mu_{101} = \langle \hat{X}_1 \hat{X}_3 \rangle$; further the moment $\mu_{111} = \langle \hat{X}_1 \hat{X}_2 \hat{X}_3 \rangle$ is evaluated based on the correlation outcomes when all the three observables are measured sequentially. The JP $P_\mu(x_1, x_2, x_3)$ retrieved from the moments as given in (4.17) differ from the ones evaluated directly in terms of the correlation outcomes in the sequential measurement of all the three observables. We illustrate this inconsistency appearing in the quantum setting in the next section.

4.2.3 Quantum three-time JP and moment inversion

Let us consider a spin-1/2 system, dynamical evolution of which is governed by the Hamiltonian

$$\hat{H} = \frac{1}{2}\hbar\omega\sigma_x. \tag{4.18}$$

We choose z-component of spin as our dynamical observable:

$$\begin{aligned} \hat{X}_i &= \hat{X}(t_i) = \sigma_z'(t_i) \\ &= \hat{U}^\dagger(t_i)\sigma_z\hat{U}(t_i) \\ &= \sigma_z \cos\omega t_i + \sigma_y \sin\omega t_i. \end{aligned} \tag{4.19}$$

where $\hat{U}(t_i) = e^{-i\sigma_x \omega t_i/2} = \hat{U}_i$ and consider sequential measurements of the observable $\hat{X}_i$ at three different times $t_1 = 0$, $t_2 = \Delta t$, and $t_3 = 2\Delta t$:

$$\begin{aligned}
\hat{X}_1 &= \sigma_z, \\
\hat{X}_2 &= \sigma_z'(\Delta t) = \sigma_z \cos(\omega \Delta t) + \sigma_y \sin(\omega \Delta t), \\
\hat{X}_3 &= \sigma_z'(2\Delta t) = \sigma_z \cos(2\omega \Delta t) + \sigma_y \sin(2\omega \Delta t).
\end{aligned} \tag{4.20}$$

Note that these three operators are not commuting in general.

The moments $\langle \hat{X}_1 \rangle, \langle \hat{X}_2 \rangle, \langle \hat{X}_3 \rangle$ are readily evaluated to be

$$\mu_{100} = \langle \hat{X}_1 \rangle = \mathrm{Tr}[\hat{\rho}_{\mathrm{in}} \sigma_z] = 0, \tag{4.21}$$

$$\mu_{010} = \langle \hat{X}_2 \rangle = \mathrm{Tr}[\hat{\rho}_{\mathrm{in}} \sigma_z'(\Delta t)] = 0, \tag{4.22}$$

$$\mu_{001} = \langle \hat{X}_3 \rangle = \mathrm{Tr}[\hat{\rho}_{\mathrm{in}} \sigma_z'(2\Delta t)] = 0. \tag{4.23}$$

when the system density matrix is prepared initially in a maximally mixed state $\hat{\rho}_{\mathrm{in}} = \mathbb{I}/2$. The probabilities of outcomes $x_i = \pm 1$ in the completely random initial state are given by $P(x_i = \pm 1) = \mathrm{Tr}[\hat{\rho}_{\mathrm{in}} \hat{\Pi}_{x_i}] = \frac{1}{2}$, where $\hat{\Pi}_{x_i} = |x_i\rangle\langle x_i|$ is the projection operator corresponding to measurement of the observable $\hat{X}_i$.

The two-time JP arising in the sequential measurements of the observables $\hat{X}_i, \hat{X}_j, for j > i$ are evaluated as follows. The measurement of the observable $\hat{X}_i$ yielding the outcome $x_i = \pm 1$ projects the density operator to $\hat{\rho}_{x_i} = \frac{\hat{\Pi}_{x_i} \hat{\rho}_{\mathrm{in}} \hat{\Pi}_{x_i}}{\mathrm{Tr}[\hat{\rho}_{\mathrm{in}} \hat{\Pi}_{x_i}]}$. Further, a sequential measurement of $\hat{X}_j$ leads to the two-time JP as,

$$\begin{aligned}
P(x_i, x_j) &= P(x_i) P(x_j | x_i) \\
&= \mathrm{Tr}[\hat{\rho}_{\mathrm{in}} \hat{\Pi}_{x_i}] \mathrm{Tr}[\hat{\rho}_{x_i} \hat{\Pi}_{x_j}] \\
&= \mathrm{Tr}[\hat{\Pi}_{x_i} \hat{\rho}_{\mathrm{in}} \hat{\Pi}_{x_i} \hat{\Pi}_{x_j}] \\
&= \langle x_i | \hat{\rho}_{\mathrm{in}} | x_i \rangle |\langle x_i | x_j \rangle|^2.
\end{aligned} \tag{4.24}$$

We evaluate the two-time JP associated with the sequential measurements of $(\hat{X}_1, \hat{X}_2)$,

$(\hat{X}_2, \hat{X}_3)$, and $(\hat{X}_1, \hat{X}_3)$ explicitly:

$$P(x_1, x_2) = \frac{1}{4}[1 + x_1 x_2 \cos(\omega \Delta t)], \tag{4.25}$$

$$P(x_2, x_3) = \frac{1}{4}[1 + x_2 x_3 \cos(\omega \Delta t)], \tag{4.26}$$

$$P(x_1, x_3) = \frac{1}{4}[1 + x_1 x_3 \cos(2\omega \Delta t)]. \tag{4.27}$$

We then obtain two-time correlation moments as,

$$\begin{aligned} \mu_{110} = \langle \hat{X}_1 \hat{X}_2 \rangle &= \sum_{x_1, x_2 = \pm 1} x_1 x_2 P(x_1, x_2) \\ &= \frac{1}{2} \cos(\omega \Delta t)], \end{aligned} \tag{4.28}$$

$$\begin{aligned} \mu_{011} = \langle \hat{X}_2 \hat{X}_3 \rangle &= \sum_{x_2, x_3 = \pm 1} x_2 x_3 P(x_2, x_3) \\ &= \frac{1}{2} \cos(\omega \Delta t)], \end{aligned} \tag{4.29}$$

$$\begin{aligned} \mu_{101} = \langle \hat{X}_1 \hat{X}_3 \rangle &= \sum_{x_1, x_3 = \pm 1} x_1 x_3 P(x_1, x_3) \\ &= \frac{1}{2} \cos(2\omega \Delta t)]. \end{aligned} \tag{4.30}$$

Further, the three-time JP $P(x_1, x_2, x_3)$ arising in the sequential measurements of $\hat{X}_1, \hat{X}_2$ followed by $\hat{X}_3$ are given by

$$\begin{aligned} P(x_1, x_2, x_3) &= P(x_1) P(x_2|x_1) P(x_3|x_1, x_2) \\ &= \mathrm{Tr}[\hat{\rho}_{\mathrm{in}} \hat{\Pi}_{x_1}] \mathrm{Tr}[\hat{\rho}_{x_1} \hat{\Pi}_{x_2}] \mathrm{Tr}[\hat{\rho}_{x_2} \hat{\Pi}_{x_3}] \end{aligned} \tag{4.31}$$

where $\hat{\rho}_{x_2} = \frac{\hat{\Pi}_{x_2}\hat{\rho}_{x_1}\hat{\Pi}_{x_2}}{\mathrm{Tr}[\hat{\rho}_{x_1}\hat{\Pi}_{x_2}]}$. We obtain,

$$\begin{aligned} P(x_1,x_2,x_3) &= \mathrm{Tr}[\hat{\Pi}_{x_2}\hat{\Pi}_{x_1}\hat{\rho}_{\mathrm{in}}\hat{\Pi}_{x_1}\hat{\Pi}_{x_2}\hat{\Pi}_{x_3}] \\ &= \langle x_1|\hat{\rho}_{\mathrm{in}}|x_1\rangle|\langle x_1|x_2\rangle|^2|\langle x_2|x_3\rangle|^2 \\ &= \frac{P(x_1,x_2)P(x_2,x_3)}{\langle x_2|\hat{\rho}_{\mathrm{in}}|x_2\rangle} \\ &= \frac{P(x_1,x_2)P(x_2,x_3)}{P(x_2)}, \end{aligned} \tag{4.32}$$

where in the third line of (4.32) we have used (4.24). The three-time correlation moment is evaluated to be,

$$\begin{aligned} \mu_{111} = \langle \hat{X}_1\hat{X}_2\hat{X}_3\rangle &= \sum_{x_1,x_2,x_3=\pm 1} x_1x_2x_3P(x_1,x_2,x_3) \\ &= 0. \end{aligned} \tag{4.33}$$

From the set of eight moments (4.21), (4.28) and (4.33), we construct the TTJP (see (4.17) as,

$$\begin{aligned} P_\mu(1,1,1) &= \frac{1}{8}[1+2\cos(\omega\Delta t)+\cos(2\omega\Delta t)] = P_\mu(-1,-1,-1), \\ P_\mu(-1,1,1) &= \frac{1}{8}[1-\cos(2\omega\Delta t)] = P_\mu(-1,-1,1) = P_\mu(1,1,-1) = P_\mu(1,-1,-1), \\ P_\mu(1,-1,1) &= \frac{1}{8}[1-2\cos(\omega\Delta t)+\cos(2\omega\Delta t)] = P_\mu(-1,1,-1). \end{aligned} \tag{4.34}$$

On the other hand, the three dichotomic variable quantum probabilities $P(x_1,x_2,x_3)$ evaluated directly are given by,

$$\begin{aligned} P_d(1,1,1) &= \frac{1}{8}[1+\cos(\omega\Delta t)]^2 = P_d(-1,-1,-1), \\ P_d(-1,1,1) &= \frac{1}{8}[1-\cos^2(\omega\Delta t)] = P_d(-1,-1,1) = P_d(1,1,-1) = P_d(1,-1,-1), \\ P_d(1,-1,1) &= \frac{1}{8}[1-\cos(\omega\Delta t)]^2 = P_d(-1,1,-1). \end{aligned} \tag{4.35}$$

Clearly, there is no agreement between the moment inverted TTJP (4.34) and the ones of (4.35) directly evaluated. In other words, the TTJP realized in a sequential measurement

are not invertible in terms of the moments which in turn reflects the incompatibility of the set of all MP with the grand JP $P_d(x_1, x_2, x_3)$. In fact, it may be explicitly verified that $P(x_1, x_3) \neq \sum_{x_2=\pm1} P_d(x_1, x_2, x_3)$. Moment-indeterminacy points towards the absence of a valid grand probability distribution consistent with all the marginals.

The TTJP and moments can be independently extracted experimentally using NMR methods on an ensemble of spin-1/2 nuclei. The experimental approach and results are reported in the next section.

4.2.4 Experiment

The projection operators at time $t = 0$ ($\hat{X}_1 = \sigma_z$) are $\{\hat{\Pi}_{x_i^0} = |x_i^0\rangle\langle x_i^0|\}_{x_i^0=0,1}$. This measurement basis is rotating under the unitary $\hat{U}_i$, resulting in time dependent basis given by, $\hat{\Pi}_{x_i^t} = \hat{U}_i^\dagger \hat{\Pi}_{x_i^0} \hat{U}_i$. While doing experiments it is convenient to perform the measurement in the computational basis as compared to the time dependent basis. This can be done as follows: We can expand the measurement on an instantaneous state $\rho(t_i)$ as, $\hat{\Pi}_{x_i^t}\hat{\rho}(t_i)\hat{\Pi}_{x_i^t} = \hat{U}_i^\dagger \hat{\Pi}_{x_i^0} \left(\hat{U}_i\hat{\rho}(t_i)\hat{U}_i^\dagger\right) \Pi_{x_i^0} U_i$. Thus, measuring in time dependent basis is equivalent to evolving the state under the unitary $\hat{U}_i$, followed by measuring in the computational basis and lastly evolving under the unitary $\hat{U}_i^\dagger$. As explained before, the JP were measured using the circuit shown in Fig. 4.2c. Circuit shown in Fig. 4.2c has two controlled gates for encoding the outcomes of first and second measurements on to the first and second ancilla qubits respectively. A set of four experiments are to be performed, with following arrangement of first and second controlled gates for measurement of the TTJP: (i) CNOT; CNOT, (ii) anti-CNOT; CNOT, (iii) CNOT; anti-CNOT, and (iv) anti-CNOT; anti-CNOT. The propagators $\hat{U}_i = e^{-i\sigma_x\omega t_i/2}$ is realized by the cascade $H\hat{U}_d H$, where H is the Hadamard gate, and the delay propagator $\hat{U}_d = e^{-i\sigma_z\omega t_i/2}$ corresponds to the z-precession of the system qubit at $\omega = 2\pi 100$ rad/s resonance off-set. The diagonal tomography was performed at the end to determine the probabilities [110]. The experimental profile shown in Fig. 4.10 was obtained by varying Δt such that $\theta = \omega\Delta t \in [0, \pi]$.

The three qubits were provided by the three ^{19}F nuclear spins of trifluoroiodoethylene dissolved in acetone-D6. The structure of the molecule is shown in Fig. 4.4c and the chemical shifts and the scalar coupling values (in Hz) in Fig. 4.4d. The effective ^{19}F

spin-lattice (T_2^*) and spin-spin (T_1) relaxation time constants were about 0.8s and 6.3 s respectively. The experiments were carried out at an ambient temperature of 290 K on a 500 MHz Bruker UltraShield NMR spectrometer. The first spin (F_1) is used as the system qubit and, other spins (F_2 and F_3) as the ancilla qubits. Initialization involved preparing the state, $\frac{1-\epsilon}{8}\mathbb{I} + \epsilon\left\{\frac{I}{2}\mathbb{I}_S \otimes |00\rangle\langle 00|_A\right\}$ where $\epsilon \sim 10^{-5}$ is the purity factor [117]. The pulse sequence to prepare this state from the equilibrium state is shown in Fig. 4.4(e). All pulses were numerically optimized using the GRAPE technique [43] and had fidelities better than 0.999. With our choice of measurement model (Fig. 4.2c) we find a striking agreement with theoretical results on TTJP (4.35) . Our measurement scheme provides an optimal procedure to preserve the state information, thus resulting in an excellent agreement of experimental results on TTJP with theoretical prediction (see Fig. 4.10).

For calculating the moments we utilize the Moussa protocol [111], which requires only two spins in our case. We utilize F_1 as the system and F_2 as the ancilla qubit. F_3 was decoupled using π pulses and the initialization involved preparing the state, $\frac{1-\epsilon}{8}\mathbb{I} + \epsilon\left\{\frac{1}{2}\mathbb{I}_S \otimes |+\rangle\langle +|_A \otimes |0\rangle\langle 0|\right\}$, which is obtained by applying the Hadamard gate to F_2 after the pulse sequence shown in Fig. 4.4c. The circuit for measuring moments by Moussa

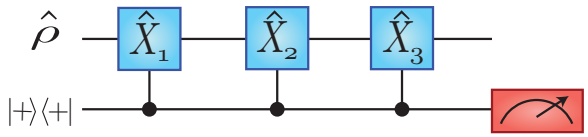

Figure 4.8: Moussa Protocol for obtaining the 3-time correlated moments. One and two time moments can be calculated using the appropriate number of controlled gates.

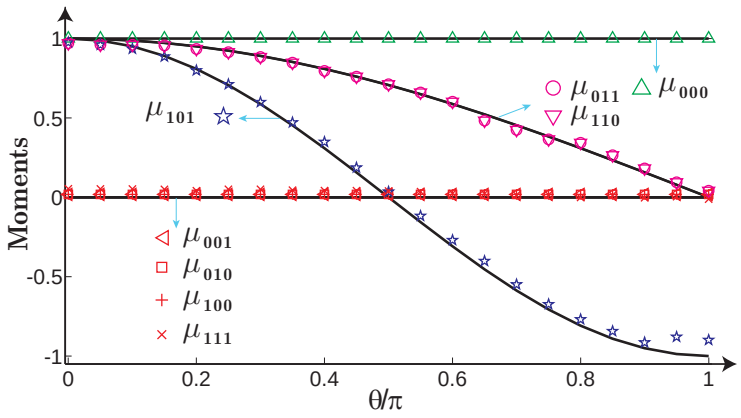

Figure 4.9: Moments obtained experimentally from Moussa Protocol. The symbols represent experimentally obtained values of the indicated moments with the solid lines showing the corresponding theoretical values. Here $\theta = \omega\Delta t$.

protocol is shown in Fig. 4.8 and it proceeds as follows,

$$\hat{\rho} \otimes |+\rangle\langle+|$$
$$\downarrow \mathrm{c}\hat{\mathrm{X}}_1$$
$$\hat{\rho}\hat{\mathrm{X}}_1^\dagger \otimes |0\rangle\langle 1| + \hat{\mathrm{X}}_1\hat{\rho} \otimes |1\rangle\langle 0|+$$
$$\hat{\rho} \otimes |0\rangle\langle 0| + \hat{\mathrm{X}}_1\hat{\rho}\hat{\mathrm{X}}_1^\dagger \otimes |1\rangle\langle 1|$$
$$\downarrow \mathrm{c}\hat{\mathrm{X}}_2$$
$$\hat{\rho}\hat{\mathrm{X}}_1^\dagger\hat{\mathrm{X}}_2^\dagger \otimes |0\rangle\langle 1| + \hat{\mathrm{X}}_2\hat{\mathrm{X}}_1\hat{\rho} \otimes |1\rangle\langle 0|+$$
$$\hat{\rho} \otimes |0\rangle\langle 0| + \hat{\mathrm{X}}_2\hat{\mathrm{X}}_1\rho\hat{\mathrm{X}}_1^\dagger\hat{\mathrm{X}}_2^\dagger \otimes |1\rangle\langle 1|$$
$$\downarrow \mathrm{c}\hat{\mathrm{X}}_3$$
$$\hat{\rho}\hat{\mathrm{X}}_1^\dagger\hat{\mathrm{X}}_2^\dagger\hat{\mathrm{X}}_3^\dagger \otimes |0\rangle\langle 1| + \hat{\mathrm{X}}_3\hat{\mathrm{X}}_2\hat{\mathrm{X}}_1\hat{\rho} \otimes |1\rangle\langle 0|+$$
$$\hat{\rho} \otimes |0\rangle\langle 0| + \hat{\mathrm{X}}_3\hat{\mathrm{X}}_2\hat{\mathrm{X}}_1\hat{\rho}\hat{\mathrm{X}}_1^\dagger\hat{\mathrm{X}}_2^\dagger\hat{\mathrm{X}}_3^\dagger \otimes |1\rangle\langle 1|,$$

where, $\mathrm{c}\hat{\mathrm{X}}_\mathrm{i}$ represents the controlled gates and $\hat{\rho}$ is the initial state of the system. The state of the ancilla qubit ($\hat{\rho}_a$) at the end of the circuit is given by,

$$\begin{aligned}\hat{\rho}_a &= |0\rangle\langle 1|\mathrm{Tr}(\hat{\rho}\hat{X}_1^\dagger\hat{X}_2^\dagger\hat{X}_3^\dagger) + |1\rangle\langle 0|\mathrm{Tr}(\hat{X}_3\hat{X}_2\hat{X}_1\hat{\rho}) \\ &\quad +|0\rangle\langle 0|\mathrm{Tr}(\hat{\rho}) + |1\rangle\langle 1|\mathrm{Tr}(\hat{X}_3\hat{X}_2\hat{X}_1\hat{\rho}\hat{X}_1^\dagger\hat{X}_2^\dagger\hat{X}_3^\dagger).\end{aligned}$$

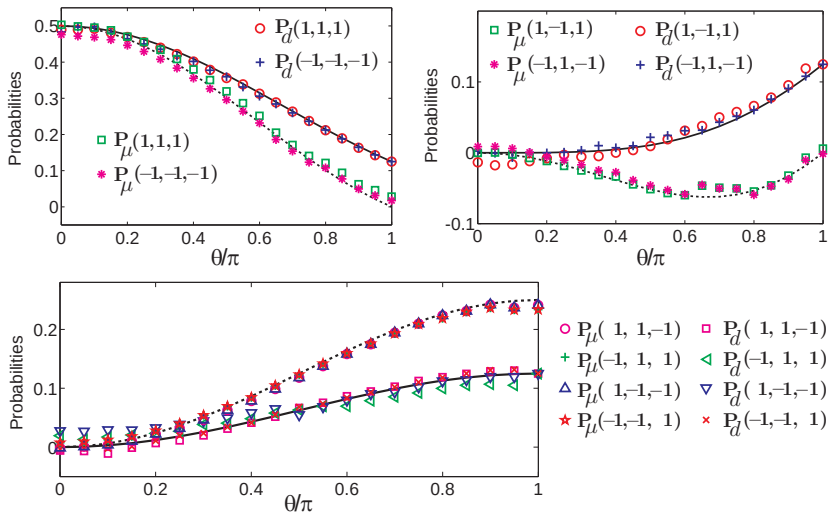

Figure 4.10: Three-time JP (TTJP): The solid curves represent the probabilities measured directly and the dashed curve the probabilities obtained by inverting the moments. The symbols represents the experimental data. The mismatch between the directly measured and the inverted moments indicate the illegitimacy of the grand probability distribution.

Moussa protocol was originally proposed for commuting observables, however, it can be easily extended to non-commuting observables. The NMR measurements correspond to the expectation values of spin angular momentum operators I_x or I_y [34]. The measurement of the I_x for ancilla qubit at the end of the circuit gives:

$$\mathrm{Tr}[\hat{\rho}_a I_x] = \mathrm{Tr}[\hat{X}_3\hat{X}_2\hat{X}_1\hat{\rho}]/2 + \mathrm{Tr}[\hat{\rho}\hat{X}_1^\dagger\hat{X}_2^\dagger\hat{X}_3^\dagger]/2. \tag{4.36}$$

If, $\hat{X}_1, \hat{X}_2, \hat{X}_3$ commute, then the above expression gives $\mathrm{Tr}[\hat{\rho}\hat{X}_1\hat{X}_2\hat{X}_3]$. In case of non-commuting hermitian observables, we also measure expectation value of I_y, which gives :

$$i\mathrm{Tr}[\rho_a I_y] = \mathrm{Tr}[\hat{X}_3\hat{X}_2\hat{X}_1\hat{\rho}]/2 - \mathrm{Tr}[\hat{\rho}\hat{X}_1^\dagger\hat{X}_2^\dagger\hat{X}_3^\dagger]/2. \tag{4.37}$$

From (4.36) and (4.37) we can calculate $\mathrm{Tr}[\hat{\rho}\hat{X}_1\hat{X}_2\hat{X}_3] \equiv \langle\hat{X}_1\hat{X}_2\hat{X}_3\rangle$ for the 3-measurement case. Hence, by using the different number of controlled gates in appropriate order we can calculate all the moments. The experimentally obtained moments for various values $\theta = \omega\Delta t \in [0, \pi]$ are shown in Fig. 4.9. These experimentally obtained moments are inverted according to Eq. (4.17) to calculate the TTJP and are plotted along with the directly obtained TTJP using circuit shown in Fig. 4.4 c as symbols in Fig. 4.10. The

theoretical values for TTJP from moments and the one directly obtained are plotted as solid and dashed lines respectively. The results agree with the predictions of Eqs. (4.34) and (4.35) that the TTJP obtained directly and the one obtained from the inversion of moments do not agree.

4.2.5 Conclusion

In classical probability theory, statistical moments associated with dichotomic random variables determine the probabilities uniquely. When the same issue is explored in the quantum context – with random variables replaced by Hermitian observables (which are in general non-commuting) and the statistical outcomes of observables in sequential measurements are considered – it is shown that the JP do not agree with the ones inverted from the moments. This is explicitly illustrated by considering sequential measurements of a dynamical variable at three different times in the specific example of a spin-1/2 system.An experimental investigation based on NMR methods, where moments and the JP are extracted independently, demonstrates the moment indeterminacy of probabilities, concordant with theoretical observations.

The failure to revert joint probability distribution from its moments points towards its inherent incompatibility with the family of all marginals. In turn, the moment indeterminacy reveals the absence of a legitimate joint probability distribution compatible with the set of all marginal distributions is the root cause behind various no go theorems like Bell theorem and Kochen-Specker theorem which supports the underlying randomness in quantum mechanics and puts constraints on various local hidden variable theories.

Chapter 5

Applications of NOON states

5.1 Introduction

The use of multiple-quantum coherences has several applications in NMR [118]. The NOON state in an N-spin system is the highest multiple quantum coherence i.e. for an N-spin system it is N^{th} quantum coherence which can be written in the form $(|00\cdots0\rangle + |11\cdots1\rangle)/\sqrt{2}$. Such states have found several applications in optics and other fields [119–121]. Recently NMR NOON states have been used to sense ultra-weak magnetic fields [122]. The NOON state can be easily prepared in star-topology systems using CNOT and Hadamard gates as described in the later section. The NOON state has high sensitivity to phase encoding. In NMR, phase encoding can be achieved easily either by static fields or by RF fields. The former is used in the characterization of translational diffusion and the latter is used to characterize the RF inhomogeneities of the NMR probes. Here we describe the advantages of NOON state in both of these applications.

Driven by the internal thermal energy, the atoms or molecules in a bulk matter may exhibit random translational motion, which is termed as translational diffusion [123, 124]. The diffusion constant (D) is described as the amount of a particular substance that diffuses across a unit area in unit time under the influence of a unit concentration gradient [123]. Here we describe the application of NOON state for measuring diffusion constant.

The strength of NMR over other spectroscopy techniques is in the excellent control over quantum dynamics [35]. Coherent control of nuclear spins is achieved by a calibrated set of radio frequency pulses. Achieving high-fidelity quantum control in practice is however limited by radio frequency inhomogeneity (RFI) over the sample volume. RFI characterization is important not only for conventional NMR experiments, but also for designing robust and high-fidelity quantum gates for quantum information studies [42]. In MRI, RFI characterization can help to understand certain image distortions and to correct them [125]. Here we describe a NOON state method to characterize RFI at high RF amplitudes. In §5.2, I describe the preparation of NOON states in star topology spin sys-

tems. §5.3 contains, the description of the measurement of diffusion using NOON state method, and the experimental results obtained on a ten-spin star-topology system. In §5.4 I describe the characterization of RF inhomogeneity (RFI) using NOON states. Finally I conclude in §5.5.

5.2 NOON state in a star-topology system

The NOON state of an N-qubit system is a superposition

$$\begin{aligned} |N00N\rangle &= (|N,0\rangle + |0,N\rangle)/\sqrt{2} \\ &= (|00\cdots0\rangle + |11\cdots1\rangle)/\sqrt{2}, \end{aligned} \tag{5.1}$$

where $|N,0\rangle$ is the state with N qubits being $|0\rangle$ and 0 qubits being $|1\rangle$, and $|0,N\rangle$ is the state with 0 qubits being $|0\rangle$ and N qubits being $|1\rangle$ [126]. The circuit (Fig. 5.1a) for preparing the NOON state consists of a Hadamard gate followed by a C-NOT gate [122] on a quantum register with a single 'control' qubit and a set of $(N-1)$ 'target' qubits initialized in $|00\cdots0\rangle$ state:

$$\begin{aligned} |00\cdots0\rangle \xrightarrow{\text{H}} \frac{1}{\sqrt{2}}(|0\rangle + |1\rangle)|00\cdots0\rangle \xrightarrow{\text{CNOT}^{\otimes(N-1)}} \\ \frac{1}{\sqrt{2}}(|00\cdots0\rangle + |11\cdots1\rangle) = |N00N\rangle. \end{aligned} \tag{5.2}$$

A star-topology spin system AM_{N-1} consisting of a single spin A coupled to a set of $N-1$ magnetically equivalent spins M (see Fig. 5.1c). The star-topology allows parallel implementation of $N-1$ C-NOT gates. For the diffusion experiments, all the CNOT gates can be realized in parallel by just two pulses: $90^M_x - \frac{1}{2J} - 90^M_y$ as shown in Fig. 5.1b. In our experiments, it is unnecessary to begin with a pure $|00\cdots0\rangle$ state. We can start from the thermal equilibrium state at room temperature, and select the coherence pathway that passes through the NOON state. The coherence selection can be achieved rather conveniently with two PFGs, G_2 and $G_3 = -gG_2$, where $g = \gamma_{\text{eff}}/\gamma_A$.

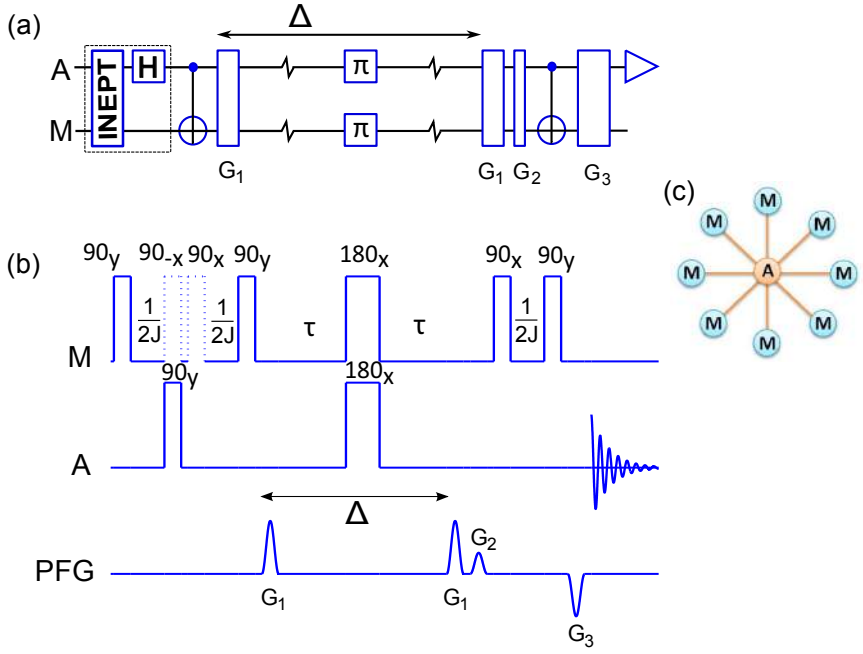

Figure 5.1: (a) Circuit for the measurement of diffusion constant using NOON state, (b) the corresponding NMR pulse sequence, and (c) a star-topology spin-system. Here Δ is the diffusion time, G_1 are diffusion gradients, and G_2 and G_3 are gradients which select out the NOON state. We have used INEPT sequence to transfer magnetization from the M spins to the A spin. In this case, the pseudo-Hadamard gate is not necessary. In (b) second pulse of INEPT cancels with the first pulse of CNOT as shown by dotted lines.

5.3 Measurement of Diffusion constant

Diffusion constant of a liquid can be measured by NMR either with the help of relaxation studies or more conveniently using pulsed-field-gradients (PFGs) [127]. The standard method for measuring diffusion constant consists of two identical PFGs (G_1) separated by diffusion time Δ with a refocusing π pulse in the middle [128, 129].

Due to the random molecular motion, each nuclei in the NMR sample acquires a different relative phase, leading to the decay of average Hahn-echo signal. Theoretically, the decay of this signal S can be given as,

$$S(G_1)/S_0 = \exp\left\{-\gamma^2 G_1^2 \delta^2 D(\Delta - \delta/3)\right\}, \tag{5.3}$$

where D is the diffusion constant, $S_0 = S(0)$ is the normalization factor, and $-\delta/3$ is the correction to Δ due to the finite durations δ of the PFGs [130]. Thus the diffusion constant D can be extracted by systematically varying the strength of the PFGs, G_1, and fitting a Gaussian curve to the experimentally obtained echo intensities. Such PFG methods are widely used for the measurement of diffusion constants and already numerous improved sequences are available [130–132]. For example, long-lived singlet states have been used to study slow diffusion [133, 134], and single-scan measurement of diffusion has been realized by effectively z-coordinate dependent PFG strengths [135].

Although the NOON state method is a special form of the multiple-quantum diffusion experiments [136–138], the star-topology of the spin system, if available, provides a simple way to prepare the NOON states and to convert them back to single quantum coherences.

5.3.1 Diffusion constant via the NOON state

Under the $G_1 - \pi - G_1$ sequence, a spin system in NOON state diffusing through a distance dz acquires a net relative phase:

$$\frac{1}{\sqrt{2}}(|00\cdots0\rangle + |11\cdots1\rangle) \xrightarrow{G_1-\pi-G_1} \frac{1}{\sqrt{2}}(|00\cdots0\rangle + e^{id\phi}|11\cdots1\rangle). \tag{5.4}$$

The relative phase acquired is $d\phi = \gamma_{\text{eff}} dz G_1 \delta$, where $\gamma_{\text{eff}} = \{\gamma_A + (N-1)\gamma_M\} = g\gamma_A$. In the standard diffusion experiments with uncoupled spin 1/2 particles, $N = 0$ and γ_{eff} reduces to γ_A. The larger the value of g, the more sensitive is the NOON state for phase encoding, and allows the study of diffusion with weaker PFGs and smaller durations (Δ) between them. This is the main advantage of using the NOON states. Since NOON state is a multiple quantum coherence, it is necessary to convert it back to single quantum coherence before detection. This conversion can efficiently be carried out using a second

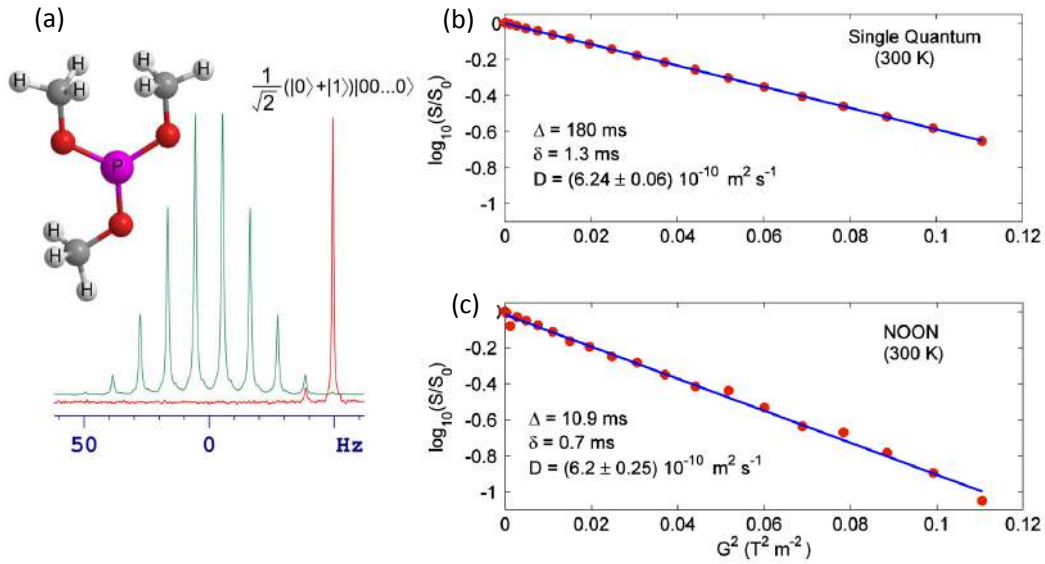

Figure 5.2: (a) ^{31}P spectra of trimethylphosphite corresponding to single quantum excitation from thermal equilibrium (upper trace) and corresponding to the NOON state (lower trace). The molecular structure of trimethylphosphite is shown in the inset. Intensity of the echo signals as a function of the gradient strength G_1 with (b) standard method and (c) the NOON state method. The dots represent the experimental data and the lines represent the linear fit.

set of CNOT gates:

$$\frac{1}{\sqrt{2}}(|00\cdots0\rangle + e^{id\phi}|11\cdots1\rangle) \xrightarrow{\text{CNOT}^{\otimes(N-1)}} \frac{1}{\sqrt{2}}(|0\rangle + e^{id\phi}|1\rangle)|00\cdots0\rangle. \tag{5.5}$$

Thus the phase encoding due to the diffusion, i.e., $d\phi$ has been transfered to one transition of the control spin. In an ensemble of nuclei the above phase encoding results in the attenuation of the control transition. Diffusion constant can be measured by monitoring this attenuation as a function of the PFG strengths [130].

5.3.2 Diffusion Experiments

All the experiments are carried out at 300 K on a 500 MHz Bruker NMR spectrometer. We have studied the diffusion of two samples using the standard method as well as the

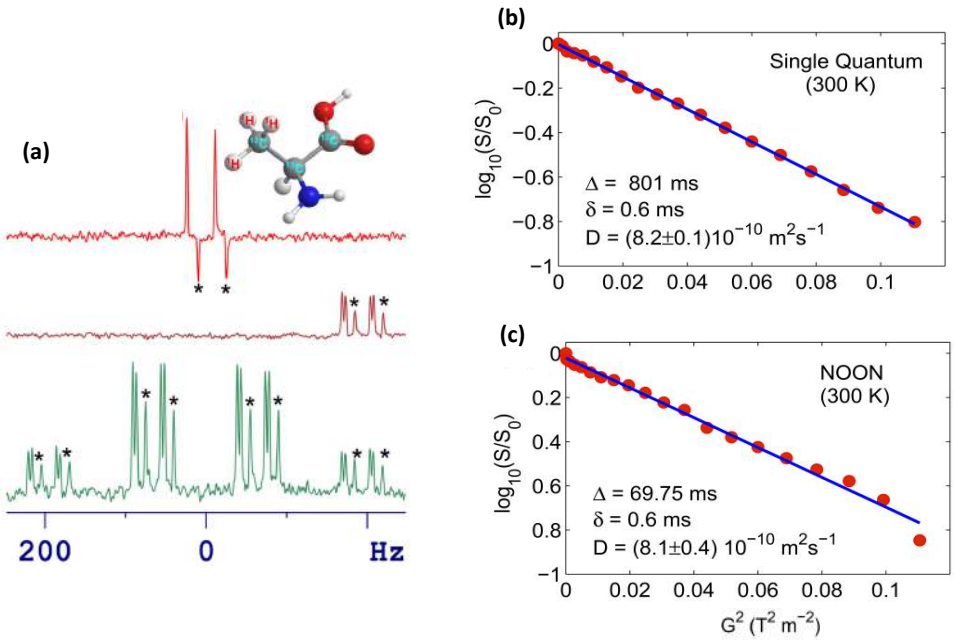

Figure 5.3: (a) ^{13}C spectra of methyl carbon of Alanine corresponding to single quantum excitation from thermal equilibrium (lower trace), and after converting the NOON state into the single quantum coherence using CNOT gates without (middle trace) and with (top trace) subsequent ^{1}H decoupling. The peaks marked with asterisks correspond to different molecules and are to be ignored. Intensity of the echo signals as a function of the gradient strength G_1 with (b) standard method and (c) the NOON state method. The dots represent the experimental data and the lines represent the linear fit.

NOON state method in each case.

First we used 100 μl of trimethylphosphite ($P(OCH_3)_3$ dissolved in 600 μl DMSO-D6) as the star-topology system (Fig. 5.2a). Here each of the nine magnetically equivalent ^{1}H spins are coupled to the ^{31}P spin via indirect spin-spin interaction with a coupling constant of $J = 11$ Hz thus forming an AM_9 spin system. The parameters and the results of single quantum and NOON state experiments are shown in Fig. 5.2b, Fig. 5.2c consecutively. The logarithms of normalized intensities obtained via diffusion experiments are plotted versus G_1^2 in Fig. 5.2. In case of single quantum experiment diffusion constant $D = (6.24 \pm 0.06)10^{-10}$ m^2 s^{-1} was obtained by applying a linear fit based on the expression 5.3. The NOON state diffusion experiments were carried out as described by the pulse sequence in Fig. 5.1b. After an initial INEPT transfer to enhance the ^{31}P polarization, the NOON state was prepared and at the end of the diffusion delay, it was converted back to

a single quantum coherence. To select the 10-quantum coherence pathway, the PFGs G_2 and G_3 were adjusted such that $G_3/G_2 = -g = -(\gamma_P + 9\gamma_H)/\gamma_P = -23.2$.

The results of the NOON state diffusion experiments are shown in Fig. 5.2b. Again a linear fit based on expression 5.3, with an effective gyromagnetic ratio $\gamma_{\text{eff}} = (\gamma_P + 9\gamma_H)$ lead to the diffusion constant of $D = (6.2 \pm 0.25)10^{-10}$ m^2 s^{-1}, which is close to the value obtained from the single quantum method. It can be seen that, in the NOON state method, the diffusion delay is reduced by a factor of 16 and the duration δ of diffusion PFG is reduced by a factor of 2.

The second sample consisted of 5 *mg* of ^{1}3C-labeled alanine in 0.7 *ml* of D_2O. The molecular spectra is shown in Fig. 5.3a. We prepared 4-spin NOON state using the three equivalent protons interacting with the methyl carbon with a coupling con- stant of J = 130 Hz. The parameters and the results of single quantum and NOON state experiments are shown in Fig. 5.3b, Fig. 5.3c consecutively. The logarithms of normalized intensities obtained via diffusion experiments are plotted versus G_1^2 in Fig. 5.3. In case of single quantum experiment diffusion constant $D = (8.2 \pm 0.1)10^{-10}$ m^2 s^{-1} (see Fig. 5.3) was obtained by applying a linear fit based on the expression 5.3. The NOON state diffusion experiments were carried out as described by the pulse sequence in Fig. 5.1b. After an initial INEPT transfer to enhance the ^{31}P polarization, the NOON state was prepared and at the end of the diffusion delay, it was converted back to a single quantum coherence. To select the 4-quantum coherence pathway, the PFGs G_2 and G_3 were adjusted such that $G_3/G_2 = -g = -(\gamma_C + 3\gamma_H)/\gamma_P = -12.92$. During the INEPT transfer, CNOT gates, and the diffusion delays, the evolution of all un-necessary interactions were refocused by using π pulses selectively on methyl carbon. The spin-selective π pulse was realized using a strongly modulated RF sequence [42]. The results of the NOON state diffusion experiments are shown in Fig. 5.3c. Again a linear fit based on expression 5.3, with an effective gyromagnetic ratio $\gamma_{\text{eff}} = (\gamma_P + 9\gamma_H)$ lead to the diffusion constant of $D = (8.1 \pm 0.4)10^{-10}$ m^2 s^{-1}, which is close to the value obtained from the single quantum method. It can be seen that, in the NOON state method, the diffusion delay is reduced by a factor of 12.

5.4 Radio frequency inhomogeneity

Consider an ensemble of spin-1/2 nuclei with long relaxation time constants. The standard method for studying RFI involves a single, constant low-amplitude, on-resonant RF pulse of variable duration. The corresponding pulse sequence is shown in Fig. 5.4a. The intensity $s(\nu_0, t)$ of the obtained signal oscillates due to the varying transverse magnetization and decays mainly due to RFI. This oscillation is known as the 'Torrey oscillation' [139]. The Fourier transform $S(\nu_0, \nu)$ of the oscillation $s(\nu_0, t)$ leads to a distribution over the actual RF amplitudes ν. We can extract RFI distribution $p(\nu)$ by normalizing the positive real part of $S(\nu_0, \nu)$ to unit area. In typical NMR probes, one obtains an asymmetric Lorentzian distribution with a higher weight towards the amplitudes lower than the nominal value [42]. Such a profile can be modelled by an asymmetric Lorentzian

$$\begin{aligned} p(\nu) &= \frac{a\lambda_-^2}{(1-\frac{\nu}{\nu_0})^2+\lambda_-^2} \quad \text{if} \quad \nu < \nu_0, \quad \text{and,} \\ p(\nu) &= \frac{a\lambda_+^2}{(1-\frac{\nu}{\nu_0})^2+\lambda_+^2} \quad \text{if} \quad \nu \geq \nu_0 \end{aligned} \tag{5.6}$$

where $\lambda_\pm$ are the Lorentzian line-width parameters and a is the normalization constant. The main disadvantage of the single-quantum method is the requirement of a long RF pulse to capture artefact-free RFI profile. The duty cycle limit of the probe introduces a limitation on the highest amplitude at which RFI can be studied. In the following we describe the NOON state Torrey oscillation which is ultra-sensitive for incoherence and hence allows capturing RFI profile with a shorter RF pulse and at higher RF amplitudes.

5.4.1 Measurement of RFI via NOON states

In order to measure RFI while preserving the coherence order of NOON states, we utilize Z-nutation. The pulse sequence for the NOON state method is shown in Fig. 5.4b. A ϕ_z

pulse acting on a NOON state introduces a large relative phase shift:

$$\frac{1}{\sqrt{2}}(|00\cdots0\rangle + |11\cdots1\rangle) \xrightarrow{\phi_z^M} \tag{5.7}$$

$$\frac{1}{\sqrt{2}}(|00\cdots0\rangle + e^{(N-1)i\phi_z}|11\cdots1\rangle) \xrightarrow{CNOT}$$

$$\frac{1}{\sqrt{2}}(|0\rangle + e^{i(N-1)\phi_z}|1\rangle)|00\cdots0\rangle. \tag{5.8}$$

Therefore the resultant phase-shift of the control spectral line is $\phi_z^M = (N-1)\phi_z$. A ϕ_z^M pulse, on M-spins can be realized by $\left(\frac{\pi}{2}\right)_{-y}^M \phi_x^M \left(\frac{\pi}{2}\right)_y^M$, where $\phi_x^M = 2\pi(N-1)\nu_0\tau$ is the corresponding x-pulse of duration τ for a nominal RF amplitude ν_0. Ideally, in the absence of RFI, one should see a regular oscillatory behavior of this coherence with τ. In practice we see Torrey oscillation, i.e., decaying oscillations, due to the RFI during ϕ_x^M pulse.

5.4.2 Experimental characterization of RFI

The single-quantum Torrey oscillations were studied using a sample consisting of 600 µl of 99% D_2O. All the RFI experiments are carried out at 300 K on a 500 MHz NMR Bruker NMR spectrometer with QXI probe. The NOON Torrey oscillations were studied using the trimethylphosphite sample (Fig. 5.2a).

The single quantum Torrey oscillations were studied using the pulse sequence shown in Fig. 5.4a. A series of experiments were recorded by incrementing the duration of the on-resonant pulse with an amplitude of 1 kHz on ^{1}H channel of QXI probe. The τ-increments are set to 250 µs respectively, and a total of 256 transients were recorded. The asymmetry parameters ($\lambda_- = 0.018$, $\lambda_+ = 0.009$) are obtained by fitting the profile in expression 5.6 to the normalized real part $S(\nu_0, \nu)$ of the Fourier transform of Torrey oscillation. The asymmetry parameters $\lambda_\pm$ for NOON RFI experiments in the NOON state RFI experiments, can were extracted in similar way using the pulse-sequence Fig. 5.4b and the results are displayed in Fig. 5.5. Its evident from values of $\lambda_\pm$ that the RFI is some what stronger at higher amplitudes. For example, the asymmetry parameters at 9.4 kHz and 21 kHz are significantly larger than those at 5.4 kHz.

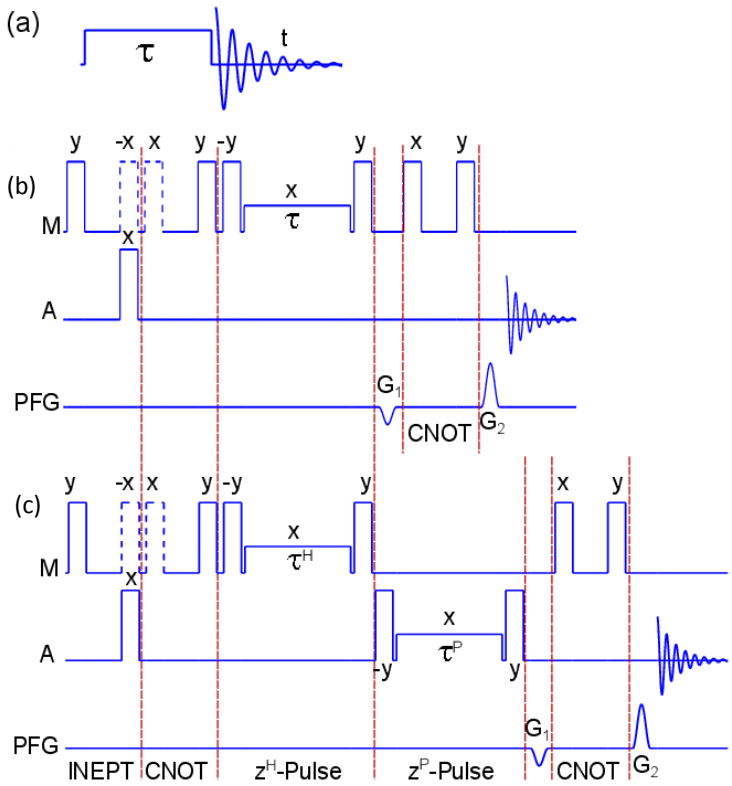

Figure 5.4: (a) Pulse sequence for single-quantum Torrey oscillation, (b) pulse sequence for NOON Torrey oscillation, and the RFI, (c) pulse sequence for measuring RFI correlation between ^{1}H and ^{31}P channels. In (b) and (c) except the variable duration (τ) pulses, all other pulses are 90°

5.4.3 Correlation between RFI of two channels

In a two-channel probe, the regions of high RF intensity of first channel may not correspond to regions of high RF intensity of the second. In other words, RFI profiles of the two channels may be spatially correlated. Such a correlation can easily be studied using a NOON state consisting of a collective coherence of heteronuclear species. The pulse diagram for the RFI-correlation study is shown in Fig. 5.4c. A ϕ_z^A pulse is introduced after the ϕ_z^M pulse, and the two pulses are independently incremented to obtain a 2D dataset $s(\nu^{M_9}, \nu^A)$. The Fourier transform along the two dimensions results in the frequency profile $S(\nu^{M_9}, \nu^A)$.

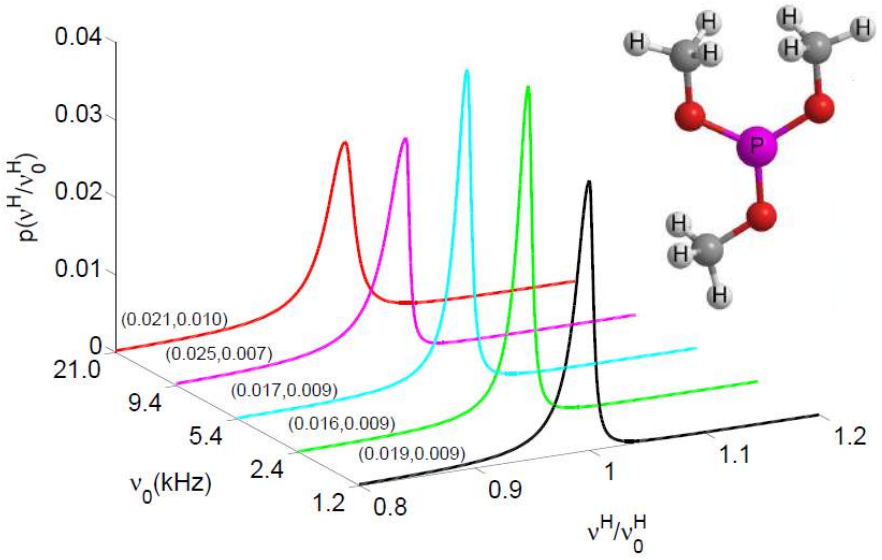

Figure 5.5: The RFI profiles at various nominal amplitudes obtained from NOON state experiments and corresponding values of asymmetry parameters (λ_-, λ_+).

We now model the RFI correlation using a 3D asymmetric Lorentzian:

$$p(\nu^H/\nu_0^H, \nu^P/\nu_0^P) = \frac{\lambda_0^2}{d^2(\nu^H, \nu^P) + \lambda_0^2}, \tag{5.9}$$

where $d(\nu^H, \nu^P)$ is the scaled distance of $\left(\frac{\nu^H}{\nu_0^H}, \frac{\nu^P}{\nu_0^P}\right)$ from the nominal point $(1, 1)$:

$$d^2(\nu^H, \nu^P) = \lambda_\pm^H \left(1 - \frac{\nu^H}{\nu_0^H}\right)^2 + \lambda_\pm^P \left(1 - \frac{\nu^P}{\nu_0^P}\right)^2. \tag{5.10}$$

Here $\lambda_\pm^H$ and $\lambda_\pm^P$ are the four asymmetry parameters on the four quadrants of ν^H - ν^P plane (Fig. 5.6b). These parameters together with λ_0 completely characterize the RFI correlation.

In the following, we describe experimental characterizations of the RFI correlation between ^{1}H and ^{31}P channels of an NMR probe. We used trimethylphosphite ($P(OCH_3)_3$ dissolved in DMSO-D6) for correlation experiments. The molecular properties of the sample are explained in subsec. 5.3.2. The 2D dataset was recorded by independently

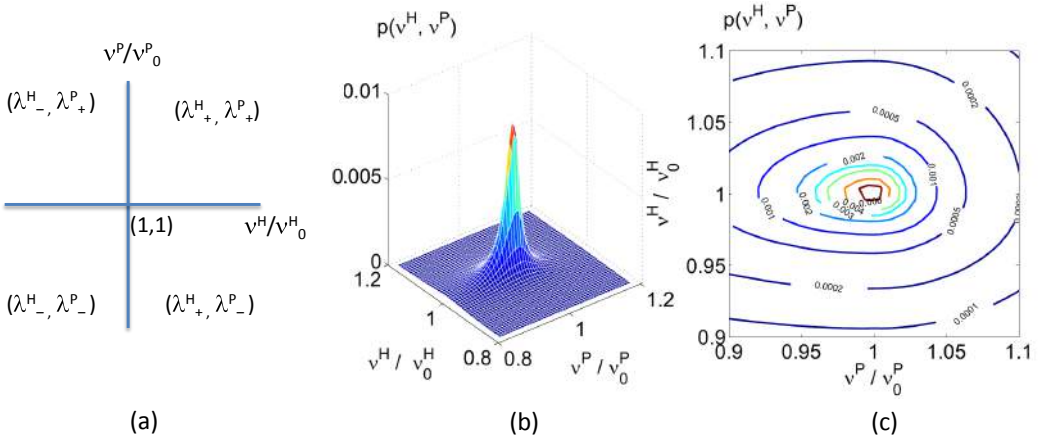

Figure 5.6: Characterization of RFI correlations between ^{1}H and ^{31}P channels of QXI probe.(a) The ν^H - ν^P plane, (b) the surface plot of the RFI profile $p(\nu^H, \nu^P)$, and (b) the contour plot of $p(\nu^H, \nu^P)$

.

incrementing the τ^H and τ^P pulses respectively by 11.1 µs and 50.0 µs. The nominal RF amplitudes in ^{1}H and ^{31}P channels were 2.4 kHz and 2.5 kHz respectively. A total of 128 data points in ^{1}H dimension and 96 data points in ^{31}P dimension were collected. The real positive part of the Fourier transform of the 2D Torrey oscillations $S(\nu^{H_9}, \nu^P)$ was obtained after a zero-fill to 256 points in each dimension. The asymmetric Lorentzian parameters $(\lambda_0, \lambda_\pm^{H/P})$ were obtained by fitting a model profile obtained by expression 5.9 to to the experimental profile $S_{1,9}$. $\{\lambda_0 = 0.005, \lambda_+^H = 0.114, \lambda_-^H = 0.226, \lambda_+^P = 0.095, \lambda_-^P = 0.028\}$. The corresponding RFI profile $p(\nu^H, \nu^P)$ is shown in Fig. 5.6b and its contour plot is shown in Fig. 5.6c. It can be observed that ^{31}P-channel has a wider RFI distribution than the ^{1}H-channel.

5.5 Conclusions

We described two applications of NOON states: (i) studying translational diffusion in liquids, and (ii) characterizing RF inhomogeneity of NMR probes.

We first described the experimental measurement of diffusion constant in a model system. Both single-quantum and the NOON-state experiments lead to identical values for the diffusion constant, but the errors were slightly larger in the latter case due to additional

complexities. However, the ultra-sensitivity of a NOON state to incoherence allowed an order of magnitude shorter diffusion delay, indicating the possible applications in studying slow diffusion. It might also be possible to combine the NOON state technique with the single scan 2D techniques to achieve ultra-fast diffusion measurements.

In the second part, we observed that the NOON state Torrey oscillations decay much faster than the single quantum Torrey oscillations allowing the characterization of RFI at higher RF amplitudes. Using this method, we have studied RFI of an NMR probe at different RF amplitudes and compared the results.

We then extended the NOON state method, using a 3D Lorentzian model, to characterize RFI correlations between two RF channels. Although the basic principle is general, the methods are particularly convenient with spin-systems having star-topology allowing parallel implementation of CNOT gates.

Such spin-systems can be found in many organic compounds and in biomolecules. The ultra-sensitivity of NOON states to phase encoding may also have potential applications in MRI.

Chapter 6

Dynamical Decoupling of Spin-Clusters using Solid State NMR

6.1 Introduction

The study of dynamics and control of quantum many body systems has renewed interest in the field of quantum information. While encoding information onto a quantum channel can potentially speed up certain computations and allow secure data transmission, the practical realization of these applications are hindered by the extreme sensitivity of the quantum channel to environmental noises. Systems based on nuclear spin-clusters is one among the various architectures being investigated to realize quantum channels. Several experimental demonstrations of quantum information processing (QIP) using solid-state nuclear magnetic resonance (SSNMR) have already been reported [111, 140–143]. By sophisticated control of spin-dynamics it is in principle possible to achieve a larger number of quantum bits (qubits) using SSNMR, because of the availability of large spin-clusters coupled mutually through long-range dipole-dipole interactions. However in such a spin-cluster, fluctuating local fields at the site of each spin induced by its environment leads to the decoherence of the encoded quantum information.

Due to the availability of large spin-clusters it is possible to prepare coherences of large quantum numbers by a widening network of correlated spins evolving under two-quantum average Hamiltonian [144, 145]. These higher order coherences are not directly observable as macroscopic magnetizations, but can be converted into obervable single quantum coherence (SQC) using a time-reversed two-quantum average Hamiltonian. This method, often known as a 'spin-counting experiment' has been used to study the evolution of coherences of large quantum numbers exceeding 4000 [146–148].

Under the standard Zeeman Hamiltonian any spin-coherence is a non-equilibrium state and decays via various relaxation processes, ultimately leading to the equilibrium longitudinal magnetization. It has long been discovered that the decay process of the spin

coherence can be prolonged by applying a series of spin flips at regular intervals of time. This sequence known as 'CPMG sequence', not only refocusses the effect of spectrometer inhomogeneities, but also reverses the phase evolution of the coherences under the random fluctuations, provided the spin flips are applied sufficiently frequent [149, 150]. Such a dynamical method for the suppression of decoherence of a qubit due its interaction with environment is often termed as 'dynamical decoupling' (DD) [151]. Recently Uhrig introduced a non-periodic spin-flip sequence which he proved theoretically to proivde optimal decoupling performance for dephasing spin-bath interactions [152]. CPMG and other similar periodic spin-flip sequences suppress spin-environment interaction to nth order using up to $O(2^n)$ pulses, while Uhrig dynamical decoupling (UDD) suppresses the same using only n pulses. In a high-frequency dominated bath with a sharp cutoff, UDD works well provided the frequency of the spin-flips exceeds the cutoff frequency [153–155]. On the other hand when the spectral density of the bath has a soft cutoff (such as a broad Gaussian or Lorentzian), the CPMG sequence was found to outperform the UDD sequence [156–163]. The original sequence for UDD is based the assumption of instantaneous spin-flips, which requires infinite bandwidth. Later on, Uhrig provided an improved sequence - 'realistic UDD' (RUDD) for practical implimentations with finite bandwidth [164].

Most of the theory and experiments of DD sequences are for single spin systems. Du et al have studied DD of electron spin coherence in solids [165] while Suter and coworkers have reported systematic experimental comparisons of various DD schemes on an ensemble of single spins in SSNMR [157, 163]. A few studies of DD on two-qubit systems have also been reported [166, 167]. Experimentally, Wang et. al. have studied DD on electron-nuclear spin pairs in a solid-state system [165], and Soumya et. al. have studied the performance of UDD an a two-qubit liquid-state NMR system [168].

We experimentally studied the performance of various DD schemes on an extended network of spin-1/2 nuclei forming a large spin cluster. In this chapter I report these studies. This chapter is organized as follows. In the next §I briefly describe the method of preparing and detecting multiple quantum coherences (MQC) in SSNMR. In §6.3 I summarize the construction of various DD sequences. The experimental details are described

in §6.4. Finally I conclude in §6.6.

6.2 Multiple Quantum SSNMR

The SSNMR Hamiltonian for a spin cluster with M spin-1/2 nuclei is

$$\mathcal{H}_{int} = \mathcal{H}_Z + \mathcal{H}_D, \tag{6.1}$$

where the Zeeman and the secular part of dipolar interaction are respectively,

$$\mathcal{H}_Z = \sum_{i=1}^{M} \omega_i I_z^i, \mathcal{H}_D = \sum_{i<j} D_{ij} \left[3I_z^i I_z^j - I^i \cdot I^j\right].$$

Here $\mathbf{I}^i$ and I_z^i are spin angular momentum operator and its z-component corresponding to the i^{th} spin, and w_i and D_{ij} are the chemical shift and the dipolar coupling constants. The equilibrium density matrix for the above Hamiltonian corresponds to the longitudinal magnetization expressed as $\sum_i I_z^i$. The density matrices for the longitudinal spin order can be expressed using product of longitudinal spin operators, eg. $I_z^1 I_z^2 \cdots$. The coherences are described by the product of transverse (or of transverse and longitudinal) spin operators, eg. $I_z^1 I_x^2 I_x^3 \cdots$. The transverse spin operators can also be expressed in terms of raising and lowering operators: $I_x = (I_+ + I_-)/2$ and $I_y = -i(I_+ - I_-)/2$. The difference between the total number of raising and lowering operators gives the quantum number n of a particular coherence. For example, operators $I_+^j I_-^k$, I_+^j, and $I_+^j I_+^k$ describe zero, single, and two-quantum coherences respectively. The pulse sequence for preparing and detecting MQC is shown in Fig. 6.1(a-b). The sequence Fig. 6.1a involves preparation of MQC, application of DD schemes, free-evolution (t_1), converting MQC into longitudinal spin order (mixing), destroying the residual coherences by transverse relaxation (t_R), followed by detection after converting the logitudinal spin order into SQC. The 8-pulse sequence in Fig. 6.1b corresponds to the two-quantum average Hamiltonian

$$\mathcal{H}_1 = \frac{D_{ij}}{2}\left(I_+^i I_+^j + I_-^i I_-^j\right), \tag{6.2}$$

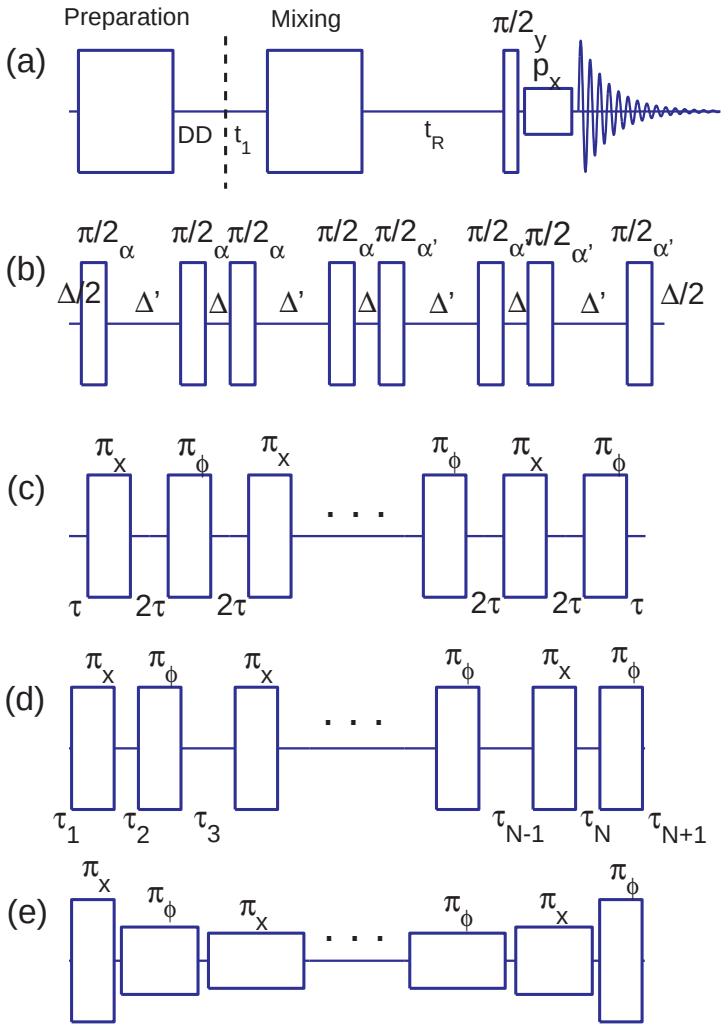

Figure 6.1: The experimental scheme (a) for studying the performance of DD on large spin-clusters and the 8-pulse sequence (b) implementing $\mathcal{H}_1(\alpha)$. In (b), $\Delta' = 2\Delta + \tau_{\pi/2}$, where $\tau_{\pi/2}$ is the duration of each $\pi/2$ pulse. The DD schemes are described in (c-e). The phase ϕ is set to x for CPMG, UDD, and RUDD schemes, while it is alternated between x and $-x$ for CPMGp, UDDp, and RUDDp.

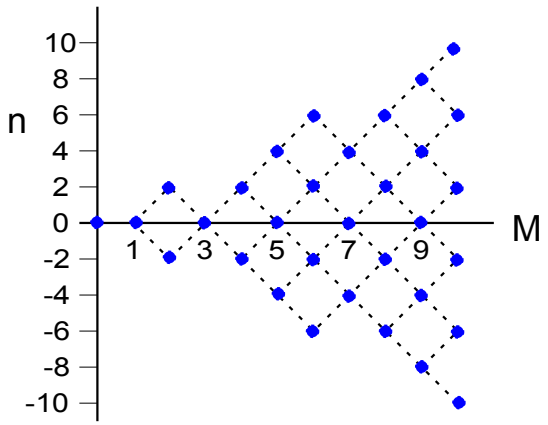

Figure 6.2: Possible quantum numbers (n) for M-spin cluster after excitation with several cycles of two-quantum average Hamiltonian ($\mathcal{H}_m$).

for $\alpha = 0$. Preparation and mixing parts involve m-cycles of the 8-pulse sequence $\mathcal{H}_m(\alpha)$ and $\mathcal{H}_m(0)$ [145]. The possible quantum numbers and the corresponding cluster size increases with the number of cycles. Only even quantum coherences are prepared as shown in Fig. 6.2. To separate the MQC, the relative phase α between the prepation and mixing is incremented in proportion to the evolution time t_1 (Fig. 6.1a). Spurious transverse coherences are suppressed by an extended delay t_R. The desired signal, stored as population information along z-axis, is detected with a $\pi/2_y$ pulse and a final purge pulse p_x is used to keep only the x-component.

6.3 DD schemes

In the following three different DD sequences and their phase variants are described. The performance of a particular sequence depends on the noise spectrum of the system. For example, CPMG generally performs better against a noise spectrum with a slow frequency cut-off, while UDD works better against the one with a sharp frequency cut-off.

6.3.1 CPMG and CPMGp

CPMG and CPMGp schemes involve periodic spin flips as shown in Figure 6.1c. In CPMG phase ϕ set to x. CPMGp scheme is obtained by alternating the phase ϕ between x and $-x$. CPMG and CPMGp have different performances depending on the initial states

[148]. The total duration of the N-pulse CPMG is $T = N(2\tau + \tau_\pi)$, where τ_π is the duration of the π pulse. The same parameters N and T are used to compare CPMG with the following schemes.

6.3.2 UDD and UDDp

The pulse distributions for UDD and UDDp schemes are shown in Figure 6.1d. Here the spin flips are symmetric but not periodic [152]. The j^{th} π pulse is applied at the time instant

$$t_j = T \sin^2\left[\frac{\pi j}{2N+2}\right], \tag{6.3}$$

where T is the total duration of the sequence and N is the total number of pulses. For a finite bandwidth case, with a π pulse of duration τ_π, the delays τ_j are given by $\tau_1 = \tau_{N+1} = t_1 - \tau_\pi/2$, $\tau_j = t_{j+1} - t_j - \tau_\pi$, for $2 \leq j \leq N$. Like in the previous scheme, UDD and UDDp are differed by the constant phase and the phase alternation in ϕ.

6.3.3 RUDD

In RUDD and RUDDp, both the delays and the pulse durations vary, but the overall sequence remains symmetric. The pulse durations are given by

$$\tau_\pi^j = T\left[\sin\left(\frac{\pi j}{N+1}\right)\sin\theta_p\right], \tag{6.4}$$

where T is total duration of the sequence and N is the number of pulses. Here θ_p is a constant and can be determined by the allowed bandwidth. We choosed $\tau_\pi^1 = \tau_\pi$, and calculated θ_p based on the minimum allowed pulse duration:

$$\sin\theta_p = \frac{\tau_\pi}{T\sin\left(\frac{\pi}{N+1}\right)}. \tag{6.5}$$

The amplitude a_j of j^{th} pulse is calibrated such that $2\pi a_j \tau_\pi^j = \pi$. Time instants of the center of each pulse is same as in equation (6.3). Using these time instants, the delays between

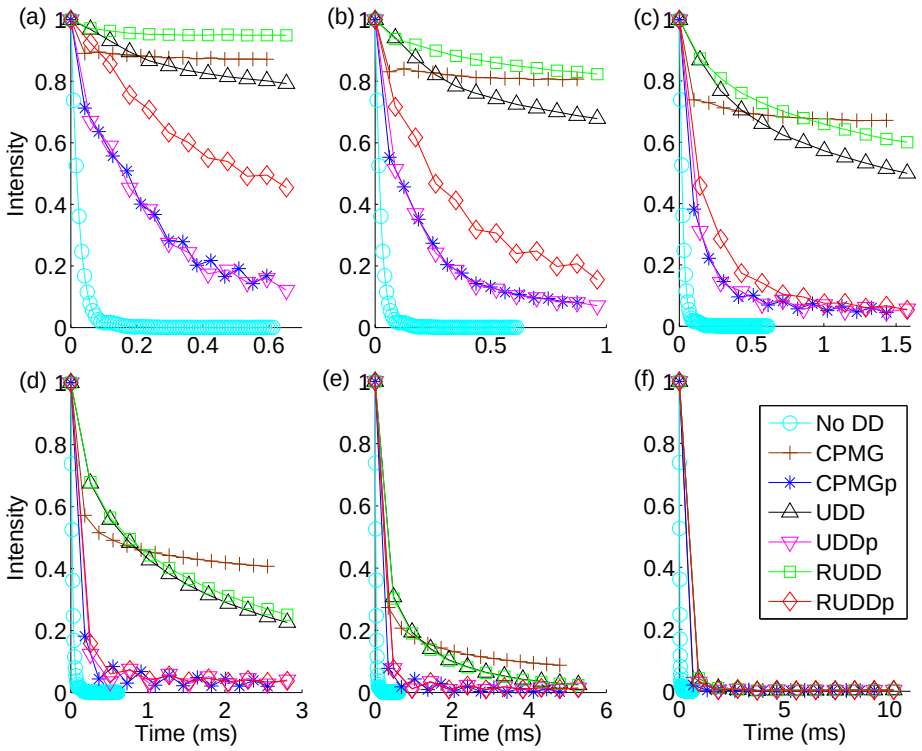

Figure 6.3: The performance of 7-pulse DD cycles to suppress decoherence measured as intensities of the preserved coherences. Here initial state is $\sum_i \sigma_{ix}$, where i is the proton spin index. The sub-plots correspond to various CPMG dealys: $\tau = 2$ μs (a), $\tau = 4$ μs (b), $\tau = 8$ μs (c), $\tau = 16$ μs (d), $\tau = 32$ μs (e), and $\tau = 64$ μs (f).

the pulses can be calculated as $\tau_1 = \tau_{N+1} = t_1 - \tau_\pi/2$, and $\tau_j = t_j - t_{j-1} - \tau_\pi^j/2 - \tau_\pi^{j-1}/2$ for $2 \leq j \leq N$. Like in the previous schemes, RUDD and RUDDp are differed by the constant phase and the phase alternation in ϕ.

6.4 Experiment

The sample consists of crystallites of powdered Hexamethylbenzene. At room temperature the entire molecule undergoes six fold hopping about the C_6 axis of benzene ring. Further the methyl group rapidly reorients about its C_3 axis. Due to these motions, the intramolecular dipolar interactions are averaged out. Intermolecular dipolar coupling is retained and each molecule acts as a point dipole. Under free precession (no DD), this sample has a spin-spin relaxation constant of about 25 μs and a spin-lattice relaxation constant of 1.7s. All the experiments are carried out on a Bruker 500 MHz spectrometer.

6.4.1 DD on SQC

First we describe the performance of various DD schemes on SQC. SQC was prepared by using an initial $(\pi/2)_y$ pulse on equilibrium longitudinal magnetization. As described in §6.3.1 and Fig. 6.1c, CPMG sequences were constructed by periodic distribution of π pulses in $\tau - \pi - \tau$ fashion. The minimum τ in our experiments was set to 2 μs owing to the duty cycle limitation of the probe coil. In our spectrometer the minimum duration of π pulse was found to be $\tau_\pi = 4.3$ μs. Under these experimental conditions, the allowed values of N for UDD and RUDD are 1 to 7. For $N \geq 8$, one obtains negative delays between the pulses. Therefore to study DD schemes for longer durations, we cycled these 7-pulse DD sequences. The 7-pulse CPMG has a total cycle time of $T(\tau) = 7(2\tau + \tau_\pi)$. The results of these experiments are shown in Fig. 6.3. The graphs correspond to $\tau = 2$ μs (a), $\tau = 4$ μs (b), $\tau = 8$ μs (c), $\tau = 16$ μs (d), $\tau = 32$ μs (e), and $\tau = 64$ μs (f). The corresponding $T(\tau)$ values are used to select the sampling points in no DD, as well as to construct other DD sequences. It is clear from these data that RUDD displays superior performance for shorter τ values, CPMG shows better performance while for longer τ values. We can also notice from these plots that the performance of RUDDp is better than CPMGp and UDDp which have almost same performance. UDD has better behavior than RUDDp, and for longer τ values UDD and RUDD have same behaviour. However, these performances in general may also be dependent on initial states [148].

6.4.2 DD on MQC

As described in §6.2 and Fig. 6.1(a-b), the scheme for studying DD on MQC involves preparation of MQC, evolution of MQC, followed by storing MQC onto longitudinal spin-orders. A delay $t_R = 5$ ms was introduced to destroy the residual transverse magnetization. The longitudinal spin order is then converted into SQC using a $(\pi/2)_y$ pulse, followed by a purge pulse p_x of duration 50 μs. A 180 degree phase alternation of the detection pulse, purge pulse, and the receiver is used to reduce artifacts arising from receiver ringing. For efficient generation of MQC five cycles of 8-pulse sequence shown in Fig. 6.1b was used in preparation and mixing periods, and the parameter Δ was optimized to 2 μs. In our ex-

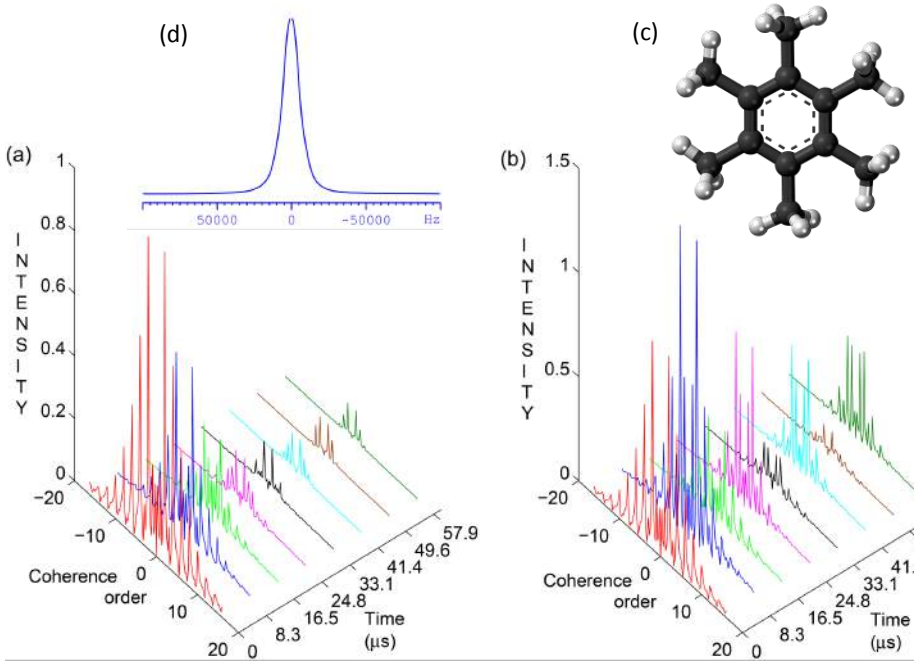

Figure 6.4: Multiple quantum spectra showing different coherence orders detected after inserting various delays (a) and RUDD sequences of same durations (b). Structure of Hexamethylbenzene(c). ^{1}H spectra of powder Hexamethylbenzene (d). The line width of the resonance peak is 12 kHZ.

periments the coherences of successive quantum number are separated by $\Delta\omega = 2\pi \times 200$ kHz In order to separate a maximum of $n_{\max}$ coherences, the relative phase α between the prepation and mixing is incremented by $\Delta\alpha = \pi/n_{\max}$. We have choosen $n_{\max} = 64$. The corresponding increment in the evolution period is given by $\Delta t_1 = \Delta\alpha/\Delta\omega$. The signal intensities of the spectrum corresponding to these increments after cosine transform display strong peaks at even multiples of $\Delta\omega$. Mean value of the signal intensities is made to zero to suppress strong zero-quantum peak. Fig. 6.4a displays these even MQCs detected after inserting various delays, and Fig. 6.4b displays those detected after applying RUDDp sequences of same durations. The first spectrum corresponding to no-delay is same in both cases, in which MQCs of order up to 24 can easily be observed. Other spectra in (b) were obtained by RUDDp sequences constructed with increasing number of pulses, i.e., $N = 1, 2, \cdots, 7$. Under no DD (Fig. 6.4a), the intensities decay monotonically with delays while under RUDDp (Fig. 6.4b) the dependence of intensities is oscillatory w.r.t. N. Similar behavior was earlier observed in a two-qubit liquid state NMR system [168]. The spectra in (b) at odd N clearly show better intensities compared to the corresponding spectra in (a). Comprasions of performance of different DD schemes for preserving MQCs of various orders are discribed in the following. The intensities of MQCs of even orders between 2 and 8 w.r.t. size of various DD schemes are plotted in Fig. 6.5. The first data point in each data set corresponds to no DD, and the rest correspond to different size of the DD sequence with $N = 1, 2, \cdots, 7$. As observed in Fig. 6.4b, we see the oscillatory behaviour of each MQC under various DD schemes. But all the DD schemes display an overall improvement w.r.t. no DD. However it can be noticed that RUDDp has significantly better performance than all other schemes, even for higher order coherences. Surprisingly, unlike the single-quantum case, where in RUDD displayed the best performance, in multiple-quantum case RUDDp is the best scheme.

The intensities of MQCs of even orders between 2 and 8 for different cycles of 7-pulse DD schemes are plotted in Fig. 6.6. The first data point in each case corresponds to no DD. The fast decay of magnetization under no DD allowed to detect intensities corresponding to a duration of only one cycle, while for RUDD and RUDDp, intensities up to 3 cycles could be detected.

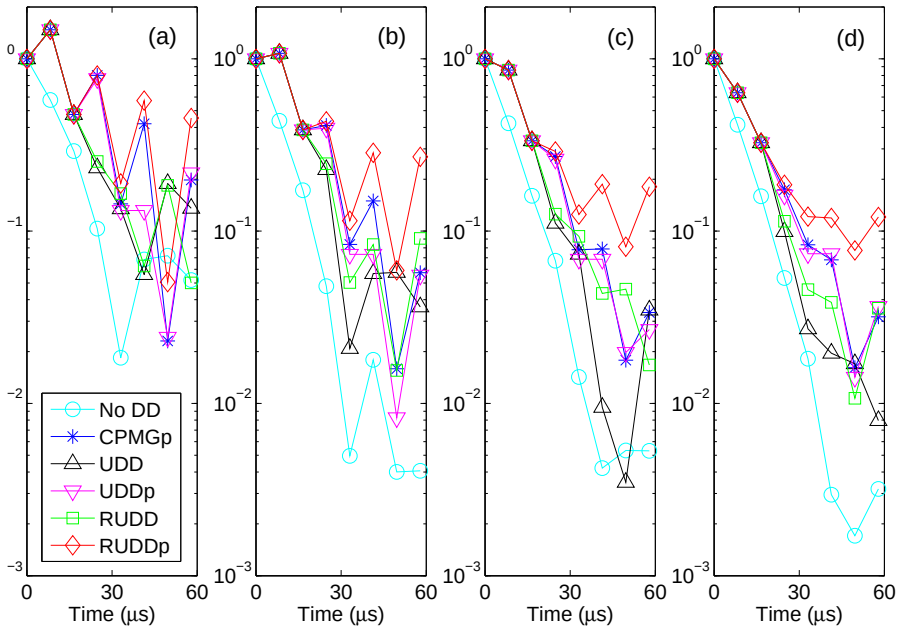

Figure 6.5: Performance of various DD schemes in preserving MQCs of order 2 (a), 4 (b), 6 (c), and 8 (d). Each data set has 8 points, in which the first point corresponds to no DD, and the rest correspond to different size of the DD sequence with $N = 1, 2, \cdots, 7$.

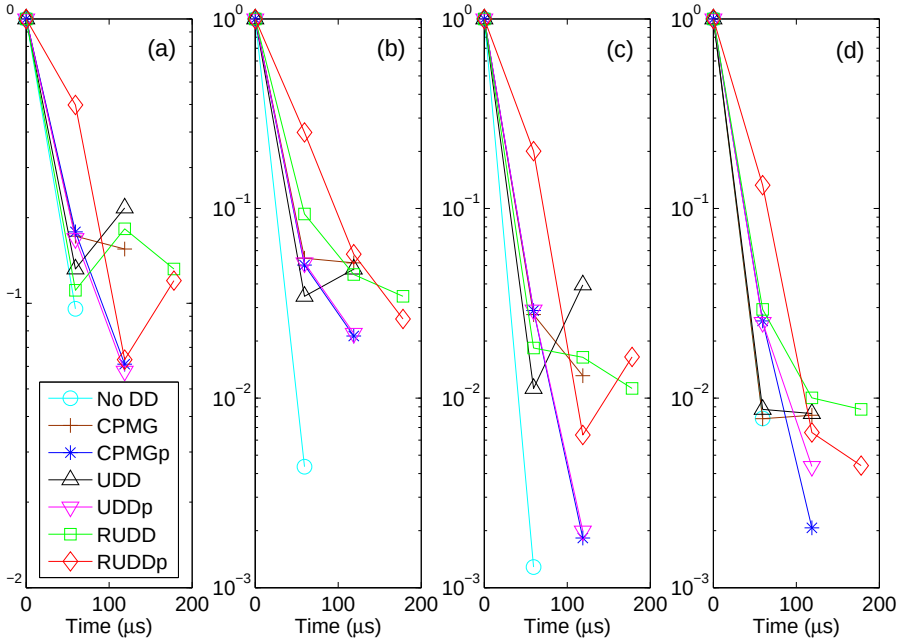

Figure 6.6: Performance of various DD schemes in preserving MQCs of order 2 (a), 4 (b), 6 (c), and 8 (d). The intensities were obtained from spectra detected after applying up to a maximum of 3 cycles of 7-pulse DD schemes.

6.5 Filter function analysis of various DD sequences

The most detrimental source of error in coherent evolution of quantum systems is the decoherence. The fluctuations in environmental couplings lead to random qubit errors and hence to loss of coherence. In following, I will revisit the effect of decoherence and dynamical decoupling quantitatively as described in [155]. Consider a qubit initially prepared in a superposition state,

$$|\psi\rangle = c_1|0\rangle + c_2|1\rangle. \tag{6.6}$$

Here c_1 and c_2 are probability amplitudes of state $|0\rangle$ and $|1\rangle$ respectively, such that $|c_1|^2 + |c_2|^2 = 1$. In a semiclassical picture, the average effect of the environment is captured by a random field $\beta(t)$, under which the qubit experiences a dephasing Hamiltonian $H = (\frac{\Omega}{2} + \beta(t))\sigma_z$. The Rabi frequency Ω can be dropped by transforming into a rotating frame. The state after the evolution under the Hamiltonian at time t is

$$|\psi(t)\rangle = c_1 e^{-i\int_0^t \beta(t)dt}|0\rangle + c_2 e^{i\int_0^t \beta(t)dt}|1\rangle. \tag{6.7}$$

Here $\int_0^t \beta(t)dt$ is the accumulated random phase by the qubit in time t. In the density matrix formulation the off diagonal terms in the density matrix

$$\rho(t) = |c_1|^2|0\rangle\langle 0| + |c_2|^2|1\rangle\langle 1| + c_1c_2^* e^{-2i\int_0^t \beta(t)dt}|0\rangle\langle 1| + c_2c_1^* e^{2i\int_0^t \beta(t)dt}|1\rangle\langle 0| \tag{6.8}$$

represent coherence and decays due to ensemble average. Typical source of dephasing involves error in experimental control, noise, and random parameters due to environment. In particular, magnetic field fluctuations in atomic systems [153], charge fluctuations in solid state charge qubits [169], and effective Overhauser field due to nuclear spins in semiconductors systems [170, 171].

Suppose we prepare our initial state $|\psi(0)\rangle$ along x direction, then the coherence at

time t is the ensemble average of expectation value i.e.,

$$W(\tau) = |\overline{\langle\sigma_x(\tau)\rangle}| = e^{-\chi(\tau)}, \tag{6.9}$$

where

$$\chi = \frac{2}{\pi}\int_0^\infty \frac{S_\beta(\omega)}{\omega^2}F_n(\omega\tau)d\omega. \tag{6.10}$$

In the above equation

$$S_\beta(\omega) = \int_{-\infty}^{\infty} e^{-i\omega t}(\beta(t+\tau)\beta(t))dt \tag{6.11}$$

is the power spectral density of environment and contains noise information in the frequency domain which is the Fourier transform of auto-correlation function of time domain noise term $\beta(t)$. It is often convenient to characterize noise in frequency domain using $S_\beta(\omega)$.

The term $F_n(\omega\tau)$ known as filter function captures the experimentally induced modulation to the coherence-decay $e^{-\chi(\tau)}$. A DD sequence introduces modulations to accumulated random phase such that every π pulse switches the phase between $\int_0^\infty \beta(t)dt$ and $-\int_0^\infty \beta(t)dt$. The DD sequence and corresponding modulation function $y_n(t)$ is shown in figure 1 of [155]. The convolution of $\beta(t)$ and $y_n(t)$ provides desired noise suppression. The Fourier transform of this convolution provides relevant spectral information. Filter function form in Fourier domain is

$$F_n(\omega\tau) = \left|1 + (-1)^{n+1}e^{i\omega\tau'} + 2\sum_{j=1}^{n}(-1)^j e^{i\delta_j\omega\tau'}\cos\left(\frac{\omega\tau_\pi}{2}\right)\right|^2 \tag{6.12}$$

Here τ' is the total time of the pulse sequence, $\delta_j\tau'$ and τ_π are respectively the time instant and the duration of the j^{th} π pulse. From the eqn. 6.9 it is evident that minimum value of $F_n(\omega\tau)$ leads to minimum decay χ and hence maximum coherence W. The filter function takes values between 0 and 1. For free evolution case, filter function $F_n(\omega\tau)$ is 1 and for

perfect refocusing it is zero. Filter function analysis using eqn. 6.10 and 6.12 provides a way to examine performance of various DD sequences. The minimum area under the filter function for a given DD leads to maximum coherence further one may also design an optimal DD sequence for a given power spectral density by minimizing $F_n(\omega\tau)$. Here we compare performance of DD sequences used in above experiments via filter function analysis. Results of the analysis are shown in Fig. 6.7 and in Fig. 6.8. Figure 6.8 shows plots of $\frac{F_n(\omega\tau)}{\omega^2}$ versus ω for different number of pulses ranging from 3-10. In each subplot, the filter function for RUDD sequence has lesser area than for corresponding CPMG and UDD sequences. The π pulse durations and delays used for calculating $F_n(\omega\tau)$ are $\tau = 2\mu s$ and $\tau_\pi = 4.27\mu s$, same as in our experiments. Fig. 6.7 shows area under the function $\frac{F_n(\omega\tau)}{\omega^2}$ for CPMG, UDD, and RUDD sequences. Clearly, in the case of RUDD sequence, the area under the curve is less than other sequences. One may also see typical even-odd behavior of RUDD sequence supporting our experimental results.

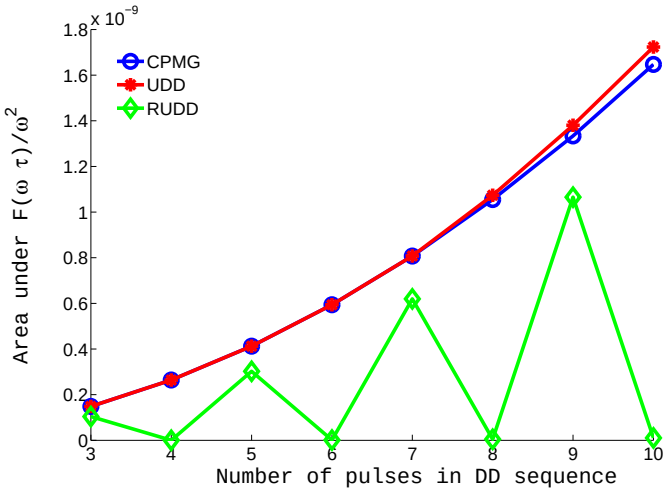

Figure 6.7: Filter function analysis (FF) of various DD sequences. Each point in the plot corresponds to the area under $\frac{F_n(\omega\tau)}{\omega^2}$ for respective sequence of given block size.

6.6 Conclusions

We studied the performance of various DD schemes on nuclear spins with long-range interactions using a solid state NMR system. First applied these DD schemes on a single

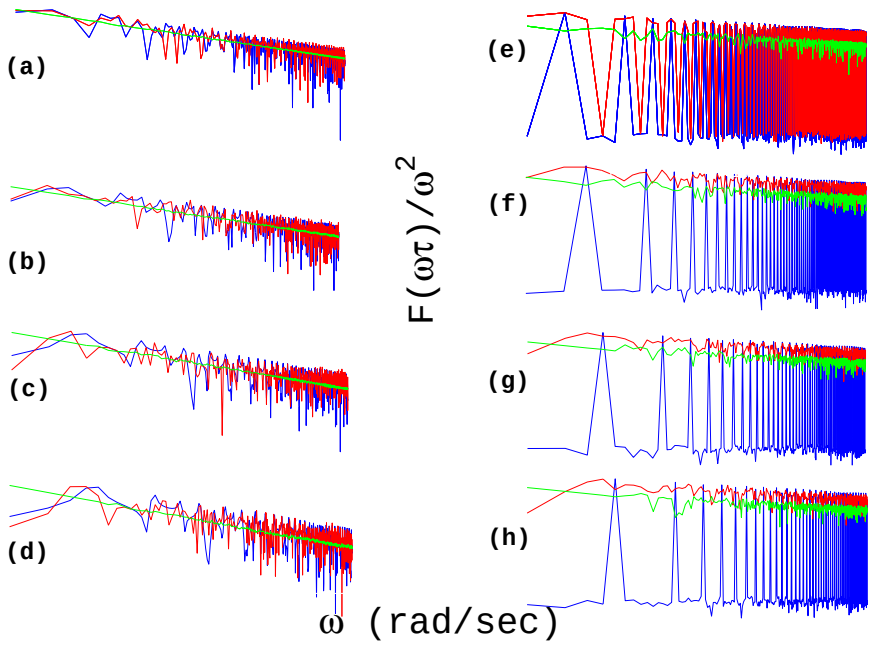

Figure 6.8: Plot shows $\frac{F(\omega\tau)}{\omega^2}$ versus ω for various DD sequences (CPMG, UDD, RUDD). The subplots (a) to (h) respectively correspond to the total number of π pulses ranging from 3 to 10.

quantum coherence. The experiments were carried out for different number of π pulses and for different delays between them. The results clearly show that all the DD schemes are able to preserve the single quantum coherence for longer durations of time compared to no DD. However, for small delays between the π pulses, RUDD showed the best performance. For longer dealys between the π pulses, CPMG was better.

Then we prepared MQCs of even orders using multiple cycles of the well known 8-pulse sequence implementing a two-quantum average Hamiltonian. The MQCs so prepared could be detected using standard spin-counting experiment. Various DD schemes were inserted after the preparation of MQCs. We studied the performance of various DD sequences of different sizes. The intensity behaviour under all the DD sequences were oscillatory, but they showed an overall improvement over no DD. However, RUDDp sequence showed the best performance over all other sequences. The superior performance of RUDD sequence over other DD sequences is attributed to lower filter function area of RUDD than others.

Bibliography

[1] A. R. Usha Devi, H. S. Karthik, Sudha, and A. K. Rajagopal. Macrorealism from entropic leggett-garg inequalities. *Phys. Rev. A*, 87:052103, May 2013.

[2] H. S. Karthik, Hemant Katiyar, Abhishek Shukla, T. S. Mahesh, A. R. Usha Devi, and A. K. Rajagopal. Inversion of moments to retrieve joint probabilities in quantum sequential measurements. *Phys. Rev. A*, 87:052118, May 2013.

[3] Claude Elwood Shannon. A mathematical theory of communication. *ACM SIGMOBILE Mobile Computing and Communications Review*, 5(1):3–55, 2001.

[4] Nielsen and Isaac L Chuang. *Quantum computation and quantum information*. Cambridge university press, 2010.

[5] Thomas M Cover and Joy A Thomas. *Elements of information theory*. John Wiley & Sons, 2012.

[6] Alexander Semenovich Holevo. Bounds for the quantity of information transmitted by a quantum communication channel. *Problemy Peredachi Informatsii*, 9(3):3–11, 1973.

[7] Charles H Bennett. Logical reversibility of computation. *IBM journal of Research and Development*, 17(6):525–532, 1973.

[8] R. P. Poplavskii. Termodinamicheskie modeli informatsionnykh protsessov. *Uspekhi Fizicheskikh Nauk*, 115(3):465–501, 1975.

[9] Paul Benioff. The computer as a physical system: A microscopic quantum mechanical hamiltonian model of computers as represented by turing machines. *Journal of Statistical Physics*, 22(5):563–591, 1980.

[10] Paul Benioff. Quantum mechanical models of turing machines that dissipate no energy. *Physical Review Letters*, 48(23):1581, 1982.

[11] Roman S Ingarden. Quantum information theory. *Reports on Mathematical Physics*, 10(1):43–72, 1976.

[12] Yu I Manin. Computable and non-computable. *Sov. Radio*, pages 13–15, 1980.

[13] Richard P Feynman. Simulating physics with computers. *International journal of theoretical physics*, 21(6):467–488, 1982.

[14] Charles H Bennett, Gilles Brassard, Seth Breidbart, and Stephen Wiesner. Quantum cryptography, or unforgeable subway tokens. In *Advances in Cryptology*, pages 267–275. Springer, 1983.

[15] Artur K Ekert. Quantum cryptography based on bell's theorem. *Physical review letters*, 67(6):661, 1991.

[16] Peter W Shor. Polynomial-time algorithms for prime factorization and discrete logarithms on a quantum computer.(english summary).

[17] Peter W Shor. Scheme for reducing decoherence in quantum computer memory. *Physical review A*, 52(4):R2493, 1995.

[18] Andrew M Steane. Error correcting codes in quantum theory. *Physical Review Letters*, 77(5):793, 1996.

[19] Lov K Grover. A fast quantum mechanical algorithm for database search. In *Proceedings of the twenty-eighth annual ACM symposium on Theory of computing*, pages 212–219. ACM, 1996.

[20] Lov K Grover. Quantum mechanics helps in searching for a needle in a haystack. *Physical review letters*, 79(2):325, 1997.

[21] Daniel R Simon. On the power of quantum computation. *SIAM journal on computing*, 26(5):1474–1483, 1997.

[22] David P DiVincenzo. Topics in quantum computers. In *Mesoscopic electron transport*, pages 657–677. Springer, 1997.

[23] Jun John Sakurai and Jim Napolitano. *Modern quantum mechanics*. Addison-Wesley, 2011.

[24] John Preskill. Lecture notes for physics 229: Quantum information and computation. *California Institute of Technology*, 1998.

[25] Carl W Helstrom. Quantum detection and estimation theory, mathematics in science and engineering. 1976.

[26] Soumya Singha Roy. Nuclear spins as quantum testbeds: Singlet states, quantum correlations, and delayed-choice experiments. *arXiv preprint arXiv:1210.7522*, 2012.

[27] C. Monroe, D. M. Meekhof, B. E. King, W. M. Itano, and D. J. Wineland. Demonstration of a fundamental quantum logic gate. *Phys. Rev. Lett.*, 75:4714–4717, Dec 1995.

[28] Walther Gerlach and Otto Stern. Das magnetische moment des silberatoms. *Zeitschrift für Physik A Hadrons and Nuclei*, 9(1):353–355, 1922.

[29] A Abragam. The principles of nuclear magnetism, 1961. *Oxford: University Press*, 119:120, 1998.

[30] II Rabi, S Millman, P Kusch, and JR Zacharias. The molecular beam resonance method for measuring nuclear magnetic moments. the magnetic moments of li 6 3, li 7 3 and f 19 9. *Physical review*, 55(6):526, 1939.

[31] E. M. Purcell, H. C. Torrey, and R. V. Pound. Resonance absorption by nuclear magnetic moments in a solid. *Phys. Rev.*, 69:37–38, Jan 1946.

[32] Felix Bloch. Nuclear induction. *Physical review*, 70(7-8):460, 1946.

[33] Ulrich Haberlen. *High resolution NMR in solids*. Acadmic press, 1976.

[34] John Cavanagh, Wayne J Fairbrother, Arthur G Palmer III, and Nicholas J Skelton. *Protein NMR spectroscopy: principles and practice*. Academic Press, 1995.

[35] Malcolm H Levitt. *Spin dynamics: basics of nuclear magnetic resonance*. John Wiley & Sons, 2001.

[36] Ulrich Haberlen. *High resolution NMR in solids*. Acadmic press, 1976.

[37] F. Bloch and A. Siegert. Magnetic resonance for nonrotating fields. *Phys. Rev.*, 57:522–527, Mar 1940.

[38] David G Cory, A. F. Fahmy, and T. F. Havel. Ensemble quantum computing by nmr spectroscopy. *Proc. Natl. Acad. Sci. USA*, 94:1634, 1997.

[39] Isaac L Chuang, Neil Gershenfeld, Mark G Kubinec, and Debbie W Leung. Bulk quantum computation with nuclear magnetic resonance: theory and experiment. *Proceedings of the Royal Society of London. Series A: Mathematical, Physical and Engineering Sciences*, 454(1969):447–467, 1998.

[40] C Negrevergne, TS Mahesh, CA Ryan, M Ditty, F Cyr-Racine, W Power, N Boulant, T Havel, DG Cory, and R Laflamme. Benchmarking quantum control methods on a 12-qubit system. *Physical Review Letters*, 96(17):170501, 2006.

[41] Jonathan A Jones, RH Hansen, and Michael Mosca. Quantum logic gates and nuclear magnetic resonance pulse sequences. *Journal of Magnetic Resonance*, 135(2):353–360, 1998.

[42] Marco A Pravia, Nicolas Boulant, Joseph Emerson, Amro Farid, Evan M Fortunato, Timothy F Havel, R Martinez, and David G Cory. Robust control of quantum information. *The Journal of chemical physics*, 119(19):9993–10001, 2003.

[43] Navin Khaneja, Timo Reiss, Cindie Kehlet, Thomas Schulte-Herbrüggen, and Steffen J Glaser. Optimal control of coupled spin dynamics: design of nmr pulse sequences by gradient ascent algorithms. *Journal of Magnetic Resonance*, 172(2):296–305, 2005.

[44] Henry O Everitt. *Experimental aspects of quantum computing*. Springer, 2005.

[45] M. G. Kubinec I. L. Chuang, N. Gershenfeld and D. W. Leung. Bulk quantum computation with nuclear magnetic resonance:theory and experiment. *Proc. R. Soc. Lond.,Ser A*, 454(2):447, 1998.

[46] Debbie Leung, Lieven Vandersypen, Xinlan Zhou, Mark Sherwood, Constantino Yannoni, Mark Kubinec, and Isaac Chuang. Experimental realization of a two-bit phase damping quantum code. *Physical Review A*, 60(3):1924, 1999.

[47] Ranabir Das, T. S. Mahesh, and Anil Kumar. Efficient quantum-state tomography for quantum-information processing using a two-dimensional fourier-transform technique. *Phys. Rev. A*, 67:062304, Jun 2003.

[48] A. E. Allahverdyan, R. Balian, and Th. M. Nieuwenhuizen. Determining a quantum state by means of a single apparatus. *Phys. Rev. Lett.*, 92:120402, Mar 2004.

[49] Xinhua Peng, Jiangfeng Du, and Dieter Suter. Measuring complete quantum states with a single observable. *Phys. Rev. A*, 76:042117, Oct 2007.

[50] Yafei Yu, Hua Wen, Hua Li, and Xinhua Peng. Determining an unknown state of a high-dimensional quantum system with a single, factorized observable. *Phys. Rev. A*, 83:032318, Mar 2011.

[51] Soumya Singha Roy and T.S. Mahesh. Density matrix tomography of singlet states. *Journal of Magnetic Resonance*, 206(1):127 – 133, 2010.

[52] Lloyd N Trefethen and David Bau III. *Numerical linear algebra*, volume 50. Siam, 1997.

[53] Ronald Y Dong. *Nuclear magnetic resonance of liquid crystals*. Springer, 1997.

[54] I. L. Chuang and M. A. Nielsen. Prescription for experimental determination of the dynamics of a quantum black box. *Journal of Modern Optics*, 44(11-12):2455–2467, 1997.

[55] J. F. Poyatos, J. I. Cirac, and P. Zoller. Complete characterization of a quantum process: The two-bit quantum gate. *Phys. Rev. Lett.*, 78:390–393, Jan 1997.

[56] Andrew M. Childs, Isaac L. Chuang, and Debbie W. Leung. Realization of quantum process tomography in nmr. *Phys. Rev. A*, 64:012314, Jun 2001.

[57] Yaakov S. Weinstein, Timothy F. Havel, Joseph Emerson, Nicolas Boulant, Marcos Saraceno, Seth Lloyd, and David G. Cory. Quantum process tomography of the quantum fourier transform. *The Journal of Chemical Physics*, 121:6117, 2004.

[58] Francesco De Martini, Andrea Mazzei, Marco Ricci, and Giacomo Mauro D'Ariano. Exploiting quantum parallelism of entanglement for a complete experimental quantum characterization of a single-qubit device. *Phys. Rev. A*, 67:062307, Jun 2003.

[59] J. B. Altepeter, D. Branning, E. Jeffrey, T. C. Wei, P. G. Kwiat, R. T. Thew, J. L. O'Brien, M. A. Nielsen, and A. G. White. Ancilla-assisted quantum process tomography. *Phys. Rev. Lett.*, 90:193601, May 2003.

[60] J. L. O'Brien, G. J. Pryde, A. Gilchrist, D. F. V. James, N. K. Langford, T. C. Ralph, and A. G. White. Quantum process tomography of a controlled-not gate. *Phys. Rev. Lett.*, 93:080502, Aug 2004.

[61] M. W. Mitchell, C. W. Ellenor, S. Schneider, and A. M. Steinberg. Diagnosis, prescription, and prognosis of a bell-state filter by quantum process tomography. *Phys. Rev. Lett.*, 91:120402, Sep 2003.

[62] M. Riebe, K. Kim, P. Schindler, T. Monz, P. O. Schmidt, T. K. Körber, W. Hänsel, H. Häffner, C. F. Roos, and R. Blatt. Process tomography of ion trap quantum gates. *Phys. Rev. Lett.*, 97:220407, Dec 2006.

[63] D. Hanneke, J. P. Home, J. D. Jost, J. M. Amini, D. Leibfried, and D. J. Wineland. Realization of a programmable two-qubit quantum processor. *Nature Phys.*, 6:13, Jan 2010.

[64] M. Neeley, M. Ansmann, R. C. Bialczak, M. Hofheinz, N. Katz, E. Lucero, A. O/'Connell, H. Wang, A. N. Cleland, and John M. Martinis. Process tomography of quantum memory in a josephson-phase qubit coupled to a two-level state. *Nature Phys.*, 4:523, Jan 2008.

[65] J. M. Chow, J. M. Gambetta, L. Tornberg, Jens Koch, Lev S. Bishop, A. A. Houck, B. R. Johnson, L. Frunzio, S. M. Girvin, and R. J. Schoelkopf. Randomized benchmarking and process tomography for gate errors in a solid-state qubit. *Phys. Rev. Lett.*, 102:090502, Mar 2009.

[66] R. C. Bialczak, M. Ansmann, M. Hofheinz, E. Lucero, M. Neeley, A. D. O/'Connell, D. Sank, H. Wang, J. Wenner, M. Steffen, and J. M. Cleland, A. N.and Martinis. Quantum process tomography of a universal entangling gate implemented with josephson phase qubits. *Nature Phys.*, 6:409, Jun 2010.

[67] T. Yamamoto, M. Neeley, E. Lucero, R. C. Bialczak, J. Kelly, M. Lenander, Matteo Mariantoni, A. D. O'Connell, D. Sank, H. Wang, M. Weides, J. Wenner, Y. Yin, A. N. Cleland, and John M. Martinis. Quantum process tomography of two-qubit controlled-z and controlled-not gates using superconducting phase qubits. *Phys. Rev. B*, 82:184515, Nov 2010.

[68] Jerry M. Chow, A. D. Córcoles, Jay M. Gambetta, Chad Rigetti, B. R. Johnson, John A. Smolin, J. R. Rozen, George A. Keefe, Mary B. Rothwell, Mark B. Ketchen, and M. Steffen. Simple all-microwave entangling gate for fixed-frequency superconducting qubits. *Phys. Rev. Lett.*, 107:080502, Aug 2011.

[69] A. Dewes, F. R. Ong, V. Schmitt, R. Lauro, N. Boulant, P. Bertet, D. Vion, and D. Esteve. Characterization of a two-transmon processor with individual single-shot qubit readout. *Phys. Rev. Lett.*, 108:057002, Feb 2012.

[70] Jingfu Zhang, Alexandre M. Souza, Frederico Dias Brandao, and Dieter Suter. Protected quantum computing: Interleaving gate operations with dynamical decoupling sequences. *Phys. Rev. Lett.*, 112:050502, Feb 2014.

[71] A. Shabani, R. L. Kosut, M. Mohseni, H. Rabitz, M. A. Broome, M. P. Almeida, A. Fedrizzi, and A. G. White. Efficient measurement of quantum dynamics via compressive sensing. *Phys. Rev. Lett.*, 106:100401, Mar 2011.

[72] Z. Wu, S. Li, W. Zheng, X. Peng, and M. Feng. Experimental demonstration of simplified quantum process tomography. *The Journal of Chemical Physics*, 138:024318, 2013.

[73] A Mazzei, M Ricci, F De Martini, and GM D'Ariano. Pauli tomography: complete characterization of a single qubit device. *Fortschritte der Physik*, 51:342–348, 2003.

[74] Giacomo Mauro D'Ariano and Paoloplacido Lo Presti. Imprinting complete information about a quantum channel on its output state. *Phys. Rev. Lett.*, 91:047902, Jul 2003.

[75] Abhishek Shukla, K. Rama Koteswara Rao, and T. S. Mahesh. Ancilla-assisted quantum state tomography in multiqubit registers. *Phys. Rev. A*, 87:062317, Jun 2013.

[76] Charles H. Bennett, Gilles Brassard, Sandu Popescu, Benjamin Schumacher, John A. Smolin, and William K. Wootters. Purification of noisy entanglement and faithful teleportation via noisy channels. *Phys. Rev. Lett.*, 76:722–725, Jan 1996.

[77] Charles H. Bennett, David P. DiVincenzo, John A. Smolin, and William K. Wootters. Mixed-state entanglement and quantum error correction. *Phys. Rev. A*, 54:3824–3851, Nov 1996.

[78] Joseph Emerson, Robert Alicki, and Karol Życzkowski. Scalable noise estimation with random unitary operators. *J. Opt. B: Quantum Semiclass. Opt.*, 7:S347–S352, Oct 2005.

[79] J. Emerson, M. Silva, O. Moussa, C. Ryan, M. Laforest, J. Baugh, David G. Cory, and R. Laflamme. Symmetrized characterization of noisy quantum processes. *Science*, 317(5846):1893, September 2007.

[80] M. Silva, E. Magesan, D. W. Kribs, and J. Emerson. Scalable protocol for identification of correctable codes. *Phys. Rev. A*, 78:012347, Jul 2008.

[81] Cecilia C. López, Ariel Bendersky, Juan Pablo Paz, and David G. Cory. Progress toward scalable tomography of quantum maps using twirling-based methods and information hierarchies. *Phys. Rev. A*, 81:062113, Jun 2010.

[82] Christoph Dankert, Richard Cleve, Joseph Emerson, and Etera Livine. Exact and approximate unitary 2-designs and their application to fidelity estimation. *Phys. Rev. A*, 80:012304, Jul 2009.

[83] Osama Moussa, Marcus P. da Silva, Colm A. Ryan, and Raymond Laflamme. Practical experimental certification of computational quantum gates using a twirling procedure. *Phys. Rev. Lett.*, 109:070504, Aug 2012.

[84] M. S. Anwar, L. Xiao, A. J. Short, J. A. Jones, D. Blazina, S. B. Duckett, and H. A. Carteret. Practical implementations of twirl operations. *Phys. Rev. A*, 71:032327, Mar 2005.

[85] Hengyan Wang, Wenqiang Zheng, Yafei Yu, Min Jiang, Xinhua Peng, and Jiangfeng Du. Determining an n-qubit state by a single apparatus through a pairwise interaction. *Physical Review A*, 89(3):032103, 2014.

[86] Agustin Palacios-Laloy, François Mallet, François Nguyen, Patrice Bertet, Denis Vion, Daniel Esteve, and Alexander N Korotkov. Experimental violation of a bell/'s inequality in time with weak measurement. *Nature Physics*, 6(6):442–447, 2010.

[87] ME Goggin, MP Almeida, Marco Barbieri, BP Lanyon, JL O'Brien, AG White, and GJ Pryde. Violation of the leggett–garg inequality with weak measurements of photons. *Proceedings of the National Academy of Sciences*, 108(4):1256–1261, 2011.

[88] J. Dressel, C. J. Broadbent, J. C. Howell, and A. N. Jordan. Experimental violation of two-party leggett-garg inequalities with semiweak measurements. *Phys. Rev. Lett.*, 106:040402, Jan 2011.

[89] Vikram Athalye, Soumya Singha Roy, and T. S. Mahesh. Investigation of the leggett-garg inequality for precessing nuclear spins. *Phys. Rev. Lett.*, 107:130402, Sep 2011.

[90] George C Knee, Stephanie Simmons, Erik M Gauger, John JL Morton, Helge Riemann, Nikolai V Abrosimov, Peter Becker, Hans-Joachim Pohl, Kohei M Itoh, Mike LW Thewalt, et al. Violation of a leggett-garg inequality with ideal non-invasive measurements. *Nature communications*, 3:606, 2012.

[91] Albert Einstein, Boris Podolsky, and Nathan Rosen. Can quantum-mechanical description of physical reality be considered complete? *Physical review*, 47(10):777, 1935.

[92] John S Bell et al. On the einstein-podolsky-rosen paradox. *Physics*, 1(3):195–200, 1964.

[93] E. Specker Simon Kochen. The problem of hidden variables in quantum mechanics. *Indiana Univ. Math. J.*, 17:59–87, 1968.

[94] JOHN S. BELL. On the problem of hidden variables in quantum mechanics. *Rev. Mod. Phys.*, 38:447–452, Jul 1966.

[95] A. J. Leggett and Anupam Garg. Quantum mechanics versus macroscopic realism: Is the flux there when nobody looks? *Phys. Rev. Lett.*, 54:857–860, Mar 1985.

[96] Neill Lambert, Robert Johansson, and Franco Nori. Macrorealism inequality for optoelectromechanical systems. *Phys. Rev. B*, 84:245421, Dec 2011.

[97] AM Souza, IS Oliveira, and RS Sarthour. A scattering quantum circuit for measuring bell's time inequality: a nuclear magnetic resonance demonstration using maximally mixed states. *New Journal of Physics*, 13(5):053023, 2011.

[98] Clive Emary. Leggett-garg inequalities for the statistics of electron transport. *Phys. Rev. B*, 86:085418, Aug 2012.

[99] Yutaro Suzuki, Masataka Iinuma, and Holger F Hofmann. Violation of leggett–garg inequalities in quantum measurements with variable resolution and back-action. *New Journal of Physics*, 14(10):103022, 2012.

[100] Sun Yong-Nan, Zou Yang, Ge Rong-Chun, Tang Jian-Shun, and Li Chuan-Feng. Violation of leggett—garg inequalities in single quantum dots. *Chinese Physics Letters*, 29(12):120302, 2012.

[101] Zong-Quan Zhou, Susana F Huelga, Chuan-Feng Li, and Guang-Can Guo. Experimental detection of quantum coherent evolution through the violation of leggett-garg inequalities. *arXiv preprint arXiv:1209.2176*, 2012.

[102] Samuel L. Braunstein and Carlton M. Caves. Information-theoretic bell inequalities. *Phys. Rev. Lett.*, 61:662–665, Aug 1988.

[103] Rafael Chaves and Tobias Fritz. Entropic approach to local realism and noncontextuality. *Phys. Rev. A*, 85:032113, Mar 2012.

[104] P. Kurzyński, R. Ramanathan, and D. Kaszlikowski. Entropic test of quantum contextuality. *Phys. Rev. Lett.*, 109:020404, Jul 2012.

[105] P. Kurzyński, R. Ramanathan, and D. Kaszlikowski. Entropic test of quantum contextuality. *Phys. Rev. Lett.*, 109:020404, Jul 2012.

[106] T. S. Mahesh and Dieter Suter. Quantum-information processing using strongly dipolar coupled nuclear spins. *Phys. Rev. A*, 74:062312, Dec 2006.

[107] J A Shohat and J D Tamarkin. *The Problem of Moments*. American Mathematical Society, New York, 1943.

[108] N I Akhiezer. *The classical moment problem*. Hafner Publishing Co., New York, 1965.

[109] Albert N Shiryaev. *Probability*. Springer-Verlag, New York,, 1996.

[110] Hemant Katiyar, Abhishek Shukla, Rama Koteswara Rao, and T. S. Mahesh. Violation of entropic leggett-garg inequality in nuclear spins. 2012.

[111] Osama Moussa, Colm A. Ryan, David G. Cory, and Raymond Laflamme. Testing contextuality on quantum ensembles with one clean qubit. *Phys. Rev. Lett.*, 104:160501, Apr 2010.

[112] Arthur Fine. Hidden variables, joint probability, and the bell inequalities. *Phys. Rev. Lett.*, 48:291–295, Feb 1982.

[113] S. Kochen and E. P. Specker. *J. Math. Mech.*, 17:59, 1967.

[114] A Peres. Two simple proofs of the kochen-specker theorem. *Journal of Physics A: Mathematical and General*, 24(4):L175, 1991.

[115] N. David Mermin. Simple unified form for the major no-hidden-variables theorems. *Phys. Rev. Lett.*, 65:3373–3376, Dec 1990.

[116] M. Markiewicz, P. Kurzynski, J. Thompson, S. Y. Lee, A. Soeda, T. Paterek, and D. Kaszlikowski. Unified approach to contextuality, non-locality, and temporal correlations. 2013.

[117] D. G. Cory, M. D. Price, and T. F. Havel. *Physica D*, 120:82, 1998.

[118] Geoffrey Bodenhausen. Multiple-quantum nmr. *Progress in Nuclear Magnetic Resonance Spectroscopy*, 14(3):137–173, 1980.

[119] Hwang Lee, Pieter Kok, and Jonathan P Dowling. A quantum rosetta stone for interferometry. *Journal of Modern Optics*, 49(14-15):2325–2338, 2002.

[120] Jonathan P Dowling. Quantum optical metrology–the lowdown on high-n00n states. *Contemporary physics*, 49(2):125–143, 2008.

[121] Yu-Ao Chen, Xiao-Hui Bao, Zhen-Sheng Yuan, Shuai Chen, Bo Zhao, and Jian-Wei Pan. Heralded generation of an atomic noon state. *Physical review letters*, 104(4):043601, 2010.

[122] Jonathan A Jones, Steven D Karlen, Joseph Fitzsimons, Arzhang Ardavan, Simon C Benjamin, G Andrew D Briggs, and John JL Morton. Magnetic field

sensing beyond the standard quantum limit using 10-spin noon states. *Science*, 324(5931):1166–1168, 2009.

[123] Richard Ghez. *Diffusion phenomena: cases and studies*. Springer Science & Business Media, 2001.

[124] Norman Henry March, Mario P Tosi, and Norman H March. *Introduction to liquid state physics*. World Scientific, 2002.

[125] BR Condon, J Patterson, D Wyper, A Jenkins, and DM Hadley. Image non-uniformity in magnetic resonance imaging: its magnitude and methods for its correction. *The British journal of radiology*, 60(709):83–87, 1987.

[126] Agedi N Boto, Pieter Kok, Daniel S Abrams, Samuel L Braunstein, Colin P Williams, and Jonathan P Dowling. Quantum interferometric optical lithography: exploiting entanglement to beat the diffraction limit. *Physical Review Letters*, 85(13):2733, 2000.

[127] Herman Y Carr and Edward M Purcell. Effects of diffusion on free precession in nuclear magnetic resonance experiments. *Physical Review*, 94(3):630, 1954.

[128] EO Stejskal and JE Tanner. Spin diffusion measurements: spin echoes in the presence of a time-dependent field gradient. *The journal of chemical physics*, 42(1):288–292, 1965.

[129] William S Price and Philip W Kuchel. Effect of nonrectangular field gradient pulses in the stejskal and tanner (diffusion) pulse sequence. *Journal of Magnetic Resonance (1969)*, 94(1):133 – 139, 1991.

[130] William S Price. Pulsed-field gradient nuclear magnetic resonance as a tool for studying translational diffusion: Part 1. basic theory. *Concepts in magnetic resonance*, 9(5):299–336, 1997.

[131] William S Price. Pulsed-field gradient nuclear magnetic resonance as a tool for studying translational diffusion: Part ii. experimental aspects. *Concepts in Magnetic Resonance*, 10(4):197–237, 1998.

[132] CS Johnson. Diffusion ordered nuclear magnetic resonance spectroscopy: principles and applications. *Progress in Nuclear Magnetic Resonance Spectroscopy*, 34(3):203–256, 1999.

[133] Simone Cavadini, Jens Dittmer, Sasa Antonijevic, and Geoffrey Bodenhausen. Slow diffusion by singlet state nmr spectroscopy. *Journal of the American Chemical Society*, 127(45):15744–15748, 2005.

[134] Nirbhay N Yadav, Allan M Torres, and William S Price. Nmr q-space imaging of macroscopic pores using singlet spin states. *Journal of Magnetic Resonance*, 204(2):346–348, 2010.

[135] Michael J. Thrippleton, Nikolaus M. Loening, and James Keeler. A fast method for the measurement of diffusion coefficients: one-dimensional dosy. *Magnetic Resonance in Chemistry*, 41(6):441–447, 2003.

[136] Lewis E Kay and JH Prestegard. An application of pulse-gradient double-quantum spin echoes to diffusion measurements on molecules with scalar-coupled spins. *Journal of Magnetic Resonance (1969)*, 67(1):103–113, 1986.

[137] Bocomv E Chapman and PW Kuchel. Sensitivity in heteronuclear multiple-quantum diffusion experiments. *Journal of Magnetic Resonance, Series A*, 102(1):105–109, 1993.

[138] Gang Zheng, Allan M Torres, and William S Price. Mq-pgste: a new multi-quantum ste-based pgse nmr sequence. *Journal of Magnetic Resonance*, 198(2):271–274, 2009.

[139] HC Torrey. Transient nutations in nuclear magnetic resonance. *Physical Review*, 76(8):1059, 1949.

[140] Shangwu Ding, Charles A McDowell, Chaohui Ye, Mingsheng Zhan, Xiwen Zhu, Kelin Gao, Xianping Sun, Xi-An Mao, and Maili Liu. Quantum computation based on magic-angle-spinning solid state nuclear magnetic resonance spectroscopy. *The*

European Physical Journal B-Condensed Matter and Complex Systems, 24(1):23–35, 2001.

[141] Garett M. Leskowitz, Nima Ghaderi, Ryan A. Olsen, and Leonard J. Mueller. Three-qubit nuclear magnetic resonance quantum information processing with a single-crystal solid. *The Journal of Chemical Physics*, 119(3), 2003.

[142] Jonathan Baugh, Osama Moussa, Colm A. Ryan, Raymond Laflamme, Chandrasekhar Ramanathan, Timothy F. Havel, and David G. Cory. Solid-state nmr three-qubit homonuclear system for quantum-information processing: Control and characterization. *Phys. Rev. A*, 73:022305, Feb 2006.

[143] Stephanie Simmons, Richard M Brown, Helge Riemann, Nikolai V Abrosimov, Peter Becker, Hans-Joachim Pohl, Mike LW Thewalt, Kohei M Itoh, and John JL Morton. Entanglement in a solid-state spin ensemble. *Nature*, 470(7332):69–72, 2011.

[144] Yu-Sze Yen and A Pines. Multiple-quantum nmr in solids. *The Journal of chemical physics*, 78(6):3579–3582, 1983.

[145] J Baum, M Munowitz, AN Garroway, and A Pines. Multiple-quantum dynamics in solid state nmr. *The Journal of chemical physics*, 83(5):2015–2025, 1985.

[146] Hans Georg Krojanski and Dieter Suter. Decoherence in large nmr quantum registers. *Physical Review A*, 74(6):062319, 2006.

[147] Marko Lovrić, Hans Georg Krojanski, and Dieter Suter. Decoherence in large quantum registers under variable interaction with the environment. *Phys. Rev. A*, 75:042305, Apr 2007.

[148] Gonzalo A. Álvarez and Dieter Suter. Nmr quantum simulation of localization effects induced by decoherence. *Phys. Rev. Lett.*, 104:230403, Jun 2010.

[149] Herman Y Carr and Edward M Purcell. Effects of diffusion on free precession in nuclear magnetic resonance experiments. *Physical Review*, 94(3):630, 1954.

[150] Saul Meiboom and David Gill. Modified spin-echo method for measuring nuclear relaxation times. *Review of scientific instruments*, 29(8):688–691, 1958.

[151] Lorenza Viola, Emanuel Knill, and Seth Lloyd. Dynamical decoupling of open quantum systems. *Physical Review Letters*, 82(12):2417, 1999.

[152] Götz S Uhrig. Keeping a quantum bit alive by optimized π-pulse sequences. *Physical Review Letters*, 98(10):100504, 2007.

[153] Michael J Biercuk, Hermann Uys, Aaron P VanDevender, Nobuyasu Shiga, Wayne M Itano, and John J Bollinger. Optimized dynamical decoupling in a model quantum memory. *Nature*, 458(7241):996–1000, 2009.

[154] Michael J. Biercuk, Hermann Uys, Aaron P. VanDevender, Nobuyasu Shiga, Wayne M. Itano, and John J. Bollinger. Experimental uhrig dynamical decoupling using trapped ions. *Phys. Rev. A*, 79:062324, Jun 2009.

[155] MJ Biercuk, AC Doherty, and H Uys. Dynamical decoupling sequence construction as a filter-design problem. *Journal of Physics B: Atomic, Molecular and Optical Physics*, 44(15):154002, 2011.

[156] Jiangfeng Du, Xing Rong, Nan Zhao, Ya Wang, Jiahui Yang, and RB Liu. Preserving electron spin coherence in solids by optimal dynamical decoupling. *Nature*, 461(7268):1265–1268, 2009.

[157] Gonzalo A Alvarez, Ashok Ajoy, Xinhua Peng, and Dieter Suter. Performance comparison of dynamical decoupling sequences for a qubit in a rapidly fluctuating spin bath. *Physical Review A*, 82(4):042306, 2010.

[158] Łukasz Cywiński, Roman M. Lutchyn, Cody P. Nave, and S. Das Sarma. How to enhance dephasing time in superconducting qubits. *Phys. Rev. B*, 77:174509, May 2008.

[159] G De Lange, ZH Wang, D Riste, VV Dobrovitski, and R Hanson. Universal dynamical decoupling of a single solid-state spin from a spin bath. *Science*, 330(6000):60–63, 2010.

[160] C Barthel, J Medford, CM Marcus, MP Hanson, and AC Gossard. Interlaced dynamical decoupling and coherent operation of a singlet-triplet qubit. *Physical review letters*, 105(26):266808, 2010.

[161] C. A. Ryan, J. S. Hodges, and D. G. Cory. Robust decoupling techniques to extend quantum coherence in diamond. *Phys. Rev. Lett.*, 105:200402, Nov 2010.

[162] Yoav Sagi, Ido Almog, and Nir Davidson. Process tomography of dynamical decoupling in a dense cold atomic ensemble. *Phys. Rev. Lett.*, 105:053201, Jul 2010.

[163] Ashok Ajoy, Gonzalo A Álvarez, and Dieter Suter. Optimal pulse spacing for dynamical decoupling in the presence of a purely dephasing spin bath. *Physical Review A*, 83(3):032303, 2011.

[164] S Pasini, P Karbach, and GS Uhrig. High-order coherent control sequences of finite-width pulses. *EPL (Europhysics Letters)*, 96(1):10003, 2011.

[165] Ya Wang, Xing Rong, Pengbo Feng, Wanjie Xu, Bo Chong, Ji-Hu Su, Jiangbin Gong, and Jiangfeng Du. Preservation of bipartite pseudoentanglement in solids using dynamical decoupling. *Phys. Rev. Lett.*, 106:040501, Jan 2011.

[166] GS Agarwal. Saving entanglement via a nonuniform sequence of π pulses. *Physica Scripta*, 82(3):038103, 2010.

[167] Musawwadah Mukhtar, Wee Tee Soh, Thuan Beng Saw, and Jiangbin Gong. Protecting unknown two-qubit entangled states by nesting uhrig's dynamical decoupling sequences. *Phys. Rev. A*, 82:052338, Nov 2010.

[168] Soumya Singha Roy and TS Mahesh. Initialization of nmr quantum registers using long-lived singlet states. *Physical Review A*, 82(5):052302, 2010.

[169] Toshiki Hayashi, Toshimasa Fujisawa, Hai-Du Cheong, Yoon Hee Jeong, and Yoshiro Hirayama. Coherent manipulation of electronic states in a double quantum dot. *Physical review letters*, 91(22):226804, 2003.

[170] DJ Reilly, JM Taylor, JR Petta, CM Marcus, MP Hanson, and AC Gossard. Suppressing spin qubit dephasing by nuclear state preparation. *Science*, 321(5890):817–821, 2008.

[171] AC Johnson, JR Petta, JM Taylor, A Yacoby, MD Lukin, CM Marcus, MP Hanson, and AC Gossard. Triplet–singlet spin relaxation via nuclei in a double quantum dot. *Nature*, 435(7044):925–928, 2005.